ALMA MATER STUDIORUM
UNIVERSITÀ DI BOLOGNA

DEPARTMENT OF PHYSICS AND ASTRONOMY "A. RIGHI"

SECOND CYCLE DEGREE

PHYSICS

Neutrino physics with the XENONnT Water Cherenkov Veto

Supervisor
Prof. Marco Selvi

Co-supervisor
Dr. Pietro Di Gangi

Defended by
Ana Barahona Roda

Graduation Session December 2025

Academic Year 2024/2025

Abstract

Dark Matter and neutrinos constitute two of the most elusive components of the Universe. The XENONnT experiment, located at the underground INFN Laboratori Nazionali del Gran Sasso (LNGS) in Italy, aims to detect Weakly Interacting Massive Particles (WIMPs), one of the leading Dark Matter candidates nowadays. A dual-phase Time Projection Chamber (TPC) filled with 6 t of liquid xenon is employed to achieve this purpose. The TPC is surrounded by the Neutron Veto (NV) and the Muon Veto (MV), which operate in coincidence with the core detector to discriminate backgrounds such as radiogenic neutrons and cosmic muons. The Muon Veto contains approximately 700 tonnes of water, with about 34 tonnes being nearly optically separated in the inner Neutron Veto. Neutrinos, through coherent neutrino-nucleus scattering (CEνNS), constitute a major background due to their similarity to a WIMP signal. Nevertheless, neutrinos are also an important signal to be investigated. Therefore, assessing the NV and MV ability to detect signals from two of the most important neutrino sources in the MeV-GeV range, galactic core-collapse supernova (CCSN) and atmospheric neutrinos, is crucial.

Simulations of a benchmark CCSN scenario in the MV (NV) predict 108 (8) detected positron events, out of the expected 162 (8) inverse beta decay interactions occurring within a 10 s burst. This study concludes that the NV features a positron detection threshold of about 0.5 MeV, while the MV exhibits a ~5 MeV detection threshold. Atmospheric neutrino interactions yield an annual rate of 56 (4) detected out of approximately 88 (5) expected events in the MV (NV), arising from interactions in pure water of electron and muon neutrinos and antineutrinos. Extrapolating these results to XLZD by assuming a proposed MV+NV configuration with ~ 1300 tonnes of total water volume and the same performance of the XENONnT vetoes, the detection of 118 atmospheric neutrino events per year can be achieved.

Contents

List of Figures

List of Tables

Introduction

The purpose of the study developed in this master's thesis is to examine the ability of the two veto subsystems of the XENONnT Dark Matter experiment to detect two important sources of neutrino signals: neutrinos from core-collapse supernovae, and those known as atmospheric neutrinos. The two vetoes, the Neutron Veto and the Muon Veto, are considered in their demineralized-water phase.

Chapter 1 will address the physics of these particles, neutrinos, beginning with their first mentions, discovery, characteristics, and typical interactions. Some neutrino properties, such as their oscillations in vacuum, will be further elaborated in the first section. Subsequently, the introduction of supernova and atmospheric neutrinos will be addressed.

Chapter 2 will describe the concept of Dark Matter (DM) and its main candidate, a Weakly Interacting Massive Particle (WIMP), which, despite constituting approximately 85% of the matter in the Universe, remains unobserved. This chapter will detail the XENONnT experiment in the context of the XENON Dark Matter Project, being one of the cutting-edge direct Dark Matter experiments nowadays. The experiment will be described by presenting the working principle and structure of its core detector, the dual-phase Time Projection Chamber (TPC). An overview of the calibration and purification systems, including the Gadolinium-Water purification system, will be provided, followed by a description of the most relevant subsystems to this study, the Neutron Veto (NV) and the Muon Veto (MV). As will be evident in the course of this chapter, the results obtained by the XENONnT experiment are significantly approaching the so-called "neutrino fog".

Chapter 3, revisits the topic of supernova neutrinos. This chapter analyzes the characteristics of their flux reaching the Earth, as well as their interaction cross section in pure water, with particular emphasis on the well-known inverse beta decay. From the integration of these two effects, the expected number of events in the XENONnT veto system will be obtained. Subsequently, Montecarlo (MC) simulations of the vetoes, integrated in GEANT4 and their PMT simulated response to the Cherenkov light using the Hitlet Simulator, will be introduced. Finally, the results of these simulations and the detection efficiencies obtained from them will be presented, together with their projection to the successor experiment of XENONnT, the XLZD observatory.

Chapter 4 addresses the characterization of the atmospheric neutrino flux and its associated uncertainties, as well as the interactions in water that are relevant in the energy regime considered in this study. Based on these elements, the expected number of events in the vetoes is derived. In the present chapter, MC simulations of these detectors are again employed to perform a comprehensive analysis of the atmospheric neutrino detection efficiency. Finally, the results obtained in this study are projected onto the XLZD observatory.

1 Neutrino Physics

This chapter will provide the necessary background to understand neutrinos' nature and two of their possible sources, due to their implication on XENONnT backgrounds and physics searches. Section 1.1.1 will serve as an introduction to the neutrino hypothesis and eventual discovery, whereas the different properties of these particles, especially highlighting neutrino mixing and oscillations will be outlined in Section 1.1.2. Finally, the main interactions with ordinary matter, relevant at low-intermediate neutrino energies, will be described in Section 1.1.3.

Two types of neutrino sources will be introduced in Sections 1.2 and 1.3, core collapse supernova and atmospheric neutrinos, respectively.

1.1 The Nature of Neutrinos

1.1.1 Neutrino Postulation and Discovery

The history of weak interactions, based on the Standard Model (SM) gauge group $SU(2)_L$, is closely related to that of the neutral and "massless" leptons, the so-called neutrinos by Enrico Fermi. The history of the hypothesis and discovery of these elusive particles will be briefly introduced below.

The Neutrino Hypothesis and the Fermi Theory of β Decay

In 1930, Wolfgang Pauli proposed a remedy to a serious problem introduced by James Chadwick in 1914, the continuous β spectrum, up to its maximum value, from the decay of the same name. Since no other particle was observed, the β-decay seemed to violate the energy conservation law. However, in an open letter to a physics conference at Tubingen, Pauli proposed the existence of a neutral weakly interacting fermion emitted in this decay, giving it the name of "neutron" and associating it with a mass of the order of the electron. After the discovery of the currently known neutron in 1932 by Chadwick, Enrico Fermi renamed the hypothetical particle proposed by Pauli as "neutrino", and later concluded that it could be massless.

After all these, the first milestone of the theory of the weak interactions came when Fermi formulated the theory of the β-decay, analogous to the quantum electrodynamics (QED) theory.

The theoretical framework developed by Fermi included several fundamental aspects:

Long particle lifetimes in decays through weak interactions (10^{-10}s) with regard to decays via electromagnetic (EM) (10^{-19}s) and strong (10^{-23}s) interactions, described by gauge groups $U(1)_Y$ and $SU(3)_C$, respectively.

Small cross sections increasing linearly with energy. At 1 GeV, it is of the order of 10^{-38}cm^2, which is about 10^{12} times smaller than the one from strong interaction processes.

Neutrinos only interact through weak interactions, whereas charged leptons also interact through EM interactions. For reference, neutrinos of about 1 MeV have a cross section of the order of 10^{-44} cm^2, which means that only one out of 10^{11} neutrinos interacts while traversing the Earth's diameter.

Weak interactions violate parity P, charge conjugation C, and strangeness S, which are instead conserved in EM and strong interactions.

Weak interactions are responsible for radioactive β-decays and have a crucial role in astrophysical systems, even if they do not participate in nuclear binding systems.

In 1936, in order to extend the Fermi theory to β-decays with different nuclear spins in the final with regard to the initial state, George Gamow and Edward Teller introduced axial-vector currents, in that way conserving parity. Although the remarkable success of the Fermi Theory, some scientists remained doubtful about the neutrino existence, however in the early 1950's everything changed.

The Neutrino Discovery

Clyde Cowan and Frederick Reines in 1956 sent a telegram to Pauli claiming the discovery of the "Poltergeist". They were able to discover the neutrino through the inverse β-decay (IBD):

$$\bar{\nu}_e + p \rightarrow e^+ + n \tag{1}$$

in which the coincidence signal between the positron annihilation and the neutron capture could definitely prove the existence of this evasive particle, distinguishing the signal from the environmental background.

After considering methods such as a nuclear explosion to create a large flux of neutrinos and increase the expected rate, finally they decided to use the steady flux, of about one neutrino every few hours, coming from the near Savannah River nuclear reactor. They made use of a detector that included 1400 liters of liquid scintillator and 200 liters of water. Furthermore, the Savannah experiment not only demonstrated the existence of neutrinos, but also allowed the calculation of the IBD cross section by measuring and estimating the interaction rate, the neutrino flux, the number of targets and the efficiency of the detector. The obtained [1] cross section was 1.3×10^{-43} cm^2 with an estimated associated error of about 25% [2], [3], [4].

1.1.2 Neutrino Properties

After the neutrino discovery, several of its properties were progressively revealed during the second half of the 20th century. In fact, only one year after its discovery, the study performed by Chien-Shiung Wu highlighted the parity violation in processes induced by weak interactions. The consequences of this fact for the **neutrino helicity** is actually relevant. The helicity is defined as the projection of the momentum over the spin, in contrast to the chirality which indicates whether a particle is right-handed or left-handed. The two operators are identical only in the ultra-relativistic limit or for a massless particle[1]. It was observed in all processes that the direction of the neutrino spin is contrary to that of their motion (negative helicity or left-handed), and the opposite is true for antineutrinos (positive helicity or right-handed).

The idea that there were different **neutrino flavors** had already been postulated by Bruno Pontecorvo when, in 1962, the muon neutrino was identified at the Brookhaven National Laboratory. In 1975, the τ lepton was discovered by Martin Lewis Perl and it constituted the third and heaviest charged lepton. It was then hypothesized its associated neutrino, which was eventually reported by the DONUT experiment [5] at Fermilab in July 2000. The vector bosons mediating the weak interaction, $W^{\pm}$ and Z^0, were identified in 1983 at the proton-antiproton collider at CERN in Geneva.

---

[1] A massive non ultra-relativistic left-handed particle is described by a linear combination of the two helicity states, depending on its mass. The same thing happens if the particle is right-handed.

Since the early 1990s, there has been extensive research directed to the study of neutrinos. One example of this was the discovery by the Super-Kamiokande experiment [6] and by the Sudbury Neutrino Observatory (SNO) [7], which provided conclusive evidence of **neutrino oscillations in vacuum**, confirming that neutrinos have mass and mix between flavors. This concept was previously proposed by Pontecorvo in the 1950s. Later, a more realistic scenario emerged, assuming that the flavor eigenstates (ν_e, ν_μ) are superpositions of two or more mass eigenstates, an idea formalized by Maki, Nakagawa, and Sakata in 1967. These discoveries not only solved the long-standing solar and atmospheric neutrino anomalies, which showed a discrepancy between detection and expectation of these fluxes, but also marked the first clear indication of physics beyond the Standard Model (BSM), showing the necessity of incorporating neutrino masses to this theory.

Neutrino oscillations arise from the interference between their mass eigenstates, which are produced and detected coherently due to their extremely small mass differences. In CC weak interactions, associated to their charged leptons, neutrinos are created in flavor eigenstates, namely ν_e, ν_μ, or ν_τ. These weak eigenstates do not possess a definite mass but can instead be expressed as linear combinations of three mass eigenstates ν_1, ν_2, and ν_3, according to

$$|\nu_\alpha\rangle = \sum_j U^*_{\alpha j} |\nu_j\rangle, \tag{2}$$

where $\alpha = e, \mu, \tau$ and $j = 1, 2, 3$. Here, U represents the Pontecorvo–Maki–Nakagawa–Sakata (PMNS) unitary mixing matrix. For three neutrino flavors, U can be parameterized in terms of three mixing angles θ_{12}, θ_{13}, θ_{23} and one CP-violating phase δ as

$$U = \begin{pmatrix} 1 & 0 & 0 \\ 0 & c_{23} & s_{23} \\ 0 & -s_{23} & c_{23} \end{pmatrix} \begin{pmatrix} c_{13} & 0 & s_{13}e^{-i\delta} \\ 0 & 1 & 0 \\ -s_{13}e^{i\delta} & 0 & c_{13} \end{pmatrix} \begin{pmatrix} c_{12} & s_{12} & 0 \\ -s_{12} & c_{12} & 0 \\ 0 & 0 & 1 \end{pmatrix}, \tag{3}$$

where $c_{jk} = \cos\theta_{jk}$ and $s_{jk} = \sin\theta_{jk}$.

Neutrinos are thus produced in weak eigenstates, propagate as mass eigenstates, and are finally detected again as weak eigenstates. The time evolution of each mass eigenstate introduces a phase difference, leading to a flavor transition probability, which can be approximated for ultra-relativistic neutrinos, and expressed in terms of the distance $L \simeq ct$ between the source and the detector (baseline), since in experiments the propagation time is not directly measured and the neutrino energy E. In the simplified case of two-neutrino mixing, with their associated mixing angle $\theta_{\alpha\beta}$, this probability reduces to

$$P(\nu_\alpha \to \nu_\beta, L) = \sin^2 2\theta_{\alpha\beta}\, \sin^2\left(1.27\,\frac{\Delta m^2[\mathrm{eV}^2]\, L[\mathrm{km}]}{E[\mathrm{GeV}]}\right) \tag{4}$$

The mass difference between the second and the first as well as between the third (lone) and the first neutrino states have been measured allowing for the determination of these parameters: $\Delta m^2_{21} \simeq (7.53 \pm 0.18) \times 10^{-5}\ \mathrm{eV}^2$ [8] (the solar mass splitting) and $\Delta m^2_{31} \simeq (2.31^{+0.11}_{-0.13}) \times 10^{-3}\ \mathrm{eV}^2$ [9] (the atmospheric mass splitting) if normal ordering (NO) is considered. In normal ordering the lone mass eigenstate is the most massive, on the other hand, if the inverted ordering (IO) is considered, where the lone neutrino state is the lightest one, the atmospheric mass splitting is $\Delta m^2_{23} \simeq (2.471^{+0.068}_{-0.070}) \times 10^{-3}\ \mathrm{eV}^2$ [10].

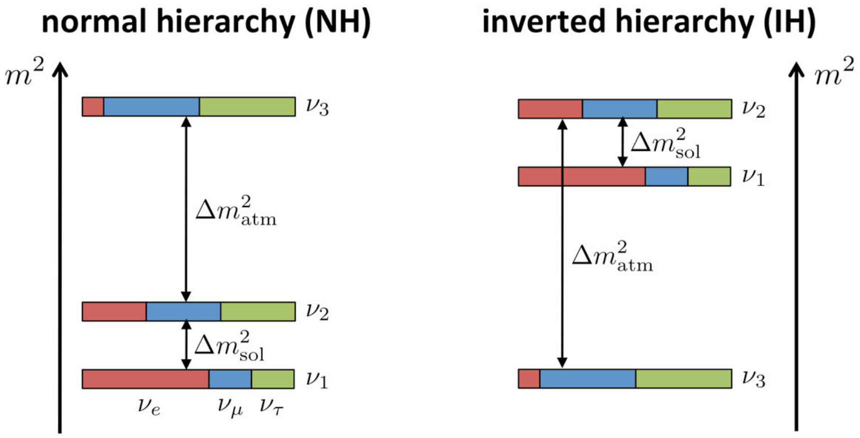

Figure 1: Neutrino mass hierarchy of the three neutrinos ν_1, ν_2, ν_3, assuming $m_{\nu_3} > m_{\nu_2} > m_{\nu_1}$ (NO) in the left picture and $m_{\nu_2} > m_{\nu_1} > m_{\nu_3}$ (IO) in the right one. Since the weak interaction eigenstates, ν_e, ν_μ, ν_τ are a linear combination of mass eigenstates, experiments can determine the flavor states percentage in mass states. This percentage is represented by different colors in the drawing. The ν_3 is ~45% ν_μ (in blue) and ~45% ν_τ (green). The ν_2 is about 1/3 ν_e (red), 1/3 ν_μ , 1/3 ν_τ . Finally, the ν_e dominates in the ν_1. Credit: JUNO Collaboration [11] / Johannes Gutenberg University-Mainz

These parameters are called solar and atmospheric mass splitting due to the solar observations of oscillations in ν_e and atmospheric measurements of ν_μ oscillations to ν_τ, respectively.

In fact, in one of the experiments where the Cherenkov angle is reconstructed, Super-Kamiokande [12], the distribution of μ-like events (attributed to ν_μ) in terms of the angle of incoming atmospheric flux, exhibited a clear deficit compared to the no-oscillation expectation, while the number of e-like events (those induced by ν_e) remained broadly consistent with the prediction[2], [3], [4], [13].

1.1.3 Neutrino Interactions with Ordinary Matter

Neutrinos interact with ordinary matter through weak interactions, mediated by charged $W^\pm$ or neutral Z^0 gauge bosons. The former type is the so-called charge current (CC) weak interaction, whereas the latter is named as neutral current (NC) weak interaction. Both fall within the general gauge theory $SU(2)_L \times U(1)_Y$, even if neutrinos represent the first significant alteration to the SM with their masses. However, in practice and as with many other disciplines, one finds out that theoretical approximations which work well in one particular energy regime completely break down elsewhere. So actually many factors form the simple description of the weak interactions, such as unclear initial state conditions, subtle but not negligible nuclear corrections or final state interactions.

The main interactions ordered by increasing energy, between neutrinos and ordinary matter will be explained below, considering the related CC or/and NC interactions that take place in each case. Moreover, the selected energy range will cover the one useful for this study, supernova and atmospheric neutrino energy range, as shown in Fig. 2, which goes from 1 MeV up to about 1 GeV.

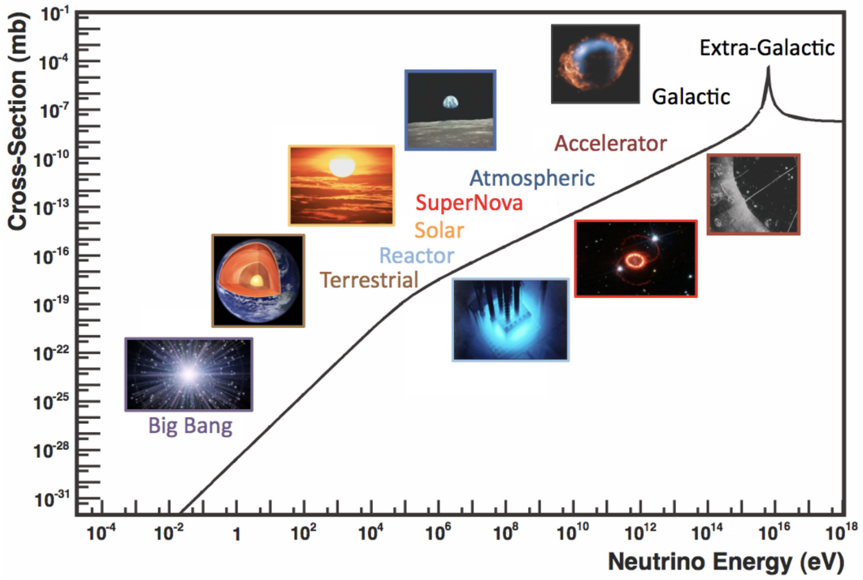

Figure 2: Neutrino sources in the cross section-energy space. The cross section shown is the elastic anti-neutrino-electron scattering. The peak at 10^{16} eV is due to the W^- resonance. Plot taken from [14].

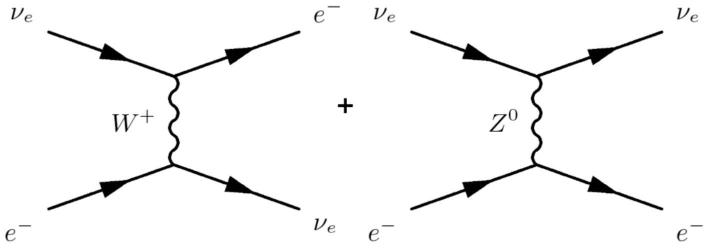

Figure 3: Tree-level Feynman diagram for CC and NC components of the electron neutrino-electron elastic scattering [14]

First, for neutrino energies of the order of tens to hundreds of MeV, we will find dominant interactions in which neutrinos interact with nuclei and atomic electrons without disruptive effects on the former. Then, when neutrino energies have approximately 200 MeV, other interactions, often disruptive, appear with the nucleons inside nuclei, producing several hadrons in the final state.

In Fig. **??** all cross sections from the interactions introduced below are summarized. These interactions, ordered by increasing energy are [14], [15], [16]:

Coherent elastic neutrino-nucleus scattering (CEνNS) is a threshold-less process which dominates at neutrino energies between 0 and 1 MeV. Mediated by NCs, this scattering is the foundation of neutrino detection in the XENONnT Time Projection Chamber, through the measurement of the xenon nuclear recoil and it is represented as:

$$\nu + A_N^Z \longrightarrow \nu + A_N^{*Z} \tag{5}$$

Neutrino electron elastic scattering being also a threshold-less process, has extremely small cross sections (of the order of $10^{-42}(E_\nu/\mathrm{GeV})\mathrm{cm}^2$). Both processes mediated by NCs and CCs are possible for electron neutrinos (Fig, 3) and antineutrinos. On the other hand, muon neutrinos and antineutrinos, due to lepton number conservation must interact via NC processes. The reactions are:

$$\nu + e^- \longrightarrow \nu + e^- \tag{6}$$

Inverse Beta Decay (IBD) dominates at low energy ($E_\nu \sim 1 - 100$ MeV) and is essential for reactor, solar and supernova electron anti-neutrinos. Its threshold is $E_\nu \geq m_n + m_e - m_p = 1.806$ MeV and it only occurs through the CC interaction (also shown in eq. 1).:

$$\bar{\nu}_e + p \longrightarrow n + e^+ \tag{7}$$

The associated CC reaction of an electron neutrino with a neutron, has a higher threshold due to the typical binding energy of the latter in a nucleus (e.g. of the order of 10 MeV in oxygen).

Neutrino-nucleus quasi-elastic scattering (QES) is the dominant neutrino-hadron interaction at intermediate energies ($E_\nu \sim 0.1-2$ GeV). In CC neutrino QES, the target neutron is converted into a proton, whereas in the anti-neutrino QES the opposite process takes place. The reactions are:

$$\begin{aligned} \bar{\nu}_l + p &\longrightarrow n + l^+ \\ \nu_l + n &\longrightarrow p + l^- \end{aligned} \tag{8}$$

with l = μ, τ, when l = e, the former reaction turns into the IBD and the latter is the one also mentioned in that paragraph.

Neutrino-nucleus elastic scattering is dominant in the same energy regime as the CC QES. In this case neutrinos scatter off nucleons via NCs as:

$$\nu + p \to \nu + p \quad \nu + n \to \nu + n \tag{9}$$

Multi-nucleon scattering. Both CC QES and NC elastic scattering between neutrinos and nuclei can also liberate several nucleons instead of only one (1p1h), due to many-body effects. In this process, n-particle are knocked out, leaving n-holes (np-nh). Due to these processes, the CC-QES cross section is significantly enhanced at neutrino energies of about 0.1 GeV.

Baryon resonant production (RES) (becomes relevant above ~0.1 GeV) by neutrinos that excite the target nucleon to a resonance state. The resultant baryonic resonance (Δ, N^*) decays to a variety of possible mesonic final states, including nucleons. At the energies considered in this study only single pion production is possible through CC or NC interactions:

$$\nu + N \to l/\nu + N^*/\Delta, \quad N^*/\Delta \to \pi N' \tag{10}$$

where N and N' are the nucleons and π could be charged or neutral depending on the associated lepton and nucleon.

Diffractive and coherent pion production are processes with a low energy transfer to one nucleon or the whole nucleus, respectively. They are processes similar to the resonances but with lower cross sections and producing no nuclear recoil and a distinctly forward-scattered pion.

Deep-Inelastic scattering. At energies of the order of 1 GeV the neutrino can resolve the individual quark constituents of the nucleon, creating a hadronic system (X) along with the lepton in the final state. Both CC and NC processes are possible:

$$\nu + N \to l/\nu + X \tag{11}$$

Note that for each CC interaction mentioned, the threshold is always determined by the kinematics of the system. In the case of charged-lepton production, such as for muons, the thresholds are of the order of 100 MeV, plus the binding energy of the nucleons in the nucleus (which is, of course, not considered for hydrogen or free protons). NC interactions generally exhibit lower interaction thresholds, although this always depends on whether, for example, pions are produced in the final state or more than one nucleon is emitted.

1.2 Supernova Neutrinos

Core collapse supernovae originate from dying stars with masses $M > 8M_\odot$, that end up being neutron stars or black holes, and are among the most intense neutrino sources of the Universe. During a supernova (SN) explosion, 99% of the emitted energy is released in the form of a burst of $\sim 10^{58}$ neutrinos and anti-neutrinos of all flavors with mean energies which typically range between 10 and 20 MeV. SN neutrinos not only play the role of astrophysical messengers, but also highly influence the massive star's final state. In this study, neutron star final states will be considered.

1.2.1 Stellar Collapse and Supernova Explosions

Near the end of its life, a massive star consists of concentric shells, remnants of its previous burning phases. Iron, being the most tightly bound nucleus, is the final product of nuclear fusion in the stellar core. Once iron accumulates, no further fusion can take place to withstand the gravitational pressure, and the stability of the star becomes critically dependent on the equation of state (EoS) of the system, particularly on the number of leptons per baryon. During the early stages of the collapse (t=0 s), this lepton fraction decreases as electrons are captured by protons bound inside iron nuclei ($e^- + p \rightarrow n + \nu_e$), leading to a progressive loss of pressure support and an increasing **neutronization** of the core.

As the collapse continues, the gravitational implosion of the stellar iron core leads to the **formation of a proto-neutron star**[2] and the outset of intense neutrino emission. When the core density exceeds the nuclear saturation value ($\rho \sim 2.8 \times 10^{14}\,\mathrm{g\,cm^{-3}}$), the collapse halts and a rebound shock wave is launched (t = 0.10 s). As this shock propagates outward through the in-falling stellar material, it loses energy mainly through the dissociation of iron nuclei, until it stops at about 100-200 km from the center of the proto-neutron star, which still emits electron neutrinos produced by electron capture on protons. The produced ν_e initially escape freely, but as the density rises above $\sim 10^{12}\,\mathrm{g\,cm^{-3}}$, their mean free path becomes shorter than the stellar radius, causing them to become trapped in the dense nuclear matter (neutrinosphere), before the

---

[2] If the mass of the dying star would have a mass above 25 $M_\odot$ it would eventually turn into a black hole, instead of a neutron star.

stalled shock. This marks the **neutrino trapping phase** (t = 0.11 s), during which neutrinos are thermalized and remain confined until the matter becomes transparent again as the shock advances (t = 0.12 s).

After the shock release (the so-called supernova explosion) due to the neutrino heating, deleptonization[3] of the core proceeds rapidly, leading to a significant drop in the electron lepton number. At this stage, positrons become abundant and interact with neutrons via $e^{+} + n \rightarrow p + \bar{\nu}_e$, producing intense fluxes of electron antineutrinos. The **accretion** of matter onto the proto-neutron star continues for several hundred milliseconds, forming a hot accretion mantle that radiates high luminosities of ν_e and $\bar{\nu}_e$ (and other flavors), typically of the order of $10^{52} - 10^{53}$ erg/s, which carry away the majority of the gravitational binding energy released in the collapse. Some of these neutrinos also become trapped behind the stalled shock, increasing the temperature even more. As accretion declines, the proto-neutron star enters its **cooling** phase, during which neutrinos and antineutrinos of all flavors are emitted, through NCs neutrino pair production over timescales of several seconds, gradually removing the remaining gravitational energy (~ 90%).

These escaping neutrinos deposit a fraction of their energy in the surrounding matter, mainly through charged-current QES interactions. The resulting energy deposition drives an outflow of material from the surface of the nascent neutron star, forming what is known as the neutrino-driven wind (t = 10 s). This neutrino-induced outflow is thought to play a key role in the synthesis of trans-iron elements via the rapid neutron-capture process (r-process). The rate of mass loss and the dynamics of this wind are highly sensitive to the radius, mass, and temperature of the neutron star, as well as to the luminosity and average energy of the emitted neutrinos [4], [17], [18].

1.2.2 Supernova Neutrino Emission Phases

The supernova neutrino emission occurs in three phases during the explosion, carrying away approximately 99% of the energy. Neutrino and antineutrino luminosities and mean energies are shown in Figs. 4 and 5, for all neutrino flavors as a function of the post-bounce time for a SN progenitor of mass M=11.2 $M_\odot$ and M=27 $M_\odot$ at a distance of 10 kpc. Each of the three plots corresponds to the

---

[3] Phase in which the proto-neutron star emits electronic neutrinos, decreasing the lepton number and the amount of electrons with it.

three phases described below. On the other hand, the same is shown in Figs.6 and 7, but for two different equations of state, LS220 and SFHo. These simulations are taken from SNEWPY [19] Bollig et al. (2016) [20] and Sukhbold et al. (2015) [21] models, which use LS220 and SFHo equations of state, respectively.

The neutrino signal lasts about 10 s with a drop in luminosity after a few seconds. The three main phases of neutrino emission are described as follows:

1. Neutronization burst: when the proto-neutron star forms, a peak of electron neutrino emission is dominant, releasing a peak luminosity of about 10^{53} erg/s over a duration of roughly 10 ms. This phase involves mostly ν_e emission, with an average energy of about 12 MeV.
Shock wave propagation: As the shock wave moves outward through the iron core, nuclear matter becomes transparent to neutrinos. Free protons and neutrons are released as the shock dissociates iron nuclei. A burst of ν_e is emitted as the shocked matter heats. The size of the ν_e rise and the relative contribution of ν_x do not depend on the SN progenitor mass and EoS. The average maximum energy of ν_e in this phase reaches up to 12 MeV. The differences in the neutrino properties from different progenitors during the neutronization burst are small, but become considerable at later times.

2. Post-bounce accretion phase: The reaction $e^+ + n \to p + \bar{\nu}_e$ dominates along with electron neutrino production. A plateau in the neutrino luminosity is reached (with lower ν_x contribution). The average energy of neutrinos remains around ~10 MeV.
Shock wave energy loss: As the shock wave moves outward, it loses energy and stalls around 100–200 km. The ν_e luminosity declines and flattens into a plateau. Both ν_e and $\bar{\nu}_e$ are efficiently produced in the hot mantle through charged-current interactions that are more efficient and that is why both luminosities are similar, but the one of ν_e is slightly higher due to deleptonization. Neutral current processes dominate ν_x and $\bar{\nu}_x$ production with $x = \mu, \tau$, leading to lower luminosity compared to ν_e and $\bar{\nu}_e$. They have all increasing energies; however, the spectral slope for $\nu_e, \bar{\nu}_e$ is steeper. The higher the mass of the star, the higher the neutrino emission luminosity, as displayed in central Fig. 4.

3. Cooling phase: Neutrinos of all flavors are produced in the hot mantle of the proto-neutron star through $\nu_x\bar{\nu}_x$ production (here x refers to all neutrino flavors), with a gradual decrease of luminosity and average energy over several tens of seconds.

Cooling and deleptonization: After the explosion, the proto-neutron star gradually cools and deleptonizes. The neutrino signal slowly decreases in intensity. Even after the explosion, neutrino fluxes persist, and the gradual cooling of the outer layers leads to a continued, although diminishing, emission of neutrinos of all flavors (with similar luminosities).

The neutrinos have an expected energy distribution whose average energies follow the hierarchy $\langle E_{\nu_e} \rangle < \langle E_{\bar{\nu}_e} \rangle < \langle E_{\nu_\mu,\nu_\tau} \rangle$, due to their different interaction strengths with stellar matter. Electron neutrinos interact more frequently than antineutrinos because of the neutron excess in the core, while the latter, in turn, interact more than muon and tau neutrinos, which are limited to NC interactions. The expected supernova neutrino flux at Earth depends on several parameters, such as the time-dependent neutrino energy distribution at different post-bounce phases, the supernova luminosity, the distance between the source and the detector, and the neutrino oscillation probability, in particular the resonant matter effects [4], [17], [18], [20], [22]. These aspects will be explained in Section 3.1.1, together with a detailed description of the flux.

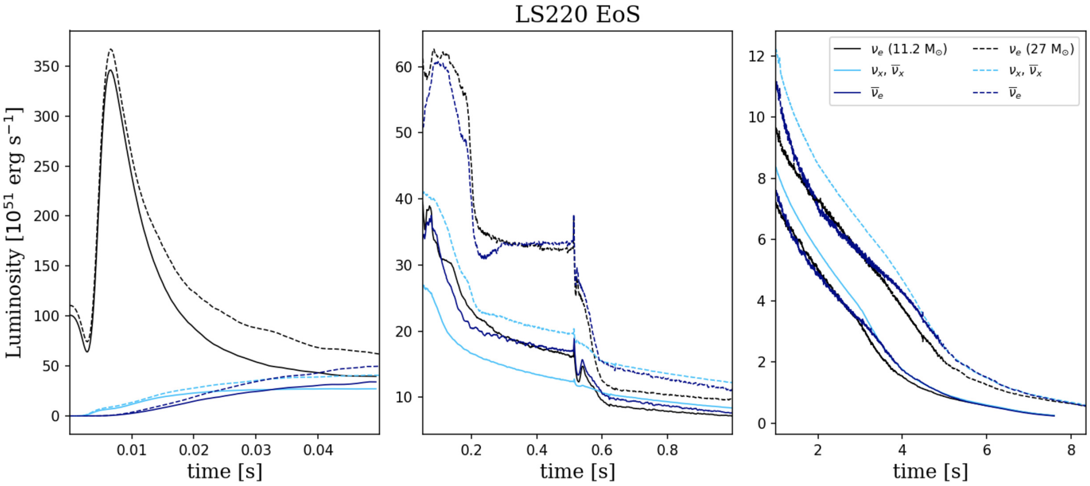

Figure 4: Neutrino luminosity as a function of post-bounce time from different SN progenitor masses, using the LS220 EoS, during the three main phases of the emitted signal: first the neutronization burst phase, then the accretion phase and finally the cooling phase. ν_x refers to muon and tau flavors.

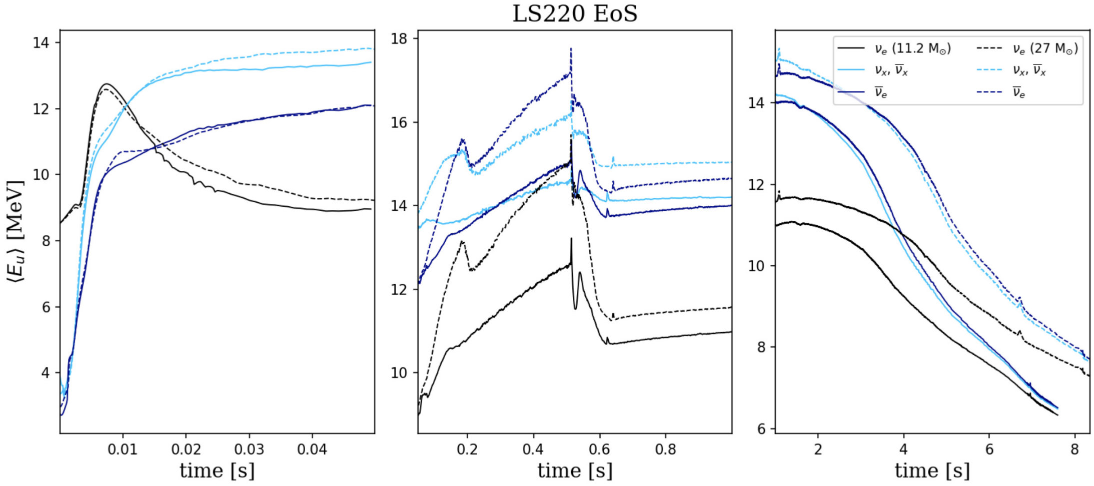

Figure 5: Neutrino mean energy as a function of post-bounce time from different SN progenitor masses, using the LS220 EoS, during the three main phases of the emitted signal: first the neutronization burst phase, then the accretion phase and finally the cooling phase.

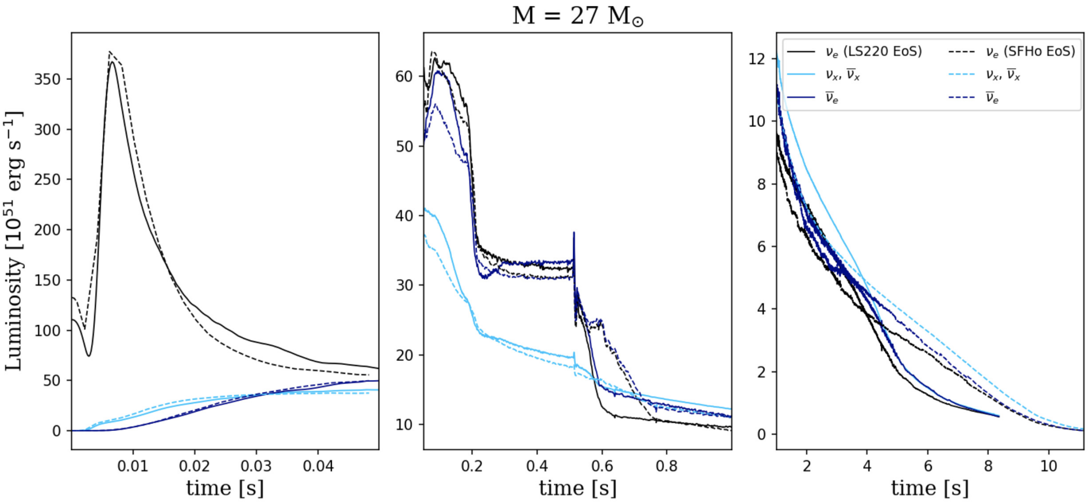

Figure 6: Neutrino luminosity as a function of post-bounce time from a SN progenitor mass of 27 $M_{\odot}$, using the LS220 and SFHo EoS, during the three main phases of the emitted signal: first the neutronization burst phase, then the accretion phase and finally the cooling phase. Note that the two models posses different maximum emission times.

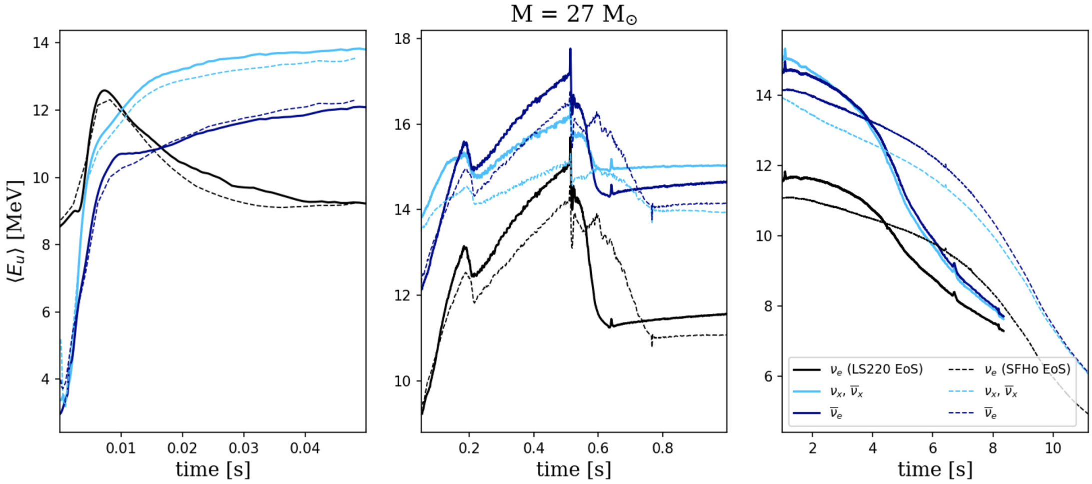

Figure 7: Neutrino mean energy as a function of post-bounce time from a SN progenitor mass of 27 M$_\odot$, using the LS220 and SFHo EoS, during the three main phases of the emitted signal: first the neutronization burst phase, then the accretion phase and finally the cooling phase. Note that the two models predict different maximum emission times.

1.3 Atmospheric Neutrinos

Atmospheric neutrinos are created when primary cosmic rays hit Earth's atmosphere, producing mesons whose decay chain leads to neutrinos, predominantly ν_μ, ν_e, $\bar{\nu}_\mu$, $\bar{\nu}_e$, as shown in Fig. 8–left.

The primary cosmic rays are mainly composed of protons, with a small component of heavier nuclei, such as ^{14}N or ^{16}O. Mesons and their decay products have an energy spectrum with a peak in the GeV range that extends to higher energies with an approximate power law. In particular, many secondary pions are produced which decay mainly into muons and muon neutrinos after traveling a certain path, through:

$$\pi^+ \longrightarrow \mu^+ + \nu_\mu, \quad \pi^- \longrightarrow \mu^- + \bar{\nu}_\mu \tag{12}$$

At high energies, kaons also contribute to the production of muons and neutrinos.

The muons decay before hitting the ground, generating electrons, electron neutrinos, and muon neutrinos through the processes:

$$\mu^+ \rightarrow e^+ + \nu_e + \bar{\nu}_\mu, \quad \mu^- \longrightarrow e^- + \bar{\nu}_e + \nu_\mu \tag{13}$$

Atmospheric neutrinos, from the decay chain of pions and kaons, have a wide spectrum of energy, which ranges from below the 100 MeV scale up to multi-TeV.

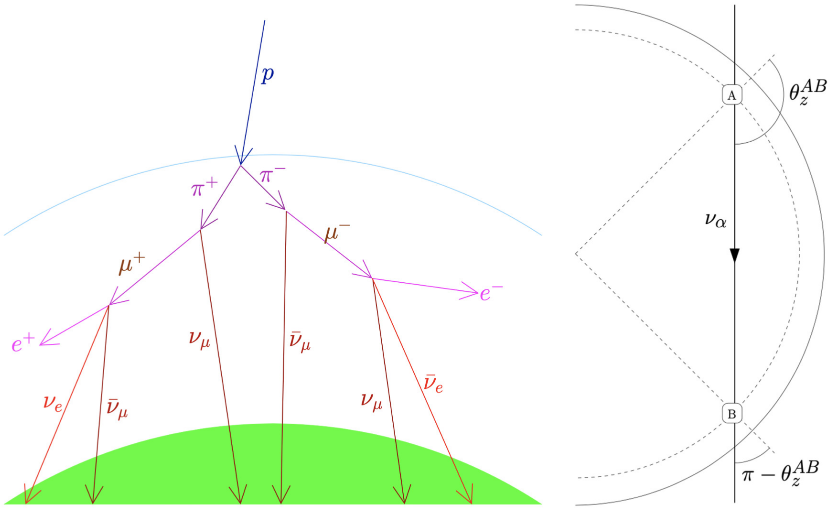

Figure 8: Left: Scheme of the atmospheric neutrino production by cosmic-ray proton interactions in the atmosphere and the subsequent generation of pions and their decays to muons. Right: up-down symmetry for atmospheric neutrinos when oscillations in matter are not considered [3]

.

Muon and electron neutrinos are generated throughout the Earth's atmosphere as a function of altitude, with typical production heights of 18–20 km above sea level, and are emitted over a wide range of directions. As a result, the neutrinos that reach a terrestrial detector arrive from various zenith angles (angle between the detector vertical axis and the neutrino flux, as shown in the Fig. 8–right) and traverse different path lengths before reaching the instrument. Moreover, if oscillations are not considered, in sites A and B of Fig. 8, the same atmospheric flux of neutrinos would be expected due to an up-down symmetry in the zenith angle.

The flight distance between electron and muon neutrinos is not larger than 5% for neutrinos coming from above (not those traversing the Earth). The difference is so small since, at these energies, half of muon neutrinos are produced in muon decay, as well as electron neutrinos. Furthermore, for $E_\nu < 100$ MeV, the difference between the average vertical production height of muon neutrinos and antineutrinos coming from pions and that of neutrinos coming from muon decay turns out to be less than 1.5 km. At higher energies, when the parent muon energy is also higher and the muon can arrive at sea level without decaying, the difference in vertical production height also increases.

The expected atmospheric neutrino flux at sea level, apart from the details already explained, varies due to several factors. These include oscillations of ν_μ to ν_τ, matter-induced resonances for upward-going neutrinos crossing the Earth, the modulation caused by the solar cycle, or the effects of the geomagnetic rigidity cut-off. All these contributions and the associated flux uncertainties will be described in more detail in Section 4.1.1.

Atmospheric as well as supernova neutrinos can be detected in underground laboratories through their scattering with nuclei. As in the case of Dark Matter (Chapter 2), the detectors must be located underground to ensure adequate shielding from the cosmic-ray muon flux [3], [13], [23].

2 Dark Matter and the XENONnT experiment

This chapter will serve as an introduction to Dark Matter since is the main physics sought in the XENONnT experiment, covering the history of its postulation in Section 2.1, its main astronomical and cosmological evidence in Subsections 2.1.1 and 2.1.2, its main candidates proposed based on observations of its abundance and characteristics in Section 2.2, concluding with its three detection methods in Section 2.3.

Afterwards, the relevance of the XENON Dark Matter Project and its current XENONnT experiment, for the direct search for Dark Matter will be outlined. Section 2.4 provides the background of the XENON project by exploring the evolution of the experiments, from XENON10 to the currently installed at the INFN Laboratori Nazionali del Gran Sasso, XENONnT. Section 2.5.1 highlights the motivation and operation principle of the Time Projection Chamber detector whereas the discrimination techniques of backgrounds that contribute to this Dark Matter search, are examined in Section 2.5.2. Section 2.6 explains the whole XENONnT experiment components. Finally, the prospective of these type of experiments is covered in Section 2.7.

2.1 Hypotheses and Evidences of Dark Matter

Dark Matter, following the path of neutrinos, is one of the most elusive components of the universe, and it conforms approximately 85% of its mass and 26% [24] of its energy density. As neutrinos, it is electrically and color neutral, since neither electromagnetic interactions with photons nor detection of exotic isotopes have been observed. Its presence is instead inferred through the gravitational interaction with ordinary (and visible) matter, such as the rotation of galaxies or gravitational lensing [25], [26].

Since antiquity, the existence of an invisible matter, imperceptible to the observational techniques available at the time, has been suggested by philosophers such as Democritus and Epicurus, as well as by mathematicians, physicists, and astronomers. In 1844, Friedrich Bessel argued for the presence of both visible and invisible stars. Later, in 1922, the German astronomer Jacobus

Kapteyn described the Milky Way local density of matter in terms of the effective stellar mass, including non-observable stars through a luminosity-curve extrapolation.

Finally, in 1933, the Swiss astronomer Fritz Zwicky published a paper [27] in which he reported the velocity dispersion of galaxies in the Coma Cluster creating the roots of our current understanding of Dark Matter. Zwicky's study involved the measurements and estimates of the redshift, mass, dimensions and quantity of galaxies in the Cluster, which was used alongside with the Virial Theorem to obtain the total mass of the Cluster. When he compared the total mass with the estimated visible mass, he found that the latter one accounted for only a small fraction of the mass required to explain the observed gravitational effects (approximately 400 times smaller). This led him to suggest the existence of what he named "Dunkle Materie" or Dark Matter (DM).

Despite this evidence, Zwicky's hypothesis did not gain broad recognition until the 1970's, when Vera Rubin and Kent Ford studied the rotation curves of spiral galaxies and provided further support for DM. Similarly, gravitational lensing, which consists on light (coming from distant objects) bending around massive galaxy clusters, also reveals the presence of some invisible mass. From the cosmological point of view, the Cosmic Microwave Background (CMB) radiation provides an additional evidence to the presence of DM [28]. All these observations suggest that DM may play a crucial role in the composition, formation and evolution of the Universe, as will be shown below.

2.1.1 Astrophysical evidences of Dark Matter

So far, the enigmatic presence of Dark Matter has been introduced, mentioning the two most relevant astrophysical evidences of it, which take place in different cosmic scales, starting from galaxies which are defined as gravitationally-bound systems composed of stars and interstellar medium with typical dimensions of tens of kiloparsecs, up to galaxy clusters, which may be of the order of megaparsecs.

Spiral Galaxy Rotation Curves

Spiral Galaxies, which constitute about 70% of all known galaxies, present a flat disk with a central dense bulge, where most of the mass is concentrated, and spiral arms of stars rotating around the central supermassive black hole. One of these galaxies, M31 (Andromeda), was studied in the 1970's by Vera Rubin and Kent Ford, who measured the rotation velocities of stars, gas and dust as a function of their distance from the galactic center.

The rotation speed of stars and gas is typically measured through the monoenergetic 21 cm line emission of atomic Hydrogen and by observing the Doppler shift in the emission spectrum. In that way, astronomers can determine the speed of the gas and consequently, infer the rotation velocity of the galaxy.

According to Kepler's laws, which describe the orbital motion of an object around a central mass, the rotation curve is expected to increase approximately linearly with distance in the inner region and then to decrease beyond the radius of the bulge (approximated as a spherical distribution), following $v_r \propto r^{-1/2}$, as the density of the galaxy decreases.

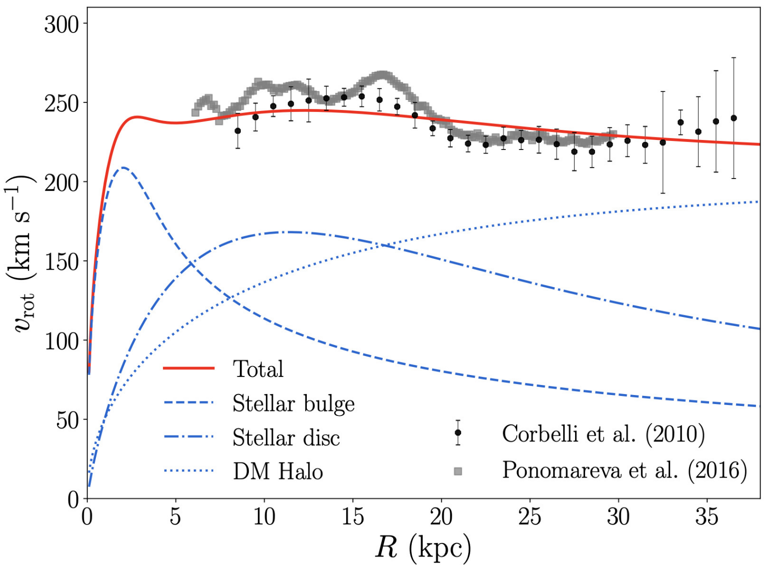

Figure 9: M31 Rotation Curve. The data points shown from two different studies come from hydrogen 21 cm emission. The model (red line) combines the rotational influence of the stellar bulge (dashed line), the stellar disc (dashed-dotted line) and the DM halo (dotted line), integrated in quadrature to construct the best-fit model to the observed data. Plot taken from [29].

However, as shown in Fig. 9, which exhibits more recent measurements of the M31 rotation curve, velocity remains approximately constant, implying that most of the galaxy's mass must reside in the halo as an invisible component. This halo, composed of invisible matter, extends well beyond the spiral arms of the galaxy and is consistent with the Navarro-Frenk-White (NFW) mass profile, which describes the density of the dark halo as a function of the radius r by the formula:

$$\rho(r) = \frac{\rho_0 R_S^3}{r(r + R_S)^2} \tag{14}$$

where $\rho(r)$ is the halo density, ρ_0 is the characteristic density and R_S is the scale radius.

These observation were later generalized to other galaxies, notably by Ken Freeman, who determined the radius at which the curve begins to decline for M33 (Triangulum Galaxy) and NGC 300 galaxies [30], [31].

Gravitational Lensing

Figure 10: Composite image of the Bullet Cluster (1E0657-558) released in June 2025. The vast number of galaxies and foreground stars in the image were captured by NASA's James Webb Space Telescope in near-infrared light. Hot X-rays captured by NASA's Chandra X-ray Observatory appear in pink. The blue represents the Dark Matter, which was precisely mapped by researchers with Webb's detailed lensing imaging. Credit: NASA, ESA, CSA, STScI, CXC [32]

This technique [33] consists of analyzing the light trajectory bending as it passes near a massive object, as predicted by Einstein's theory of General Relativity, according to which a sufficiently massive object can distort space-time.

Normally, gas, dust, stars, and Dark Matter are combined into galaxies, even when they are gravitationally bound within larger groups known as galaxy clusters. Most of the baryonic mass resulting from the collision of two galaxy clusters exists as sparse intergalactic gas, heated during the impact and emitting intensely in the X-ray spectrum. In the early 2000's, the X-ray spectrum of the frontal collision of two cluster, the Bullet Cluster was measured with the Chandra X-ray Observatory [34] and compared to the mass distribution obtained through gravitational lensing (shown in blue). The analysis revealed that the cluster center-of-mass was clearly deviated from the gas clouds observed though X-rays (shown in pink), as shown in Fig. 10. This provided a compelling proof that there was an additional non-baryonic component in the cluster, inferred from imaging distant objects lensed by the cluster, which remained unperturbed after the collision.

2.1.2 Cosmological evidences of Dark Matter

Cosmic Microwave Background Radiation

On the cosmological scale we also find observations of the primordial radiation originating from the matter–radiation decoupling that occurred in the early Universe about 380,000 years after the Big Bang, what we commonly know as the Cosmic Microwave Background (CMB).

Today, this radiation is observable in the microwave range of the electromagnetic spectrum, due to the expansion of the Universe over 13.8 billion years, and high-precision observatories like the one from the Plank collaboration, have obtained an image of this relic radiation. It provides us with a map of the early Universe displaying a nearly perfect blackbody spectrum with temperature $T = (2.7255 \pm 0.0006)$K and fluctuations of the order of 10^{-5} (see Fig. 11). The anisotropies observed imply the existence of acoustic oscillations in the primordial plasma, composed of baryonic matter, Dark Matter and radiation, caused by the contraction produced by matter (especially by Dark Matter) and the expansion driven by radiation.

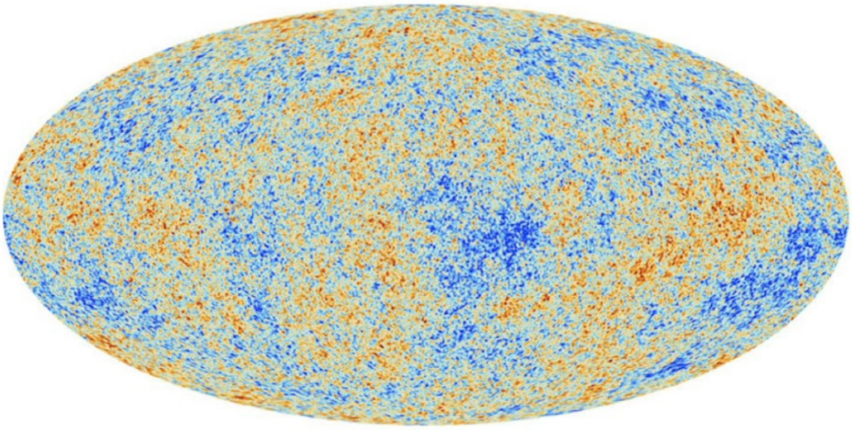

Figure 11: CMB anisotropies obtained by the Planck satellite. Different colors show different temperatures. Obtained from [35]

The ΛCDM (Lambda Cold Dark Matter) model describes the universe as flat, homogeneous and isotropic, undergoing accelerated expansion due to Dark Energy (Λ), and composed of Cold Dark Matter (CDM). The term Cold means that DM was produced thermally in the early universe and its speed was not relativistic when it decoupled from the primordial plasma. The model predicts the total energy density as:

$$\Omega_T = \Omega_\Lambda + \Omega_{DM} + \Omega_B \tag{15}$$

where Ω_Λ, Ω_{DM}, Ω_B represent the energy densities of Dark Energy, Dark Matter and Baryonic Matter, respectively.

Furthermore, the decomposition of CMB temperature fluctuations as a multipole expansion of spherical harmonics is a strong technique for testing the ΛCDM model, and over the last few decades, this angular power spectrum of the CMB has been analyzed by several experiments (see Fig. 12, where the measurements from four experiments are combined). In this representation, the expansion coefficients indicate the power spectrum associated with each multipole moment l, which are the order of the expansion and inversely proportional to the angular scale on the sky. This reveals the degree of correlation between one point and others separated by a given angle, as a function of the angular distance.

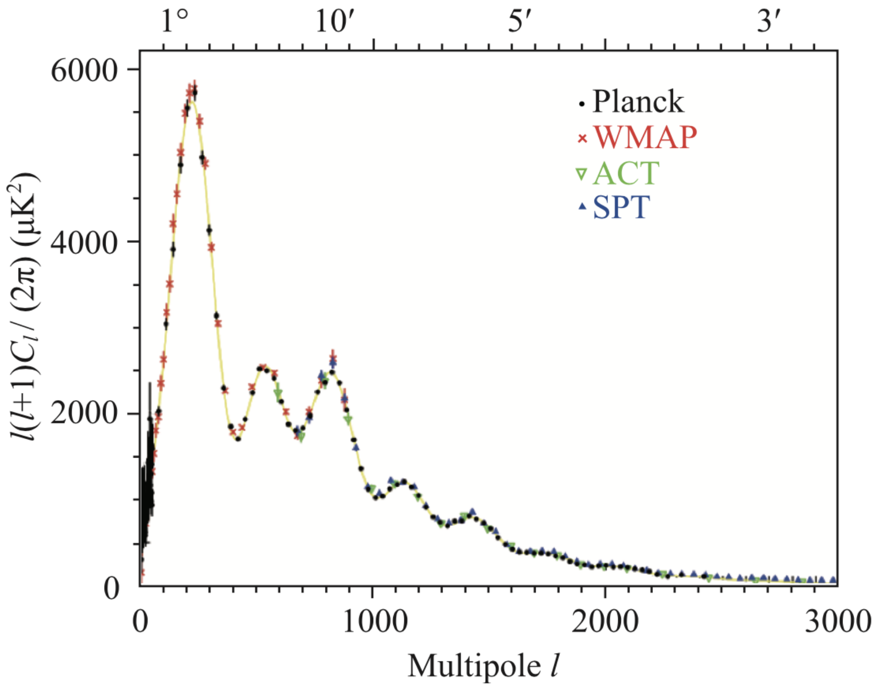

Figure 12: CMB anisotropy energetic spectrum in terms of the multipole l, which is the order of the temperature expansion of spherical harmonics and inversely proportional to the angular scale on the sky [36].

From the analysis of the second and third peaks, which correspond to the baryonic matter density and the combined baryonic and Dark Matter density, respectively, it is possible to estimate the Dark Matter density of the Universe relative to the critical density[4], ρ_c. The ESA Planck Cosmology Probe estimated in 2018 [24], from its final mission, the value of $\Omega_{DM} = \frac{\rho^0_{DM}}{\rho_c} = 0.2589 \pm 0.0057$.

The large-scale structure of the Universe

Further evidence supporting the DM hypothesis arises from Big Bang nucleosynthesis (BBN) and from N-body simulations of cosmic structure formation.

BBN, which governs the formation of light nuclei in the early universe, yields baryon density estimates consistent with those inferred from CMB observations.

---

[4] The critical density is the total energy density of an expanding universe with rate H_0 (current Hubble parameter) to have plane spatial sections (k=0) and is represented as $\rho_c = 3H_0^2/8\pi G$, where G is the Newtonian gravitational constant.

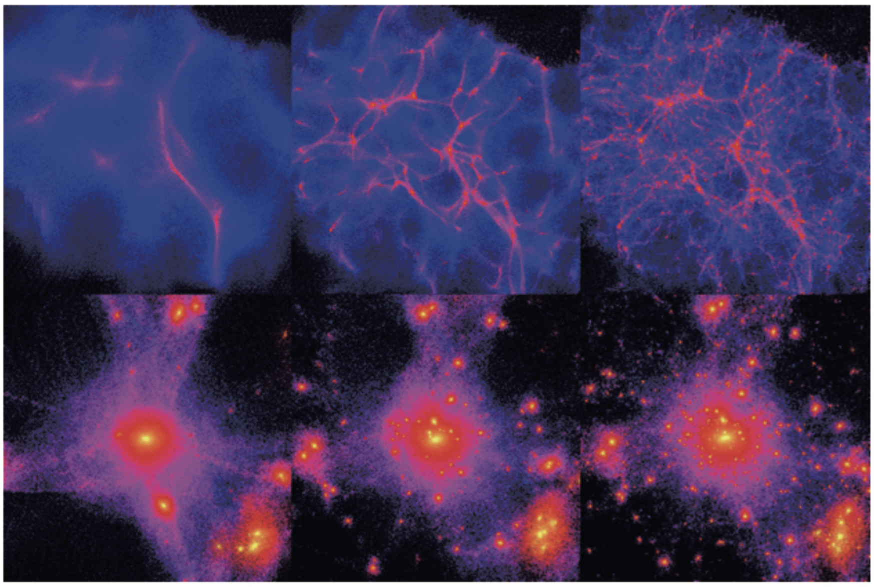

Figure 13: Numerical simulations of the large structure of the universe. Upper images show the cold dark matter model prediction whereas the lower ones, the hot dark matter model [31].

Meanwhile, N-body simulations, often initialized using the density fluctuations derived from the CMB, reproduce the observed large-scale distribution of galaxies, obtained by redshift surveys, with remarkable accuracy. These simulations emphasize the essential role of CDM in structure formation, providing the gravitational framework that enables baryons to cluster into the large-scale structures observed today, as illustrated in Fig. 13. In fact, the other scenario shown in the figure, corresponding to hot Dark Matter (HDM), composed of relativistic particles at the time of decoupling from the primordial plasma, is less consistent with the large-scale structures observed in galaxy surveys.

Together, these results constitute some of the strongest empirical support for the ΛCDM model, creating a solid foundation of the Dark Matter hypothesis and enabling the subsequent modeling of the preferred candidates to describe it [31].

2.2 Dark Matter Candidates

Dark Matter searches include a wide range of approaches, from theories that modify gravity to account for the evidences discussed in Section 2.1, such as galaxy rotation curves and the large-scale structure of the Universe; to baryonic candidates, like primordial black holes, neutron stars or white dwarfs. However, the most widely studied framework today is consistent with the ΛCDM model which focuses on non-baryonic candidates. These must satisfy several properties inferred from the aforementioned astrophysical and cosmological observations, making them the most viable possibilities:

- DM must be electrically and color neutral since since neither interactions with photons nor detection of exotic isotopes have been observed. It interacts via gravity and may perform weak interactions.
- It is stable or it has a lifetime greater than the age of the Universe in order to explain the abundance found in observations such as the CMB.
- It is slightly self-interacting, due to astrophysical observations of structure formation and cluster fusions.

Furthermore, other DM classification criteria can be considered, such as its production mechanism and kinematical properties. The former distinguishes between thermal production, in which the relic DM abundance decoupled from the primordial plasma and remained approximately constant until today, and non-thermal production in a period between the inflationary epoch and the matter-dominated era through the decay of other unstable particles.

The latter refers to the DM velocity at the time of the thermal decoupling, which would produce CDM, consisting of non-relativistic and massive particles (in the GeV/c^2 to TeV/c^2 range) or HDM, made up of relativistic and lighter particles. Warm DM (WDM) is also a possible candidate; but, as mentioned in Section 2.1.2, CDM assumed in the ΛCDM model is the most widely accepted one due to its implication on large-scale structure and formation of the Universe.

The interaction cross section and predicted DM mass are essential characteristics used to exclude or constraint different theoretical candidates in the parameter space by experiments. In fact, Fig. 25 shows the sensitivity plot obtained by different experiments in the mass-cross section parameter space.

So far, the properties that DM must satisfy in order to be consistent with observations have been introduced as well as the different possibilities of production mechanisms and kinematical conditions. Some of the candidates that satisfy some of these properties are introduced below [25], [26], [31], [37]:

WIMPs Weakly Interacting Massive Particles are the currently preferred CDM candidates which interact via the weak nuclear force and gravity. The first motivation of the WIMP paradigm is based on the fact that it agrees with the observed relic density at the freeze out, which suggests that DM particles should have a mass in the range from 1 GeV to about 100 TeV and an effective coupling at the electroweak (EW) scale or smaller with Standard Model (SM) particles. Other motivations come from beyond the SM theories requirements. The most important example of a theory that connects astrophysical and theoretical motivations, such as the hierarchy problem, is super-symmetry (SUSY) which provides an excellent DM candidate, the neutralino[5].

Axions They are very light particles ($1\ \mu\mathrm{eV}/c^2 \lesssim m_a \lesssim 1\ \mathrm{meV}/c^2$), originally introduced to address the CP-violation problem, and later found to be good Dark Matter candidates. They could form a CDM component, and their interaction with ordinary matter is expected to be extremely weak. The so-called solar axions are those produced in the core of the Sun through processes such as coupling with photons or photon–axion conversions in the Sun's magnetic field [38].

Sterile Neutrinos The difference with respect to those of the Standard Model is that they would only interact through gravity (although they do undergo oscillations in their flavor eigenstates). It has been determined that their mass must be greater than 10 keV [39].

2.3 Dark Matter Detection Techniques

There are three proposed approaches in the search for Dark Matter particles, as well as for gaining insight into their mass and weak interaction strength. Fig. 14 shows the three possible interactions between Dark Matter and ordi-

---

[5] The neutralino is the lightest SUSY candidate that preserves the R-parity, which transforms a fermion into its super-symmetric boson partner and vice-versa.

nary matter from the Standard Model (where SM represents a generic particle and its antiparticle), which are analyzed in each detection approach.

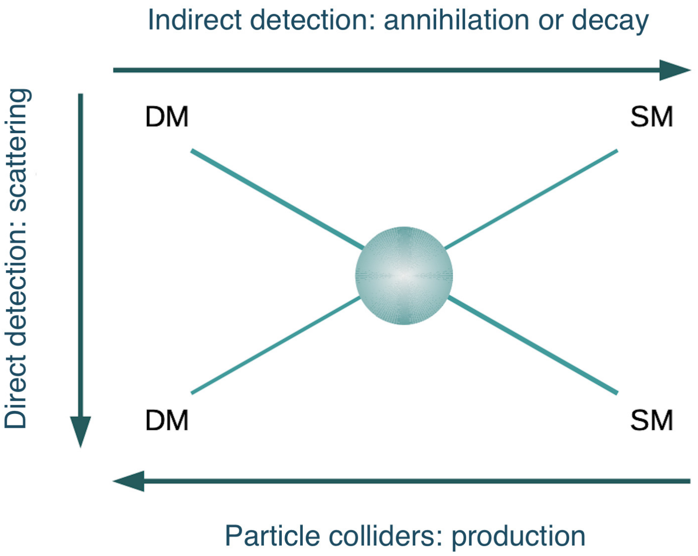

Figure 14: Scheme of the three different detection techniques with the corresponding interaction between DM and SM particles that is exploited in each of them.

Now, the principles of each detection method will be introduced and highlight some of the experiments that are or have been conducted within each domain.

Collider searches

The basis of the search for Dark Matter through colliders lies primarily in looking for Dark Matter via the high energy collisions, up to 14 TeV at the Large Hadron Collider (LHC), that could produce it. This is the main difference compared to other types of searches, which require different assumptions, such as the knowledge of the primordial abundance. However, this method also provides lower sensitivity than the others, even if it can be complementary in the low DM mass range.

One of the main signatures of Dark Matter sought in colliders is a missing transverse momentum[6] due to the possible presence of this matter, which would be produced alongside known SM particles, that would be searched as a recoiling jet or lepton (mono-X signature). Additionally, DM can be sought through the SM or dark mediators between SM and DM particles.

Some of the experiments dedicated to searches via high-energy colliders are those carried out at the LHC at CERN or the Tevatron at Fermilab. The collider that has provided results with the highest sensitivity is the LHC (through the CMS [40] and ATLAS [41] collaborations). Even if no signal of Dark Matter has been observed, the experimental program has only just begun. Specially at the future lepton colliders, where higher energies will be achieved with a cleaner environment than in hadron colliders, this search is expected to achieve much lower sensitivities [25], [26].

Indirect searches

This method focuses on the search for Standard Model particles produced by the annihilation or decay of Dark Matter particles in astrophysical regions known to have a high Dark Matter density, such as the central region of the Milky Way. Some of these detectable particles include gamma rays, neutrinos, and antimatter particles. The production rate of these particles essentially depends on the annihilation or decay rate, as well as on the density of particle pairs in the region of interest.

Experiments searching through gamma-ray observations include the Fermi Large Area Telescope [42] (LAT) in space and the ground-based Major Atmospheric Gamma-Ray Imaging Cherenkov [43] (MAGIC) telescope.

The search for an excess of antimatter particles in cosmic rays could also provide significant evidence for Dark Matter, given the baryonic asymmetry of the Universe and the relatively rare nature of such particles. Examples of antimatter detectors analyzing cosmic-ray fluxes include PAMELA [44] and AMS-02 [45]. The latter has been able to find an excess of positrons in the energy region above a hundred GeV [46], so upgrades to deeply study this high-energetic region are needed.

Neutrinos are also of great importance because WIMPs could interact within celestial bodies, increasing their local density and consequently the an-

---

[6] This technique is applied to search for particles that escape the detector due to their weak interactions but can appear as missing energy in the projection of momentum onto the plane transverse to the beam axis, where the total momentum is conserved.

nihilation rate. In such annihilations, most Standard Model particles would be absorbed within the celestial body (such as the Sun) through strong and electromagnetic interactions, unlike neutrinos. Therefore, the detection of high-energy neutrinos coming from the Sun could serve as a strong indicator of Dark Matter and allow an estimate of its mass. The IceCube [47] detector is one of the main experiments pursuing this goal [25].

Direct searches

Direct detection experiments aim to observe interactions between DM particles, that come from the Milky Way Halo with a velocity of $\sim 220\,\mathrm{km/s}$[7], and SM matter within ground-based detectors. When DM particles scatter off atomic nuclei or electrons, they can deposit a small amount of energy that is measurable as heat, light, or electric charge. Detectors are specifically designed to register these signals while minimizing external interference. In order to suppress this noise, coming from cosmic rays and natural radioactivity, experiments are conducted deep underground.

For most WIMPs, with typical masses between 10 and 100 GeV/c^2, interactions with atomic nuclei are more probable than with atomic electrons, a distinction that helps separate potential DM signals from background events. Different detection technologies are therefore optimized to discriminate between Nuclear Recoils (NR) and Electronic Recoils (ER), a crucial step in identifying DM-induced events. The elastic scattering cross section of DM off target nuclei can be expressed in terms of two contributions:

$$\frac{d\sigma}{dE_{NR}}(v) = \frac{1}{E_{max}(v)}\left(\sigma_{SI}F_{SI}^2(E_{NR}) + \sigma_{SD}F_{SD}^2(E_{NR})\right) \tag{16}$$

where E_{max} is the maximum recoil energy as a function of DM velocity. Then, we have the contributions from spin-independent (SI) interactions between DM particles and nuclei and from spin-dependent (SD) ones, both multiplied by their respective form factors, $F_{SI}(E_{NR})$ and $F_{SD}(E_{NR})$. These form factors account for the loss of coherence, suppressing cross section, with increasing momentum transfer, due to quantum effects.

One of the major challenges in direct detection is the mitigation of background signals from radioactive contaminants in the detector components, neutrons and neutrinos. Neutrons can closely mimic DM interactions by

---

[7] from the Standard Halo Model assumptions.

scattering off nuclei, potentially producing false positives. To counter this, advanced systems employ neutron vetoes and multiple-scatter identification techniques, since neutrons are far more likely than DM particles to cause multiple recoil events. Neutrinos pose an even more fundamental limitation: through Coherent Elastic Neutrino–Nucleus Scattering (CEνNS), they can generate nuclear recoils indistinguishable from those expected from WIMPs. As detector sensitivity improves, experiments approach the so-called "neutrino fog", a level beyond which neutrino-induced events dominate the background, making further discrimination extremely difficult.

Future experiments such as DARWIN (XLZD) [48] are designed to operate near this sensitivity frontier, demanding increasingly sophisticated background rejection methods. Despite the technological progress, no direct evidence for DM particle interactions has yet been found. The DAMA/LIBRA experiment [49], which uses thallium-doped sodium iodide crystals, has reported an annually modulating signal possibly compatible with DM, though this claim remains controversial and inconsistent with results from other detectors. The field continues to advance rapidly, and next-generation experiments are expected to probe the so-called "neutrino fog" [50], [51], [52].

2.4 The XENON Dark Matter Project

The XENONnT experiment is one of the cutting-edge direct detection experiments nowadays, after two decades of continuous progress. The XENON DM project, launched in 2002, is located at the underground INFN Laboratori Nazionali del Gran Sasso (LNGS), in central Italy, where it takes advantage of the natural cosmic radiation shield that the mountains provide in order to perform sensitive searches.

To achieve this sensitivity in WIMP direct detection, xenon-based dual-phase Time Projection Chambers (TPCs) are used. An evolution of the different TPCs in terms of its active mass, size and background levels is shown in Fig. 15. The first experiment, XENON10 [53], was operated between 2005 and 2007 with an active Xenon mass of 15 kg. This prototype demonstrated the long-term operational viability of these type of detectors, establishing an upper limit for the allowed WIMP-nucleon spin-independent cross section of 4.5×10^{-44} cm^2 [54] for a WIMP mass of 30 GeV/c^2, a factor of two better than the other experiments at that time.

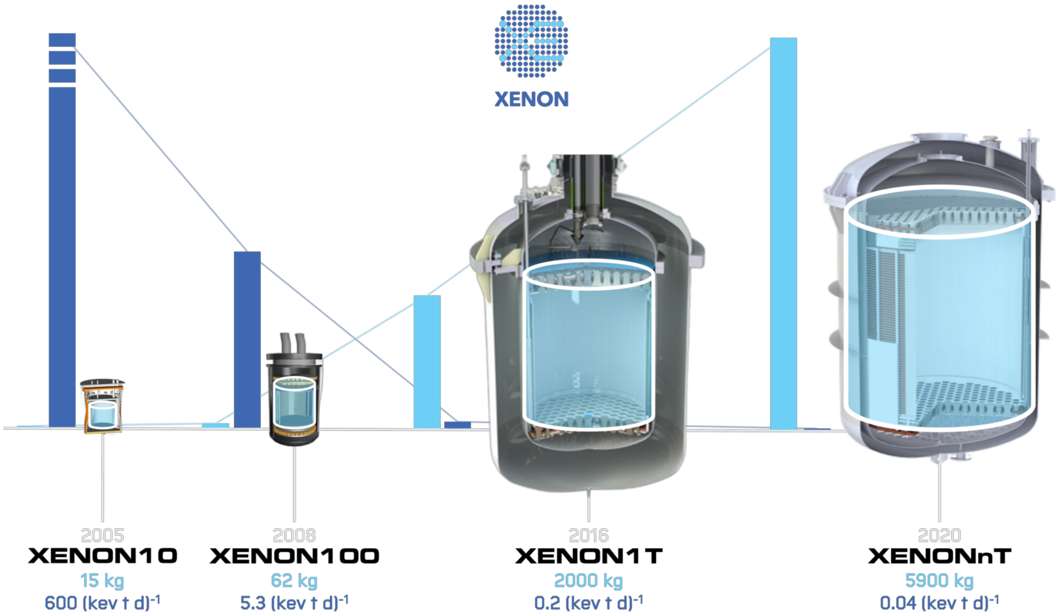

Figure 15: Visual representation of the XENON TPCs over the years, indicating the LXe active volume in kg (light blue) and the ER background level in units of (keV·t·day)$^{-1}$, measured in each experiment (dark blue).

Following this achievement, XENON100 [55] was installed in 2008 with an increased active mass of 62 kg of xenon. This experiment was the most sensitive detector from 2010 until 2014, boosting the sensitivity by an order of magnitude with regard to his predecessor. It was surrounded by 99 kg of liquid xenon used as an active scintillator veto for background rejection. This enabled the obtainment of an upper limit for the SI WIMP-nucleon cross section at 1.1×10^{-45} cm^2 for a 50 GeV/c^2 WIMP mass [56].

The first tonne-scale DM detector, XENON1T [57], operated between 2016 and 2018, with 2 tonnes of active xenon mass. From the analysis of two science runs and a fiducial volume (FV) of 1.3 tonnes an stringent upper limit on SI and SD WIMP-nucleon cross sections, with a minimum at 4.1×10^{-47} cm^2 and 6.3×10^{-42} cm^2, respectively, was reached for a 30 GeV/c^2 WIMP mass [58], [59].

The XENON program arrived to its fourth phase with XENONnT [60], which began data acquisition in 2020. This fast upgrade was possible due to the re-use of the infrastructure and sub-systems of XENON1T, only adding the new Neutron Veto system and changing the TPC and cryostat. The latest results from XENONnT, shown in Fig. 16, set a highly sensitive upper limit of 1.7×10^{-47} cm^2 on the WIMP-nucleon SI cross section, at 30 GeV/c^2 WIMP mass. These results are based on a total exposure of 3.5 tonne×year from the combined analysis of two science runs (SR0 and SR1) [61].

All these results have not only ensured the XENON program leadership in DM direct search but also broadened its scientific goals to new interaction channels and rare physics events, such as the previously mentioned cause of the "neutrino fog" [62], [63], [64].

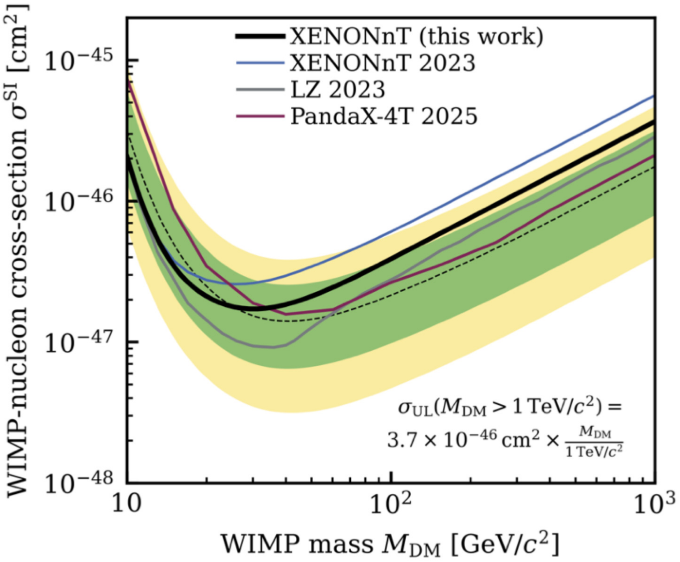

Figure 16: Upper limits on the SI WIMP-nucleon cross section (90 % C.L.) as a function of the WIMP mass (black line). The sensitivity band of 1σ (green shaded) and 2σ (yellow shaded) as well as their median (dashed line) are shown. In addition, results from XENONnT using only SR0 data, LZ, and PandaX-4T are included [61].

2.5 The dual-phase Time Projection Chamber working principle

The main reason why xenon is used for DM direct searches is due to its nuclear and chemical properties. In fact, xenon does not feature dominant intrinsic radioactivity, due to the amount of stable (or with half-lives greater than the age of the Universe) isotopes that it presents. Furthermore, the high atomic mass, A=131, enhances the SI interaction rate with WIMPs, as its cross section scales with A^2, and due to the fact that ^{129}Xe and ^{131}Xe isotopes have non zero spin, SD interactions can also be studied. Xenon density, of almost 3 g/cm^3, also provides a major advantage to these searches as it serves as a self-shield against backgrounds. On top of that, it remains in liquid state at moderated cryogenic temperatures since its boiling point (178 K) is higher, for example, than the argon one, simplifying compact designs. Finally, xenon its transparent to its own scintillation light, which is emitted in the VUV region (~175 nm), so neither wavelength shifters are needed.

More in detail, when a particle deposits energy in liquid xenon as ER or NR, part of it excites xenon atoms, which then form short-lived excimers (Xe_2^*) that de-excite emitting photons constituting the prompt scintillation signal S1. Simultaneously, ionization produces free electrons and positive ions, Xe^+, with a fraction of these electrons recombining and contributing further to S1. On the other hand, the ones that escape and drift upwards contribute to the ionization signal, S2. The scintillation light originates from transitions between the singlet and triplet states of xenon excimers, with characteristic decay times of about 4 and 27 ns, respectively. However, this temporal separation is too small to allow effective pulse shape discrimination between ERs and NRs, a method successfully used in liquid argon detectors due to its much larger time difference. In LXe detectors, the discrimination is based on the ratio between charge and light signals since NR produce shorter and denser energy tracks which favors recombination and thus light signal proportion with regard to the charge (or ionization) signal contribution [65].

2.5.1 The Dual-phase TPC Signal

As shown in Fig. 17, the TPC operates making use of three main electrodes, the anode set to a positive voltage, below it, the gate set to ground and at the bottom of the TPC, the cathode kept at a negative voltage. Due to these three electrodes a drift field of the order of 100 V/cm can be uniformly distributed parallel to z-axis in the LXe volume and an extraction field of approximately 10 kV/cm is equally distributed but along the LXe-GXe interface.

In this way, simultaneously to the prompt scintillation signal (S1) created when a WIMP crosses the TPC and excites a Xe atom, the electrons are released by ionization and moved toward the Xe liquid-gas interface thanks to the drift field. In this region they are accelerated by the extraction field, producing a delayed scintillation signal (S2) through electroluminescence.

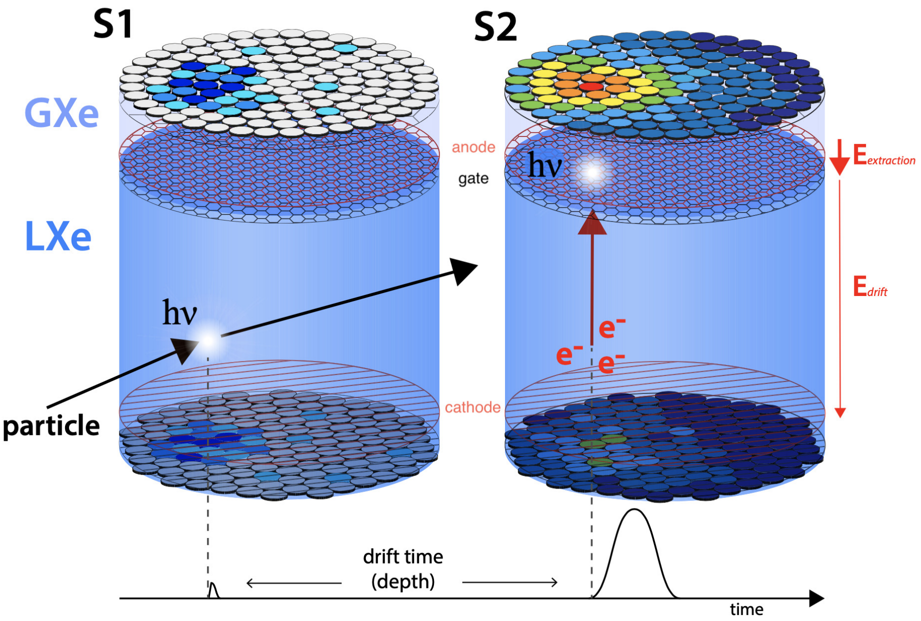

Figure 17: Schematic of the interaction between a particle crossing the XENONnT TPC and a Xe atom, creating S1 and S2 signals [50].

To detect these signals, top and bottom PMT arrays play a crucial role. S1 signal is collected by both arrays, on the other hand, S2 is mainly detected by the top array, where the xy position of the event can be estimated through its PMT distribution. Furthermore, as shown in the bottom part of Fig. 17, from the time difference between S1 and S2, drift time and thus the z position in the TPC can be obtained if the electron drift velocity is known. All this enables the TPC to perform the 3D reconstruction of an event and that is why it is called Time Projection Chamber.

As previously mentioned, from the charge/light or S2/S1 ratio, ERs and NRs can be distinguished, as shown in Fig. 18. Moreover, analyzing the number of S2 peaks in a single event, multiple scatterings (MS) and single scatterings (SS) can be classified, which is essential to distinguish expected WIMP events from background events, as will be mentioned in the next subsection.

The corrected signals, cS1 and cS2, shown in Fig. 18 axes, account for detector effects influencing the size of the observed signals. Their relationship is described by the parameters g1 and g2, which parametrize the number of light and charge quanta collected relative to those generated by energy deposition during the interaction. They are derived from the anti-correlation between S1 and S2 using mono-energetic calibration sources. The deposited energy is reconstructed as

$$E_{dep} = W \times \left(\frac{S1}{g1} + \frac{S2}{g2} \right) \tag{17}$$

where W is the average energy required to produce one scintillation photon or an ionized electron. Additionally for nuclear recoils, the Lindhard factor corrects for signal quenching due to heat loss. Discrimination between ER and NR events is characterized by the ER-leakage parameter, which improves at higher drift fields. Typically, values of about or more than 99.5% of ER discrimination and about 50% of NR acceptance are achieved with this type of detectors.

To sum up, the TPC design of XENONnT enables accurate 3D reconstruction and event selection within the fiducial volume, effectively suppressing background and enhancing Dark Matter search sensitivity [50], [66].

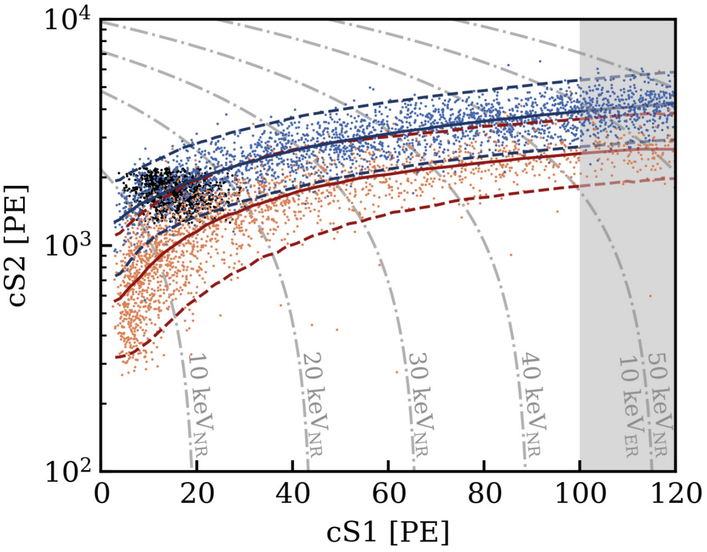

Figure 18: NR and ER bands obtained with calibration data from ^{241}AmBe (orange), ^{37}Ar (black) and ^{220}Rn (blue). The median (solid lines) and the ±2 σ contours (dashed lines) are also shown in red and blue respectively. The dash-dotted gray lines show the NR energy [66].

2.5.2 Background Rejection in XENONnT

In extremely rare event searches is essential to mitigate and discriminate the background events from those of interest. Firstly, the recoil type discrimination is exploited to distinguish ER background events from a typical WIMP signal. In fact, the signal created by WIMPs crossing the XENONnT TPC is expected to be a single scatter with a xenon nucleon (NR) and within the FV. Therefore any NR single scatter or ER events, whose S2/S1 ratio lies in a region also populated by NR signals, provide a dangerous signal that can mimic the WIMP signal.

Electronic Recoil Background

Detector components contribute to the low-energy background through single Compton scattering, forming an almost flat spectrum below 200 keV (materials curve in Fig. 19–left). The main contributors to this background are the cryostat vessel and the PMTs, via γ and β radiation.

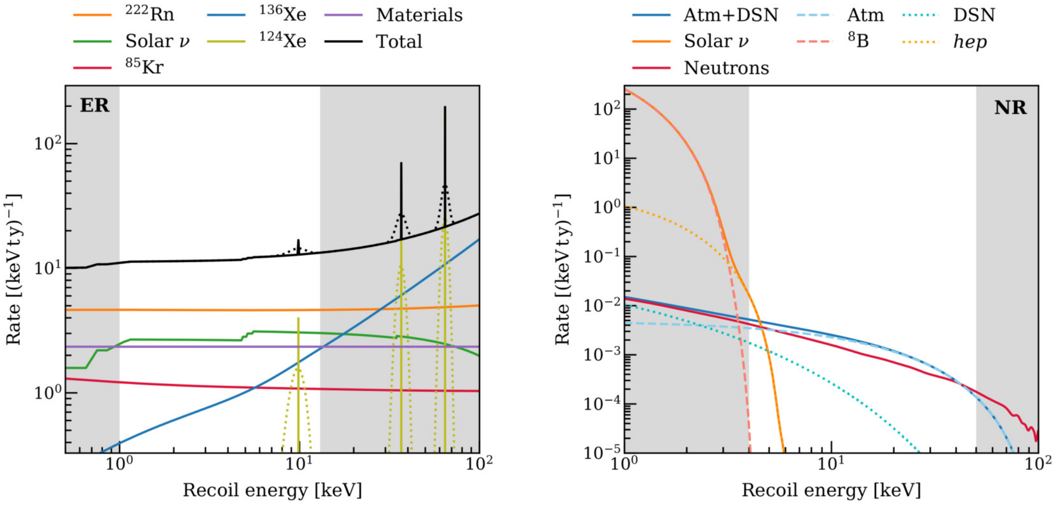

Figure 19: Energy spectra of ER (left) and NR (right) backgrounds expected in the TPC FV. The white areas highlight the ROI for the standard SI WIMP search. The dotted lines in the total ER rate represent the Gaussian smearing of monoenergetic lines [50].

^{222}Rn, ^{85}Kr and xenon isotopes ^{136}Xe, ^{127}Xe and ^{124}Xe are intrinsic sources of background uniformly distributed in the LXe volume, since γ and β radiation are present among their decay products, contributing to the ER signal. Some sources can be reduced through their dedicated distillation, whereas the other contributions can be estimated based on their half-lives. As displayed in Fig. 19, the largest contribution to ER background in the ROI comes from radon.

Solar neutrinos produced mainly through pp fusion and ^{7}Be electron capture, interact with atomic electrons in the FV, leading to a significant contribution to the ER background, given the impressive reduction of ^{222}Rn, ^{85}Kr contributions achieved in XENON1T and XENONnT.

Nuclear Recoil Background

Radiogenic neutrons in the MeV range are produced by spontaneous fission and (α,n) reactions in detector materials, such as the cryostat, PMTs, polytetrafluoroethylene (PTFE) components and others, mostly producing events in the outer layers of the active volume. Due to the unprecedentedly low ER background reached (0.04 $(\text{keV} \cdot t \cdot d)^{-1}$ as shown in Fig. 15), the NR background from radiogenic neutrons becomes more relevant in the search for WIMPs, and thus an additional mitigation strategy is mandatory since they can mimic a WIMP-like signal (they can produce a SS NR inside the FV). Fortunately, since most of the radiogenic neutrons that produce a signal inside the TPC exit the cryostat, these can be tagged by the NV profiting the synchronization between TPC and NV DAQs. When they produce MS or scatter outside the FV their discrimination is easier.

Cosmogenic neutrons which are induced by cosmic muons interacting, e.g. through spallation, with the surrounding rock and concrete can be tagged using the active MV. Furthermore, even if this contribution is negligible with respect to the radiogenic one, it can be further suppressed by the NV tagging.

CEνNS produced by solar, atmospheric and diffuse supernova neutrinos contributes to the NR background as shown in Fig. 19 with a signal that is exactly the same to that of WIMPs, due to their low interaction cross section. Solar neutrinos, from ^{8}B and hep decays, affect the sensitivity to light WIMPs whereas atmospheric and diffuse SN neutrinos contribute at higher energies. In 2024, the first XENONnT results of ^{8}B solar neutrinos [64] were published by the XENON collaboration, with a measured flux consistent with results from SNO and a background-only hypothesis rejected with a statistical significance of 2.73σ. This was the first direct measurement of nuclear recoils from solar neutrinos [65], [66].

2.6 The XENONnT Experiment

XENONnT is situated in Hall B of the INFN LNGS since 2020, when the installation of its detector systems was completed after less than a year.
The different subsystems that compose XENONnT are shown in Fig. 20. In the core of the stainless steel Water Tank (WT), the Time Projection Chamber (TPC) is surrounded by the Neutron Veto (NV) detector. This detector is immersed in Gadolinium[8]-loaded water, since Science Run 2 (SR2), to enhance neutron capture and reduce its associated radiogenic background. The WT is equipped with 84 PhotoMultiplier Tubes (PMTs) serving as an active water Cherenkov Muon Veto (MV) apart from being a passive shield for the TPC against cosmic muons. Other systems are also shown, such as the Gadolinium-Water Purification System, the Xenon storage and recovery (ReStoX), the distillation (Rn, Kr) and purification (LXe, GXe) systems.

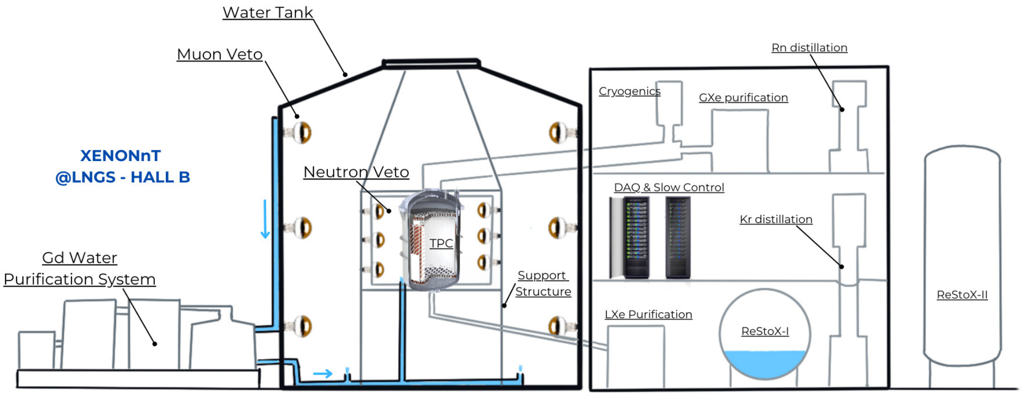

Figure 20: Scheme of the XENONnT experiment and its subsystems.

2.6.1 Dual-phase Time Projection Chamber and Cryostat

The core of the XENONnT experiment is the dual-phase Time Projection Chamber containing liquid Xenon (LXe) with a small gap of gaseous Xenon (GXe) above it, and which in turn is enclosed by an inner and an outer stainless-steel cryostat vessels, as shown in Fig. 21. It contains a total of 8.6 tonnes of Xenon at ∼-96°C, from which 5.9 tonnes serve as an inner active detection volume, whereas the rest acts as a passive shield against radioactive emanations

---

[8] Gadolinium is the element with the highest thermal neutron capture cross section.

from detector materials. The cylindrical active region is 1.613 m high and 1.327 m wide, with about 4.5 tonnes belonging to the FV.

It possess a top and bottom PMT arrays: the former is instrumented with 253 low-background 3" Hamamatsu R11410-21 PMTs while the latter holds 241 PMTs of the same type. These PMTs are selected for their low radioactivity and efficiency in detecting Xe scintillation light.

The inner walls of the TPC are covered by poly-tetrafluoroethylene (PTFE) panels to enhance the sensitivity by maximizing the Xe scintillation light (UV photons) detection. Five electrodes made of stainless-steel wires are situated near the top and bottom arrays to generate the electric fields required to transport the charge signal (already introduced in Section 2.5.1) along the TPC. The cathode is situated at the bottom region, the anode at the top one (orange and blue zoomed pictures of Fig. 21, respectively) 3.0 mm above the gate electrode, which, in turn, is located 5.1 mm below the liquid-gas Xe interface. Two additional electrodes, the top and bottom screens, are situated above the anode and below the cathode, respectively, in order to shield the PMTs from the high electric fields created by the electrodes.

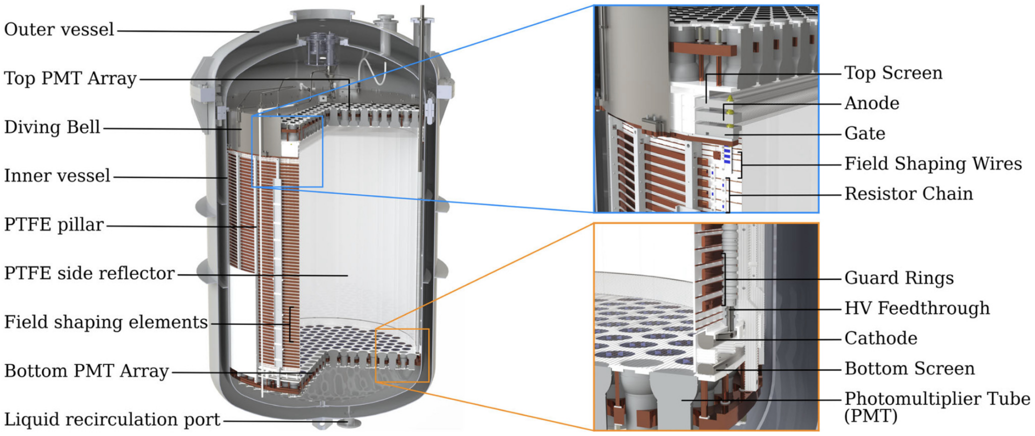

Figure 21: CAD rendering of the XENONnT TPC within the cryostats. The blue zoomed picture shows the top configuration of the electrodes, while the orange one displays the bottom configuration as well as the bottom PMT array [60].

The designed drift field in the LXe volume was 191 V/cm and the extraction field in the GXe one was intended to be 5-10 kV/cm. However, during commissioning in November 2020, a short circuit between the cathode and the bottom screen caused by a screen electrode wire breakage (discovered during the XENONnT upgrade), limited the cathode voltage thus reducing the average drift field to 23 V/cm. Even though, the drift field strength was enough to operate the TPC. Moreover, the extraction field resulted in 2.9 kV/cm [50], [60].

2.6.2 Water Cherenkov Veto Systems

XENONnT benefits from two veto systems, the Neutron and Muon Vetoes, shown in Fig. 22 which, when used in coincidence to the TPC, allows for a further reduction of neutrons that could potentially mimic a dark matter signature and muons. It should be noted that, when used as vetoes, the MV and NV induce a loss of around 1% to the TPC live time during regular science runs.

Both vetoes act as water Cherenkov detectors to collect the light created by charged particles crossing the WT or the NV with their respective PMTs. One important point to note is that they only measure the amount of Cherenkov light generated by these particles; they do not reconstruct its direction from the Cherenkov ring, as detectors like Super-Kamiokande do.

Muon Veto Detector

Inherited from XENON1T, the MV is built inside the WT which has a diameter of 9.6 m and a height of 10.2 m, and is filled with ~700 tonnes of demineralized or Gd-loaded water. The MV is equipped with 84 Hamamatsu R5912ASSY 8" PMTs sealed to be operated in water and distributed in five vertically equidistant rings and featuring ~30% QE over the wavelength range between 300 and 600 nm.

The MV ensures a tagging efficiency of 99.5% for muons and $\sim\ 50\%$ for shower events created by muons interacting outside the WT, since cosmic muons deposit a enough amount of energy to detect the light produced, even if the veto does not have a large PMT coverage. Furthermore, to increase Cherenkov light detection, the walls of the WT are covered by reflective foils with more than 99% of reflectivity to wavelengths between 400 and 1000 nm. Due to these results, the impact of NRs from cosmogenic neutrons on the WIMP sensitivity was reduced to a negligible level [60].

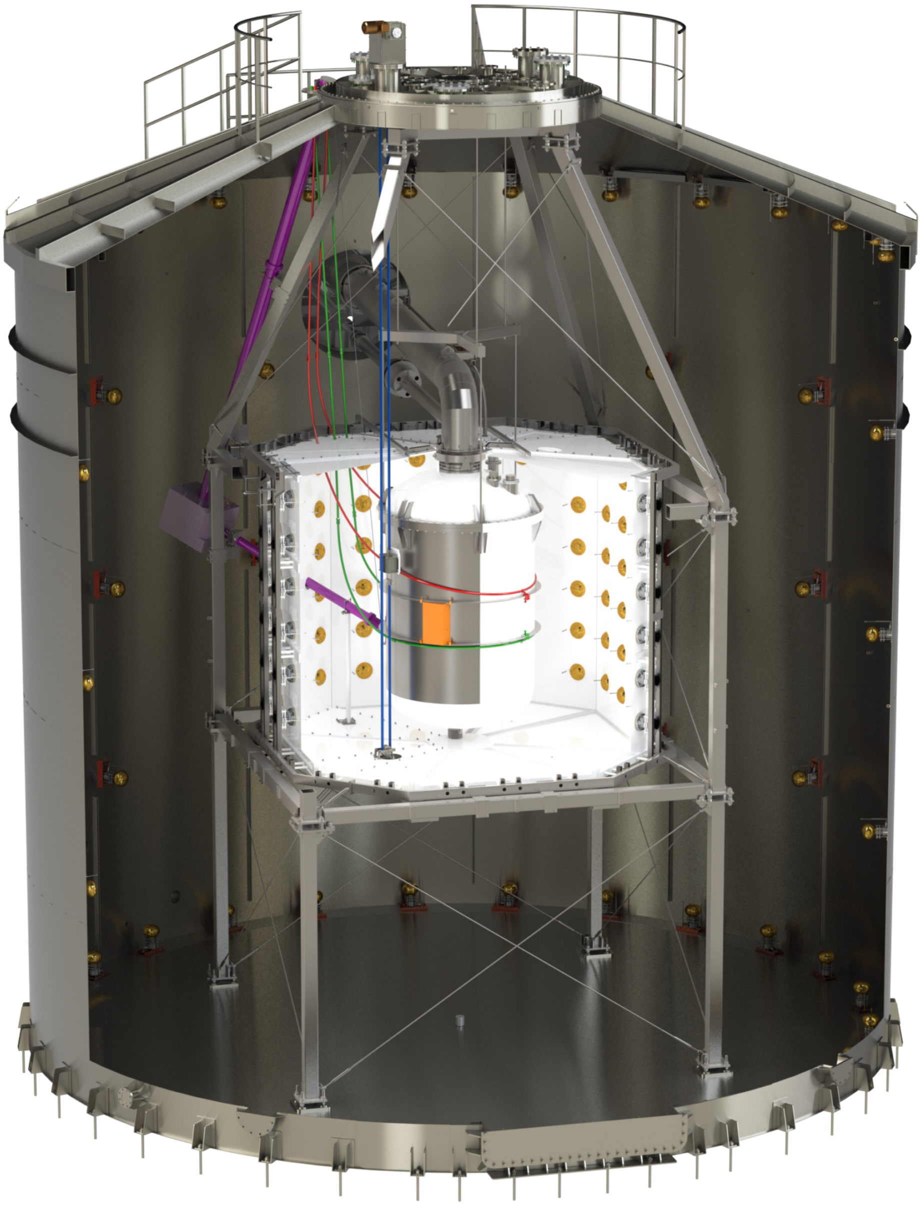

Figure 22: CAD rendering of the NV surrounding the TPC cryostat in the center of the WT, covered with reflector foils, and the MV. The main elements are the support structure (grey), the ePTFE panels (white), and the PMTs (yellow) with their calibration rods. The main components of the calibration system entering the NV are also shown: neutron generator pipe (purple), I-belt (blue), and U-tubes (red and green) [67].

Neutron Veto Detector

An indispensable upgrade of XENONnT, the Neutron Veto, is located between the cryostat and the WT, as shown in Fig. 22. It has a 40 m^3 volume (containing 34 m^3 of water) confined by reflectivity panels made of expanded PTFE (ePTFE) anchored by thin stainless steel bars, to minimize backgrounds. The reflectivity of the ePTFE panels is $> 99\%$ for optical and UV photons. The panels form an octagonal prism with a height of 3.16 m, and sides length of 2.02 m or 1.22 m. The wide and narrow sides are positioned at radial distances of 1.87 m and 2.05 m from the center, respectively. The NV floor consists of eight triangular sections that close the entire surface, while the ceiling is composed of eight individual triangles, anchored to a ring surrounding the main central pipe. Furthermore, the ceiling includes three ports: two circular openings, each with a 23 cm diameter, allowing the insertion of a neutron generator, and a third rectangular port (23×27 cm^2) designed to allow the insertion of a tungsten shield containing a calibration source for the TPC calibration. These ports allow photons to travel across the surface that separates the NV and the MV, making the detection of photons coming from events created in the other veto possible.

Cherenkov photons are detected by 120, low radioactivity, 8” Hamamatsu R5912-100-10 PMTs (with maximum QE of 39% at 350 nm) arranged in 20 columns of 6 PMTs each. Wide sides host three PMT columns and narrow sides two, with only the glass window inside the NV volume, so the impact of backgrounds produced by radioactivity of the PMT body is reduced by 40%, as this source dominates the background rate in the NV.

The Neutron Veto detects neutrons through their capture in pure water or on Gadolinium, after being thermalized in water. Thermal capture in pure water is characterized by an average capture time of about 200 μs, with a subsequent de-excitation emission of a 2.2 MeV photon, as shown below:

$$\mathrm{H} + \mathrm{n} \rightarrow {}^{2}\mathrm{H}^{*} \rightarrow {}^{2}\mathrm{H} + \gamma \text{ (2.2 MeV)} \tag{18}$$

On the other hand, one of the isotopes of Gadolinium providing the most relevant contribution to the total thermal neutron capture cross section, ^{155}Gd, emits 3 or 4 photons with a total energy of about 8.54 MeV when ^{156}Gd returns to its ground state. In this way, the average capture time can be reduced to ~30 μs with a Gd mass concentration of 0.2%. The process through which Gadolinium captures a thermal neutron and subsequently emits γ-ray's is:

$$^{155}\text{Gd} + \text{n} \rightarrow {}^{156}\text{Gd}^{*} \rightarrow {}^{156}\text{Gd} + \gamma\text{'s (8.54 MeV)} \tag{19}$$

The resulting photons interact through Compton scattering, producing secondary electrons that emit Cherenkov light. This technique of tagging neutrons was already successfully deployed by large-scale water-based neutrino experiments like Super-Kamiokande and SNO+.

During SR0 and SR1, before the insertion of gadolinium, the neutron detection efficiency was (82 ± 1)% if a coincidence time window of 600 µs is used; this is the highest neutron detection efficiency ever achieved in a water Cherenkov detector. This enables a tagging efficiency, which additionally requires that the neutrons interact first inside the TPC producing a single scatter NR (WIMP-like signal), before exiting and being captured in the NV, of (53 ± 3)%, inside a tagging time window of 250 µs between TPC and NV.

Afterwards, at the end of 2023, when SR2 started, the water in the WT was doped with Gd-Sulphate-Octahydrate ($Gd_2(SO_4)_3 \cdot 8(H_2O)$ or simply GdSO), at a concentration of 0.05% in salt mass, achieving an increase of the tagging efficiency up to ~ 78% for the same time coincidence window of the SR0 analysis. Furthermore a reduction of the neutron capture time was also observed.

Future operations will increase the Gd salt concentration to 0.5%, which will further improve the performance of neutron tagging to around 87% thanks to the increased capture cross section, the related decrease in capture time, and the increase in the total amount of energy released [60], [67].

2.6.3 Xenon Handling and Purification

The ton-scale Xe TPC volume requires an advanced system for Xe handling and purification to achieve and maintain the purity and low background levels. A LXe purification plant and a Radon distillation column were implemented to achieve these requirements. The xenon handling system consists of the following components (shown in Fig. 20) [60]:

- **Cooling system**: similar to the one used in XENON1T, the cooling and temperature control system is based on a "remote cooling" approach, since it makes use of a vacuum-insulated pipe linking the cryostat to a external cooling station. Moreover, a battery-powered liquid nitrogen cooling system is present to ensure stability in case of brief power outages.

- **Xenon storage and recovery**: the cryogenic plant includes two storage units, ReStoX-I (developed for XENON1T) and ReStoX-II, being capable of storing 7.6 and 10 tonnes of xenon at room temperature, respectively. These units are vital, since are able to fastly recover both LXe and GXe during emergencies.

- **Electronegative impurity removal**: impurities like O_2 or H_2O reduce the number of electrons available for the charge signal during their drift, thus their reduction is essential to maintain TPC's detection efficiency. Therefore, in XENONnT was added a LXe purification system apart from the GXe one present in XENON1T. Their effectiveness is quantified thanks to the electron lifetime, which has reached values up to 10 ms, compared to 650 µs in XENON1T.

- **Krypton and Radon distillation columns**: krypton and radon have some isotopes that contribute significantly to the background radiation of the detector. ^{85}Kr beta decays complicate the search in the low-energy region, whereas ^{222}Rn emanated by the detector materials leads to a uniform distribution of its decay products throughout the LXe volume. The former is removed by exploiting differences in vapor pressures. The latter, on the other hand, is integrated in the LXe recirculation loop, distilling both LXe and GXe, reducing in that way radon concentration. Due to these systems, ER background has been reduced by a factor 5.

2.6.4 Gadolinium-Water Purification System

The Cherenkov emission process in the Neutron Veto produces relatively few photons, making the transparency of the water and the reflectivity of the detector walls critical for detection efficiency. While high reflectivity is achieved through ePTFE panels, maintaining water transparency requires continuous purification. Until October 2023, the NV used demineralized water purified by the Water Loop Plant (WLP) inherited from XENON1T, which removes ions and bacteria that degrade optical performance. The system includes sensors for pressure, temperature, flow, and resistivity (key indicator of water purity), which typically is 18.18 MΩ· cm at 25 °C.

However, the introduction of gadolinium for neutron capture complicates purification, since conventional systems would also remove valuable Gd ions. To address this, the Gadolinium-Water Purification System (GdWPS) was developed to integrate and dissolve Gd sulfate into the NV and eventually the MV, maintain its concentration over time, and preserve the optical properties of water.

The performance of the GdWPS has been proven to be optimal in purifying water even without gadolinium loading. Furthermore, via transparency measurements conducted on samples of the gadolinium plant, the water transparency was found to be nearly equivalent to that of demineralized water. Finally, in October 2023 the GdSO insertion in the WT started. Furthermore, water transparency and wall reflectivity were regularly monitored using the reflectivity monitor of the NV (described in Section 2.6.5) which showed, in December, a significant decrease in light collection of ~20% after a significant Gd sulfate injection. As later discovered during the XENONnT upgrade (Section 2.6.7) [60], [68], this was due to few rusted bolts (evidently not stainless steel as required) which caused a deposit of rust on a small portion of the surface of some ePTFE reflective panels.

2.6.5 Calibration Systems

Calibration systems are essential for characterizing the TPC and veto detectors responses to different radiation types, enabling accurate event and energy reconstruction and ER/NR discrimination. These systems are divided into internal and external calibrations.

Internal calibration uses injected radionuclides to uniformly distribute known sources throughout the xenon volume, allowing precise mapping of the active volume. The main isotopes, which must have sufficiently fast decay times, are:

- **^{83m}Kr:** Introduced through the xenon recirculation loop, this metastable isotope (half-life 1.83 h) emits 32.2 keV and 9.4 keV conversion electrons. It calibrates mono-energetic peaks in the WIMP region of interest (ROI) and monitors light and charge yields, as well as electron lifetime.
- **^{220}Rn:** Produced from a ^{228}Th source, it emits α, β and γ particles. Its decay product ^{212}Pb provides a β spectrum useful for calibrating the low energy ER band. Due to its longer half-life, it is used at the start or end of science data runs.

- **^{37}Ar:** Emits 0.27 keV and 2.8 keV X-rays and is used to characterize the detector response near the low energy threshold. With a 35-day half-life, it is typically used at the end of science data runs and later removed by distillation.

External calibration places sources outside but near the cryostat to target specific detector regions. The main systems employed are:

- **L-shaped beam pipe:** Provides collimated neutron beams from a neutron generator which, when used with heavy water, is useful for low-energy NR band calibration, near the threshold. Shown in purple in Fig. 22.
- **I-belt :** Moves a tungsten collimator with a ^{88}Y–Be source along the cryostat to emit low-energy neutrons and γ rays. Displayed in blue in Fig. 22.
- **U-tubes:** Two stainless steel tubes guide external sources (e.g., AmBe, ^{232}Th) around the cryostat for TPC and NV calibration at different heights. Depicted in green and red in Fig. 22.

Light Calibrations

Weekly calibrations include low-intensity LED light pulses to monitor TPC, MV and NV PMTs gain, afterpulses and noise levels. This calibration is performed thanks to optical fibers leading to each PMT with a PTFE diffuser at the end of each fiber to optically couple the fiber to the PMT. Then by illuminating with blue light (470 nm), the characterization and monitoring of the single photoelectron (SPE) response of the each PMT can be performed, individually.

On the other hand, ”diffuser balls” employed in the NV and MV are illuminated by short laser pulses to characterize the timing, water transparency and ePTFE surface reflectivity.

Also, a reflectivity monitor set up to illuminate the NV ePTFE walls, installed at about half height on the inside of one of the NV lateral sides, is used to monitor the optical properties of the NV. The monitor consists of four optical quartz fibers fed by another laser that emit photons at a wavelength chosen to probe near the maximum of the convolution of the NV PMTs quantum efficiency and Cherenkov emission spectrum in water [60], [67].

2.6.6 Slow Control, DAQ, Computing and Processing

The **Slow Control (SC)** system of XENONnT is responsible for the continuous monitoring and control of all detector subsystems. It integrates Programmable Automation Controllers (PACs) with industry-standard Cimplicity SCADA software to automate cryogenic management, adjust PMT high voltages, and execute optical calibration sequences. Recent upgrades expanded the system to include xenon purification, the radon distillation column, ReStoX-II, and the NV with all its subsystems. All monitored parameters are logged and used to trigger alarms or notifications in case of anomalies.

The **Data Acquisition (DAQ)** system handles signals from all PMTs across the three sub-detectors: 494 in the TPC, 84 in the MV, and 120 in the NV, totaling 698 channels. The DAQ operates in a quasi-triggerless mode, digitizing PMT signals above defined thresholds and ensuring synchronized data collection among the three detectors. The signals are amplified, digitized, and directed to a unified storage system that allows integration and subsequent data processing.

The MV subsystem employs CAEN V1724 digitizers with 14-bit resolution, and a 100 MSamples/s sampling rate. Signals from the 84 PMTs are recorded whenever a predefined trigger condition is met: at least five PMTs must exceed a threshold of approximately one photo-electron (Single PE, SPE) within a 300 ns coincidence window. Once triggered, the waveforms are recorded over a 5 μs window, including pre- and post-trigger samples. The data are subsequently processed through a multi-step logic chain of Python-based plugins that produce progressively higher-level data types.

On the other hand, the NV employs eight CAEN V1730 digitizers, each with 16 channels, 14-bit resolution, and a 500 MSamples/s sampling rate. The system operates in a self-trigger mode: when the signal in a channel exceeds a fixed threshold (typically 15 ADC counts), a waveform is recorded within a time window adding some samples before and after the trigger, forming a hitlet. This fast sampling rate, five times higher than that of the TPC, enables reconstruction of the prompt Cherenkov photon arrival times before wall reflections.

Raw waveforms are processed using the **strax** and **straxen** software frameworks, which identify and group signals through the use of plugins. The first step in the software trigger involves detecting PMT hits that surpass the same channel-specific thresholds as the one from DAQ, followed by coincidences requiring at least three hits within a 600 ns window to discriminate real Cherenkov events from dark counts. Each window is extended by an additional pre-trigger window. Then, in offline processing, time windows can be reduced to 200 ns, since the typical time spread of a Cherenkov signal is about 60 ns, requiring at least three hitlets within this event window. These hitlets are formed to include the leading edge and tails of each PMT hit, that are extended by 3 and 15 samples, before and after, respectively, as shown in Fig. 23. For each event, key quantities are computed, such as the total signal area, the center time (area-weighted mean arrival time of the hits), and the reconstructed position, determined from the distribution of hitlets before position diffusion due to ePTFE reflections.

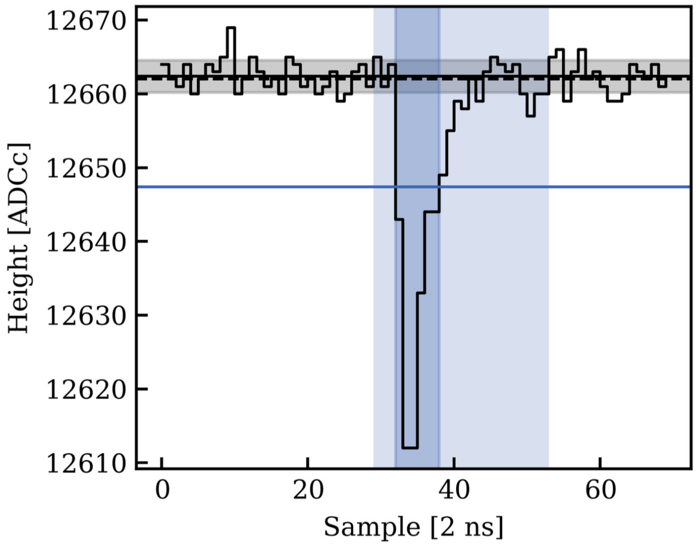

Figure 23: SPE waveform signal recorded in a NV PMT. The black solid and dashed lines represent the baseline as estimated by the digitizer and the processing software, respectively. The black-shaded region indicates the baseline RMS. The blue horizontal line shows the threshold below the baseline. All consecutive samples below this line are marked as a hit (dark blue shaded region). Whereas the light blue shaded region indicates the so-called hitlet [67].

All acquired and processed data are temporarily stored on local LNGS servers before being transferred to **remote storage centers** in Europe and the USA. Backup copies are backed-up on tape at CNAF (Italy), ensuring long-term data preservation and accessibility for offline analysis [60], [67].

2.6.7 The XENONnT Upgrade

During 2025, an upgrade of the XENONnT detector was carried out after the collaboration decided to stop data taking in order to repair several detector components. The main goal of this upgrade was to replace the electrodes so that the drift field could operate at its design value of 191 V/cm, as mentioned in Section 2.6.1. The expected benefits of the electrode repair include improved ER/NR discrimination and higher field uniformity, which in turn would allow for a larger fiducial mass, among other effects.

The water tank was opened on May 5th, and since then the disassembly and subsequent reassembly of the various XENONnT subsystems have been underway. During the Neutron Veto disassembly, the origin of the reduced light collection observed after the major Gd sulfate injection was identified. As discussed in Section 2.6.4, the decrease in light collection was caused by a few iron rusted bolts from the Gd-loaded water distributor located below the cryostat, which led to rust deposition on some of the NV's ePTFE reflective panels.

The cleaning and protection of the components of both veto systems, such as the NV ePTFE panels and the PMTs, are essential during disassembly and reassembly in order to preserve their remarkable reflectivity, purity, and consequently their light-collection performance. As an example, in order to allow access to the TPC and cryostat, the PMT columns were raised and positioned along two lateral sides of the cryostat upper hanging structure. The Neutron Veto status during a week of the reassembly period is shown in Figure 24.

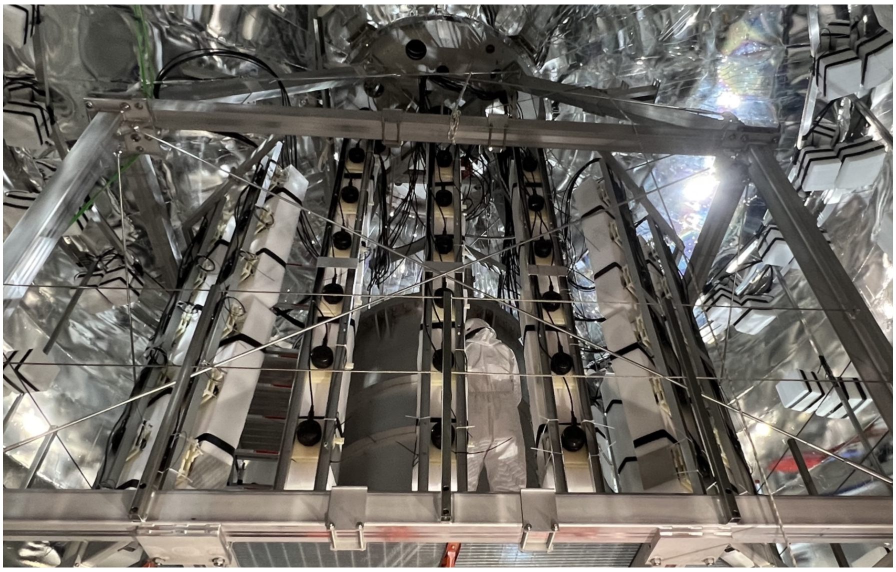

Figure 24: The Neutron Veto structure and its PMT columns situated in their final position. The ePTFE reflective panels are not present and the PMTs are protected with polystyrene foam blocks.

2.7 Future of xenon-based DM Direct Search

Recent advancements in liquid xenon detectors, such as XENONnT and LZ, have greatly improved sensitivities in the search for WIMP Dark Matter, yet the so-called "neutrino fog" still defines the ultimate boundary in the spin-independent parameter space. The gradient parameter, mentioned in Fig. 25, $n = -(\mathrm{d}\ln\sigma/\mathrm{d}\ln \mathrm{N})^{-1}$ quantifies how the discovery sensitivity degrades with increasing background. The region $n > 2$ marks the onset of the neutrino-limited regime. As previously mentioned, XENONnT already approached this limit in the light DM region, dominated by solar neutrinos.

Future detectors like the proposed 60-ton XLZD observatory [69] will not only need larger active masses but also optimized veto systems capable of detecting atmospheric neutrinos, since it would constitute a systematic limit to intermediate/high WIMP mass searches. Understanding the required veto dimensions will be crucial, as coincidences between signals in the active volume and the veto could help rejecting background events even within the neutrino fog. Beyond DM, XLZD also aims to explore rare processes such as neutrinoless double-beta decay of ^{136}Xe and solar neutrino measurement refinement.

However, such large-scale detectors present major technical challenges.

The enormous quantities of pure xenon required, the construction of cryogenic infrastructures at unprecedented scales, and the development of low radioactivity materials all pose significant hurdles. In addition, the use of traditional PMTs becomes increasingly problematic due to their size and intrinsic background, motivating the adoption of silicon photomultipliers (SiPMs) for improved radiopurity and compactness.

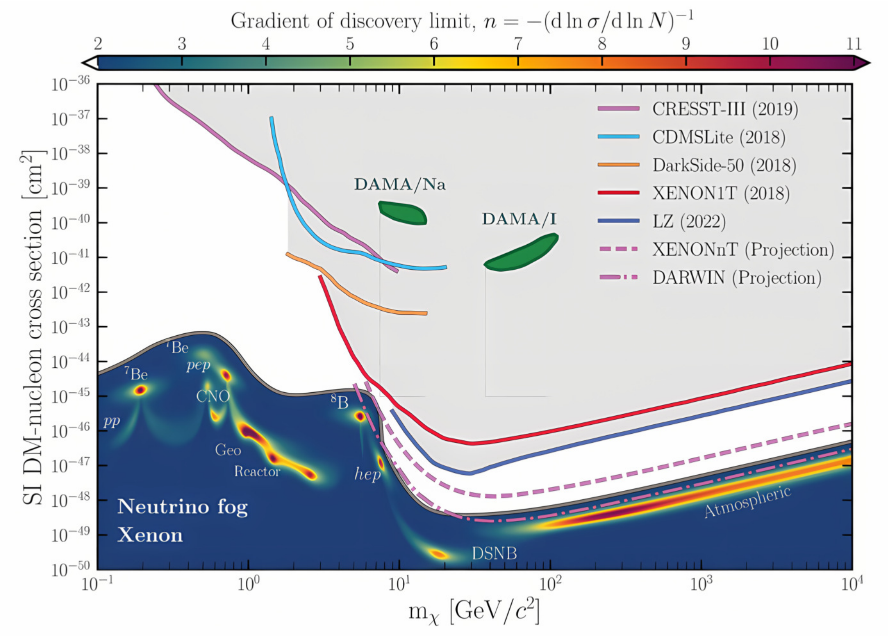

Figure 25: Exclusion limits on the SI DM-nucleon cross section for several experiments. The neutrino fog with its gradient parameter n is also displayed. Figure re-adapted from [70].

3 Study of supernova neutrinos with the XENONnT Vetoes

In Chapters 1 and 2, the crucial role of supernova neutrinos and their possible detection in Dark Matter experiments have been outlined. In this Chapter, we focus on their detection in the Gd-water vetoes of XENONnT. In particular, in Section 3.1.1, the supernova neutrino fluxes of the models introduced in Section 1.2.2, as expected at Earth after phenomena such as neutrino oscillations and matter effects have taken place, are presented. Section 3.1.2 highlights the dominant contributions of the neutrino cross section in pure water for the energy range between 0 and 50 MeV. Moreover, in Section 3.1.3 the convolution of the last two distributions is performed to obtain the expected number of neutrino-induced events in the water Cherenkov Vetoes of XENONnT.

Then, the simulation framework implemented for XENONnT is introduced in Section 3.2, which includes the MC GEANT4 toolkit and the two custom packages, *Neutron* and *Muon Veto Hitlet Simulators*. Finally, simulations of supernova neutrino-induced positrons and neutrons in both vetoes are detailed together with their results in Section 3.3.

3.1 Expected supernova neutrino events in the Vetoes

3.1.1 Supernova neutrino fluxes and oscillations

Recalling what was introduced in Section 1.2.2, the differential flux for each neutrino flavor ν_β at a time t_{pb} after the supernova core bounce and at a distance d, between the star and our detector, is parametrized as

$$\Phi_{\nu_\beta}(E, t_{\mathrm{pb}}) = \frac{L_{\nu_\beta}(t_{\mathrm{pb}})\ \varphi_{\nu_\beta}(E, t_{\mathrm{pb}})}{4\pi d^2\ \langle E_{\nu_\beta}(t_{\mathrm{pb}})\rangle}\,, \tag{20}$$

where $L_{\nu_\beta}(t_{\mathrm{pb}})$ is the neutrino luminosity, $\langle E_{\nu_\beta}(t_{\mathrm{pb}})\rangle$ the mean energy, both previously represented in Figs. 4, 5, 6 and 7.

$\varphi_{\nu_\beta}(E, t_{\mathrm{pb}})$ is the neutrino energy distribution, given at different times and energies for each neutrino flavor, and is commonly written in the α–fit form as

$$\varphi_{\nu_\beta}(E, t_{\mathrm{pb}}) = \xi_\beta(t_{\mathrm{pb}}) \left(\frac{E}{\langle E_{\nu_\beta}(t_{\mathrm{pb}})\rangle}\right)^{\alpha_\beta(t_{\mathrm{pb}})} \exp\left[-\frac{\left(\alpha_\beta(t_{\mathrm{pb}})+1\right)E}{\langle E_{\nu_\beta}(t_{\mathrm{pb}})\rangle}\right], \tag{21}$$

where $\alpha_\beta(t_{\text{pb}})$ is the so–called pinching parameter since it controls the high-energy tail of the distribution caused by thermal effects. The α_β parameter satisfies

$$\alpha_\beta(t_{\text{pb}}) = \frac{2\langle E_{\nu_\beta}(t_{\text{pb}})\rangle^2 - \langle E^2_{\nu_\beta}(t_{\text{pb}})\rangle}{\langle E^2_{\nu_\beta}(t_{\text{pb}})\rangle - \langle E_{\nu_\beta}(t_{\text{pb}})\rangle^2}, \tag{22}$$

while $\xi_\beta(t_{\text{pb}})$ is a normalization factor defined such that

$$\int \varphi_{\nu_\beta}(E, t_{\text{pb}})\, dE = 1. \tag{23}$$

Neutrino oscillations modify the introduced flux in Eq. 20, due to the effects already explained in Section 1.1.2. Furthermore, neutrinos and antineutrinos streaming through the outer layers of the stellar envelope, from the high-density region to the low-density one, feel ordinary matter effects as they cross two resonance layers. These two layers are called Mikheyev-Smirnov-Wolfenstein (MSW) resonance layers (L and H), and they are separated by a rather large region due to the relation between the two mass splittings (introduced in Section 1.1.2), $|\Delta m^2_{atm}| \gg \Delta m^2_{sol}$.

Figure 26 shows the level-crossing diagrams for the mass spectra in the normal and inverted orderings, in the right and left plots, respectively. The black curves represent the mass eigenvalues as a function of electron number density[9], while the black dotted lines correspond to the energies of the flavor levels ν_e and ν_x. Negative values of the electron number density refer to the antineutrino sector and n_e= 0 represents the vacuum. These diagrams allow us to determine in which mass eigenstate will emerge a neutrino produced in a given interaction eigenstate. Furthermore, note that H-resonance is satisfied by neutrinos in normal ordering (NO) whereas in inverse ordering (IO) is only satisfied by antineutrinos, making the neutrino burst dependent on the hierarchy.

---

[9] The SN matter potential is defined as $\lambda_r = \sqrt{2} G_F n_e$ where $n_e = n_{e^-} - n_{e^+}$, related to the net electron fraction and the matter density, refers to the electron number density and G_F is the Fermi constant of the weak interactions.

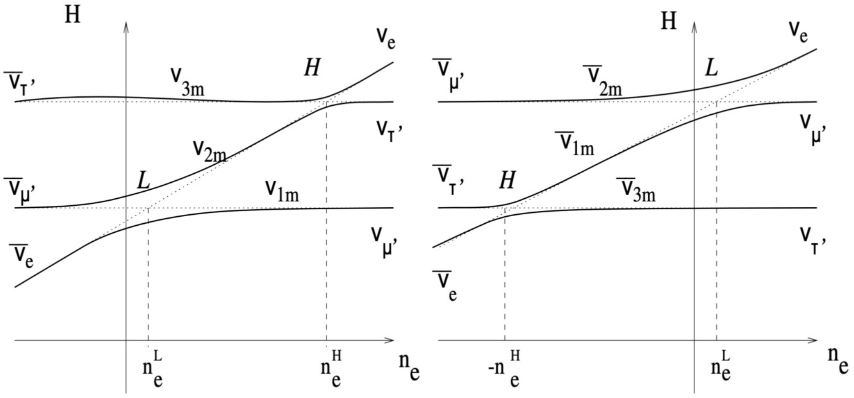

Figure 26: Three-flavor level crossing diagrams for neutrino propagation or mass eigenstates in terms of the electron number density. The left figure shows the normal ordering scenario whereas the right one displays the inverted ordering diagram. The H-resonance region is associated to Δm^2_{atm} whereas L-resonance is related to Δm^2_{sol} [20].

The flux modification due to this effect (neglecting Earth matter crossing) for normal ordering is

$$\Phi_{\nu_e} = P_H\, U_{e2}^2\, \Phi^0_{\nu_e} + (1 - P_H\, U_{e2}^2)\, \Phi^0_{\nu_x} \tag{24}$$
$$\Phi_{\bar{\nu}_e} = U_{e1}^2\, \Phi^0_{\bar{\nu}_e} + U_{e2}^2\, \Phi^0_{\bar{\nu}_x} \tag{25}$$

while for the inverted ordering one has

$$\Phi_{\nu_e} = U_{e2}^2\, \Phi^0_{\nu_e} + U_{e1}^2\, \Phi^0_{\nu_x} \tag{26}$$
$$\Phi_{\bar{\nu}_e} = P_H\, U_{e1}^2\, \Phi^0_{\bar{\nu}_e} + (1 - P_H\, U_{e1}^2)\, \Phi^0_{\bar{\nu}_x} \tag{27}$$

Here, P_H denotes the probability of a transition to an adjacent mass eigenstate when crossing the H-resonance layer, and Φ^0 is the non-oscillated flux. From the neutrino mixing matrix, introduced in Eq. 3, and from the currently best-fit values of the mixing angles [71], one obtains

$$U_{e1}^2 = \cos^2\theta_{13}\cos^2\theta_{12} \simeq \cos^2\theta_{12} \tag{28}$$
$$U_{e2}^2 = \cos^2\theta_{13}\sin^2\theta_{12} \simeq \sin^2\theta_{12}. \tag{29}$$

In standard SN simulations, the matter density profile decreases sufficiently slowly that neutrino evolution is adiabatic, meaning that each mass eigenstate follows the corresponding eigenvalue shown in Fig. 26. This behavior, however, breaks down at the shock front: the sharp discontinuity in density induces strong non-adiabatic transitions.

Given the currently measured value of θ_{13} of about 8° [71], the H-resonance is adiabatic under steady conditions, implying a flip probability $P_H = 0$. At the shock fronts, in contrast, this resonance becomes fully non-adiabatic, and the transition probability reaches $P_H = 1$. The L-resonance is crossed by the shock only at comparatively late times ($t_{\text{pb}} \gtrsim 10$ s), and it never becomes strongly non-adiabatic. Therefore, sub-leading effects associated with a nonzero P_L are generally neglected [17], [20], [22], [72].

Now, the flux integrated in the total SN emission time (or fluence), which is about 8 seconds in both cases, for a 27 $M_\odot$ and 11.2 $M_\odot$ SN progenitor masses at 10 kpc from the Earth, will be shown for different configurations. All these fluxes were computed using SNEWPY with the models from the same framework, in the LS220 EoS. These models were previously introduced in Section 1.2.2 in which their luminosities and mean neutrino energies were displayed. Firstly, the fluence for the two progenitor masses will be compared for all neutrino flavors.

Note that in the study of supernova neutrinos, muon and tau neutrino flavors are indistinguishable due to the lack of a significant difference in their interactions at this energy range, which take place through NC interactions. Correspondingly, their spectra and flux, indicated as ν_x and $\bar{\nu}_x$, are always shown together due to their similarity.

As shown in Fig. 27, the fluxes differ significantly across progenitor masses. This trend can be attributed to the distinct luminosities characterizing the post-bounce accretion phase (see Fig. 4-center). Moreover, following the peak luminosity in the neutronization burst, shown in Fig. 4-left, in both cases, the dominant non-oscillated flux comes from electron neutrinos.

Then, as shown in Fig. 28, time-integrated fluxes of non-oscillated neutrinos from all flavors are compared with the fluence considering normal ordering oscillations induced by adiabatic MSW resonance effects inside the stellar envelope in the upper figure. We have considered adiabatic conditions for simplicity, in order to perform a first estimate of the difference in the number of expected events in our detectors. In the lower one, the same comparison is performed but with inverted ordering oscillations induced by the same effects.

Focusing on the $\bar{\nu}_e$, which will be the focus on the following sections due to their predominant interactions in water at the considered energies, we can see that the difference between the flux with and without oscillations is not as significant as in the case of the neutrino of the same flavor. Moreover, for the inverted ordering, if we return to Eq. 27 and assume adiabatic conditions ($P_H = 0$), the resulting flux becomes identical to that of the x-flavor (muon and tau) neutrinos and antineutrinos, consistent with what is observed in the lower panel of Fig. 28. Furthermore, the same phenomenon occurs in normal ordering oscillations of the electron neutrino, which is approximately equal to the non-oscillated x-flavor flux, as shown in the upper panel.

The total time- and energy-integrated flux for the electron antineutrino is about $2.044 \cdot 10^{15} \mathrm{m}^{-2}$ without considering oscillations. With neutrino oscillations, it becomes $2.006 \cdot 10^{15} \mathrm{m}^{-2}$ in the NO case and $1.926 \cdot 10^{15} \mathrm{m}^{-2}$ in IO, which would imply that the expected number of events in the XENONnT Veto could be significantly lower if the mass eigenstates follow an inverted hierarchy.

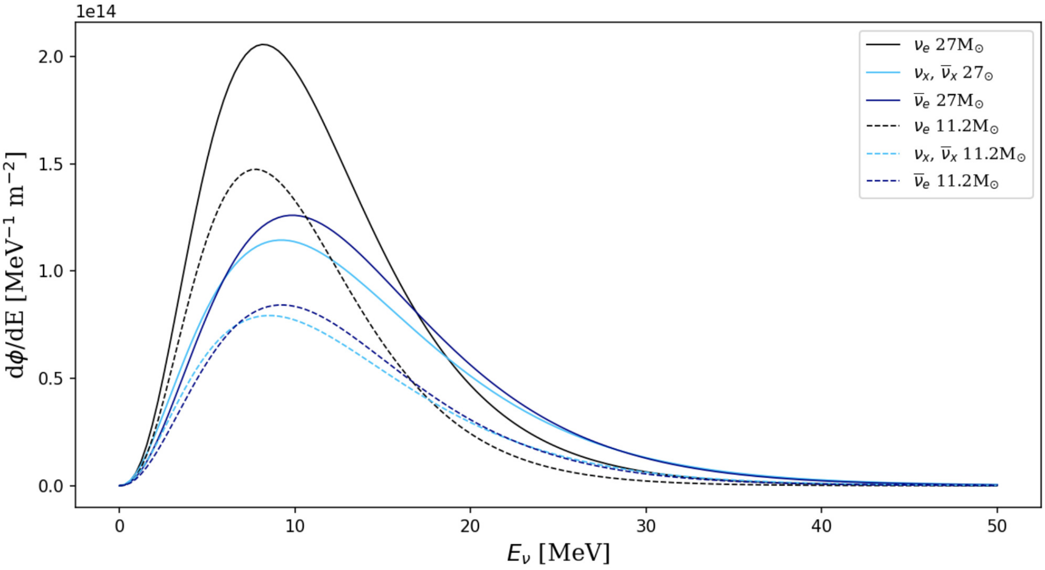

Figure 27: Total supernova emission time-integrated fluxes of non-oscillated $\nu_e, \bar{\nu}_e, \nu_x$ and $\bar{\nu}_x$ with $x = \mu, \tau$ for 27 $M_\odot$ and 11.2 $M_\odot$ SN progenitor stars at 10 kpc in LS220 EoS.

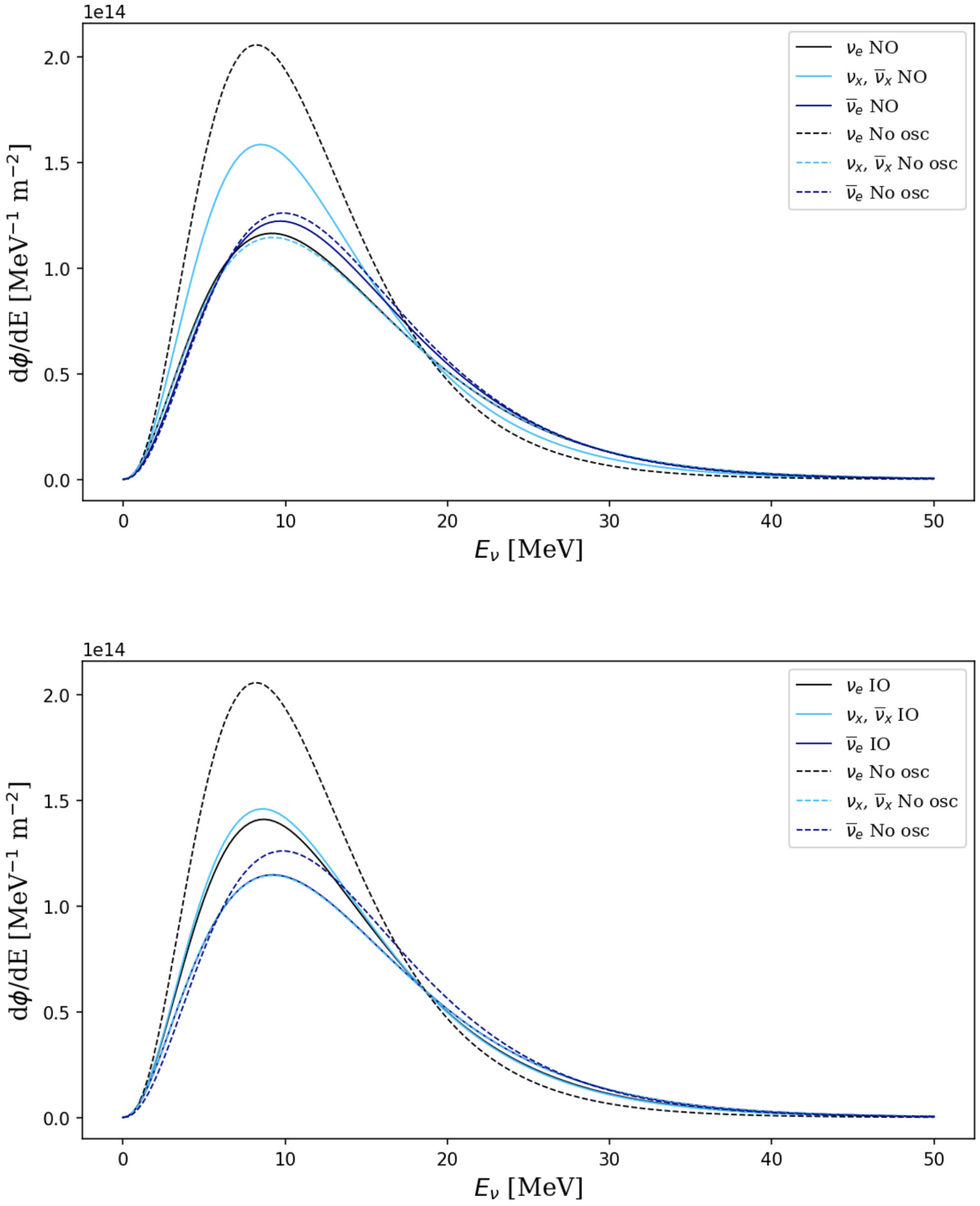

Figure 28: (Upper) Comparison between time-integrated fluxes of non- (dashed) and adiabatic normal ordering oscillated (solid) ν_e, $\bar{\nu}_e$, ν_x and $\bar{\nu}_x$ with $x = \mu, \tau$ for a 27 $M_\odot$ SN progenitor star at 10 kpc in LS220 EoS. (Lower) Comparison between time-integrated fluxes of non- (dashed) and adiabatic inverted ordering oscillated (solid) ν_e, $\bar{\nu}_e$, ν_x and $\bar{\nu}_x$ with $x = \mu, \tau$ for a 27 $M_\odot$ SN progenitor star at 10 kpc in LS220 EoS.

3.1.2 Supernova neutrino interactions in water

Thanks to the dimensions and low background rates reached in the XENONnT detector, it may able to detect also all flavor neutrinos coming from supernova explosions through their coherent elastic scatters on Xe nuclei in the TPC [72]. But this is not the only channel through which XENONnT can detect SN neutrinos.

Supernova neutrino detection in XENONnT occurs mainly through two channels:

- **Coherent Elastic Neutrino-Nucleus Scattering:** Neutrinos scatter off Xe nuclei producing nuclear recoil signals. This method is insensitive to neutrino flavor, allowing for the detection of all neutrino types.
- **Inverse beta decay:** The reaction from Eq. 1 is exploited, where both positron detection and neutron capture allow for a clear $\bar{\nu}_e$ identification, especially in water-based detectors with high proton content. This process, with the subsequent emission of Cherenkov light by the positron and the delayed neutron capture in water, is shown in Fig. 29. The typical time delay between the positron prompt signal and the neutron capture in water is $\simeq 200\ \mu\text{s}$.

In this work, we focus on the detection of IBD interactions in the water Cherenkov Muon and Neutron vetoes, since it is the dominant detection channel for supernova $\bar{\nu}_e$ in water Cherenkov detectors and scintillators. Although the IBD cross section is relatively small compared to charged current interactions on nuclei (as will be discussed in Section 4.1.2), it is by far the largest among the interactions relevant in the supernova neutrino energy regime (below ~ 100 MeV).

Other processes occurring in this energy range include CEνNS and elastic scattering on electrons, introduced in Section 1.1.3. However, being neutral–current interactions, their cross sections are significantly lower, and they often lead to partially or fully undetectable signals in water. For instance, CEνNS produces nuclear recoils with energies well below the Cherenkov threshold, and elastic $\nu - e^-$ scattering yields recoil electrons whose energies may fall below or only slightly above threshold, limiting their detectability. At energies of about 100 MeV, CC interactions with oxygen also contribute, but as already observed in the flux at these energies of typical SN spectra (Fig. 27), this contribution remains negligible.

The detection of neutrinos could help to determine the position of the SN in the visible Universe. The most promising method for neutrino pointing is via elastic scattering, in which the electron gets kicked in the direction of the neutrino. In a Cherenkov detector such as Super-Kamiokande, the directionality of the electron can be determined from the Cherenkov ring. In the XENONnT Veto, the Cherenkov angle is not measured which makes the IBD the only relevant detected interaction [17], [22].

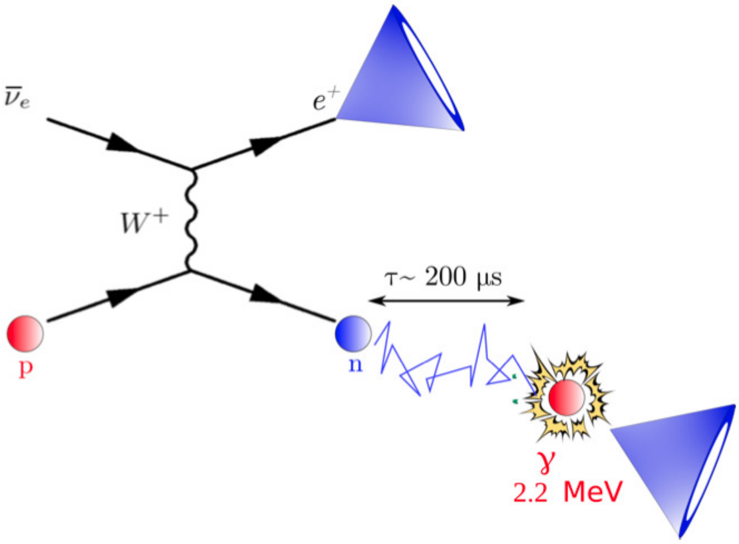

Figure 29: Schematic illustration of an IBD process and the subsequent positron emission of Cherenkov light with the delayed neutron capture on another proton. The characteristic neutron capture time in water is $\tau \simeq 200$ μs [18].

The inverse beta decay cross section, obtained from *sntools* [73], which is a Montecarlo event generator for supernova neutrino interactions, is shown in Fig. 30. The cross section from sntools is based on the calculation from [74]. Moreover, in this framework, the differential cross section in given is terms of the positron recoil energy apart from the neutrino energy, so it has been integrated in the full positron recoil energy range to obtain the plot shown just below, in units of [m^2].

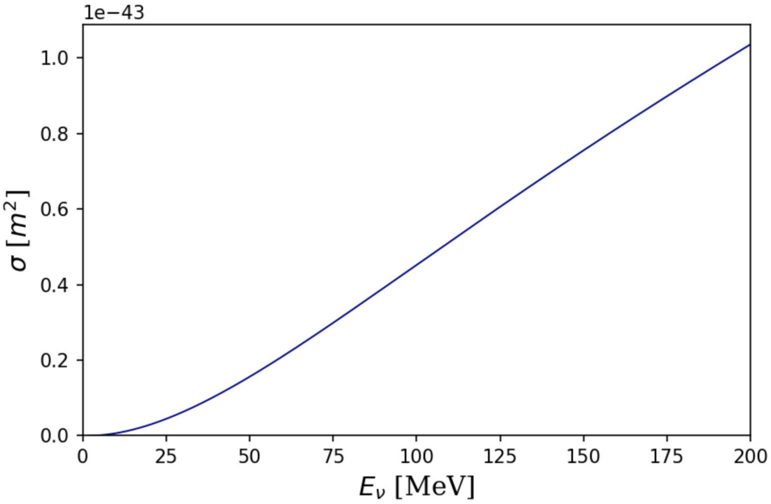

Figure 30: Inverse β-decay cross section shown in the supernova neutrino energy range with a value of the order of 10^{-44} m^2 at about 50 MeV. The IBD threshold is present at 1.806 MeV.

3.1.3 Expected positron event spectrum in the Vetoes

The differential energy spectrum of expected neutrinos interacting via IBD, for each energy bin, and considering that they arrive homogeneously to the water tank, is defined by:

$$\frac{dN_i^\nu}{dE_i} = N_{H_2O} f_p \frac{d\Phi_i^{\bar{\nu}_e}(E_i)}{dE_i} \sigma_i(E_i) \tag{30}$$

where N_{H_2O} is the number of water molecules targets in the number of tonnes considered, f_p is the fraction of H or free protons in water ($f_p = 2$), Φ_i is the flux in the energy bin i, already time integrated in units of MeV^{-1}m^{-2}, and σ_i is the cross section in the energy bin i, already integrated in the final positron energy, in units of m^2.

As already mentioned in the previous section, the products of the IBD interaction are a positron and a neutron. The positron carries away most of the antineutrino energy, leading to a continuous positron spectrum with

$$E_{e^+} \simeq E_{\bar{\nu}_e} - 1.806\ \text{MeV} \tag{31}$$

where 1.806 MeV is the kinematic threshold of the reaction, given by $m_e + (m_n - m_p)$. Because of the large mass difference between the neutron and the positron, only a tiny fraction of the antineutrino energy goes into neutron recoil, which is typically of the order of ~ 1 keV. Thus, to a good approximation, the positron spectrum can be computed by neglecting the neutron kinetic energy, in particular at small neutrino energies.

Expected interaction spectrum in the water tank

The neutrino spectrum and the corresponding positron spectrum in the entire water tank (Fig. 32) were calculated by considering the number of water molecules in 700 tons, multiplied by two to account for the number of free protons per molecule. The convolution was then performed between the electron antineutrino flux from a 27 $M_\odot$ progenitor at 10 kpc, using the LS220 equation of state and neglecting oscillations (Fig. 27), and the cross section shown in Figure 30. This convolution is illustrated in Fig. 31 which shows how the antineutrino spectrum in the water tank is shifted toward higher energies due to the combined effect of the flux peak and the rising cross section.

The energy-integrated number of events expected in the whole XENONnT veto is about 170 events.

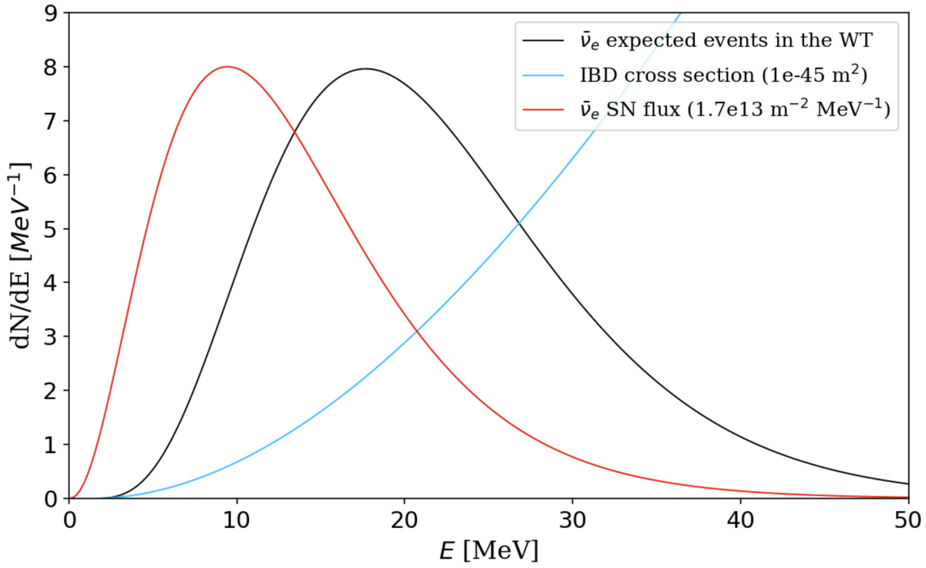

Figure 31: Convolution of the $\bar{\nu}_e$ non-oscillated time-integrated flux (red) from the SN progenitor of 27 $M_\odot$ in LS220 EoS at 10 kpc with the IBD cross section (light blue) to produce the neutrino rate in the water tank (black). The flux and cross section have been scaled for visualization purposes.

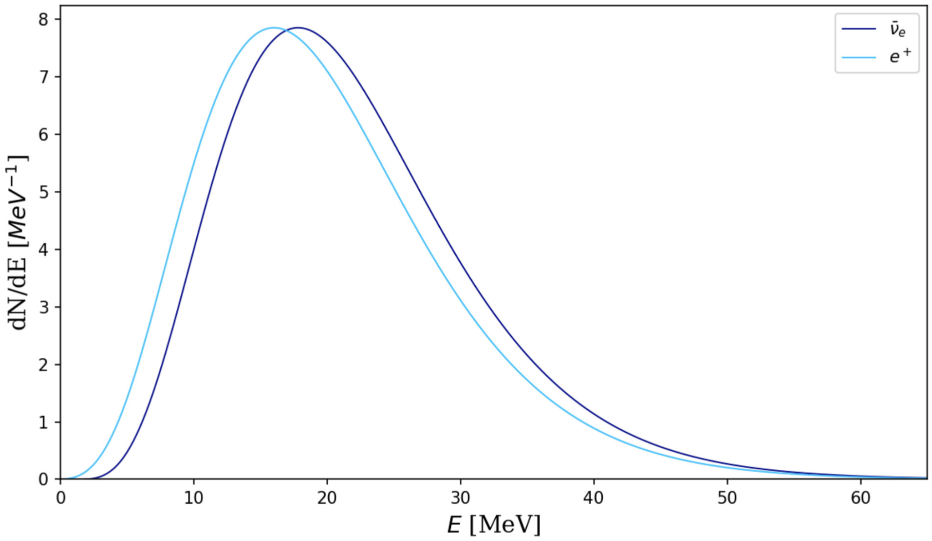

Figure 32: Differential $\bar{\nu}_e$ IBD interaction spectrum (dark blue) with its associated differential positron spectrum (light blue). The flux considered is the non-oscillated one from the SN progenitor of 27 $M_\odot$ in LS220 EoS at 10 kpc.

Expected SN neutrino events: WT, MV and NV

Tables 1 and 2 examine the different values of the expected number of events, computed using Eq. 30 but replacing the number of targets with those in the NV (34 tonnes) and in the MV (700-34 tonnes), and then applying the corresponding neutrino fluxes. Note that the NV contains approximately 5% of the water volume of the MV, which is consistent with the expected number of events obtained for all models. For instance, in Table 1 we observe that the expected number of events roughly doubles when the progenitor mass is approximately twice as large.

We also note that for the SFHo EoS model, whose peak luminosity is slightly higher and whose neutrinosphere temperature exceeds that of LS220 at certain times, the expected number of events is correspondingly slightly larger in all three active regions.

Model	NV	MV	NV + MV
LS220, 11.2 $M_\odot$	4.3	84.2	88.6
LS220, 27 $M_\odot$	8.3	161.6	169.8
SFHo, 27 $M_\odot$	8.6	167.5	176.0

Table 1: Expected IBD interactions for different progenitor models at 10 kpc, in the whole water Cherenkov Veto and its two subsystems, the NV and the MV. The first two rows compare results obtained from two different progenitor masses while the second and third rows contrast two progenitors that differ in their EoS.

Model	NV	MV	NV + MV
LS220, 27 $M_\odot$	8.3	161.6	169.8
LS220, 27 $M_\odot$, NO osc	8.1	159.5	167.6
LS220, 27 $M_\odot$, IO osc	7.9	155.1	163.0

Table 2: Expected IBD interactions for the same progenitor model at 10 kpc, in the whole water Cherenkov Veto and its two subsystems, the NV and the MV. The comparison among three flux predictions with different oscillation effects is shown. When NO and IO oscillations are mentioned, we refer to adiabatic conditions.

Regarding the difference between neglecting oscillations and including NO or IO matter effects, shown in Table 2, we find that the discrepancy in the expected event counts does not exceed about seven events in the entire WT. This arises from the similarity of the temperatures (or, equivalently, typical energies; see Fig. 5) associated with $\bar{\nu}_e$ and ν_x, $\bar{\nu}_x$, whose fluxes are closely related under adiabatic conditions, as discussed in Eqs. 25 and 27.

The expected number of SN IBD interactions in water carries a systematic uncertainty of 20–30%, which is derived from the only observation of a core-collapse supernova neutrino flux: the SN1987A neutrino signal [75].

It should be noted, however, that these spectra are still an approximation: as the antineutrino energy increases, the neutron recoil energy becomes larger, reducing the fraction of energy carried by the positron. This phenomenon is shown in Fig. 33 where the difference between the antineutrino energy and the positron energy is plotted in terms of the energy of the former. This plot has been obtained from GENIE [76] simulations of SN antineutrino interactions in water between 10 and 70 MeV (note that GENIE only supports energies starting from 10 MeV). The SN model used was from the SN progenitor of $27M_\odot$ at 10 kpc with LS220 EoS and without considering oscillations. The cross section used for this calculation was obtained from the default interaction model defined in GENIE (RFG-LS from v3.06.00 [77] which employs a Relativistic Fermi gas nuclear model and Llewellyn–Smith model for CCQES). As we can see, the mean value of the difference between the antineutrino and positron energy ΔE over the entire range is 2.4 ± 0.6 MeV, which is compatible with the kinematic threshold of the process. However, if higher neutrino energies were considered, the neutron recoil would become large enough to invalidate the approximation used here.

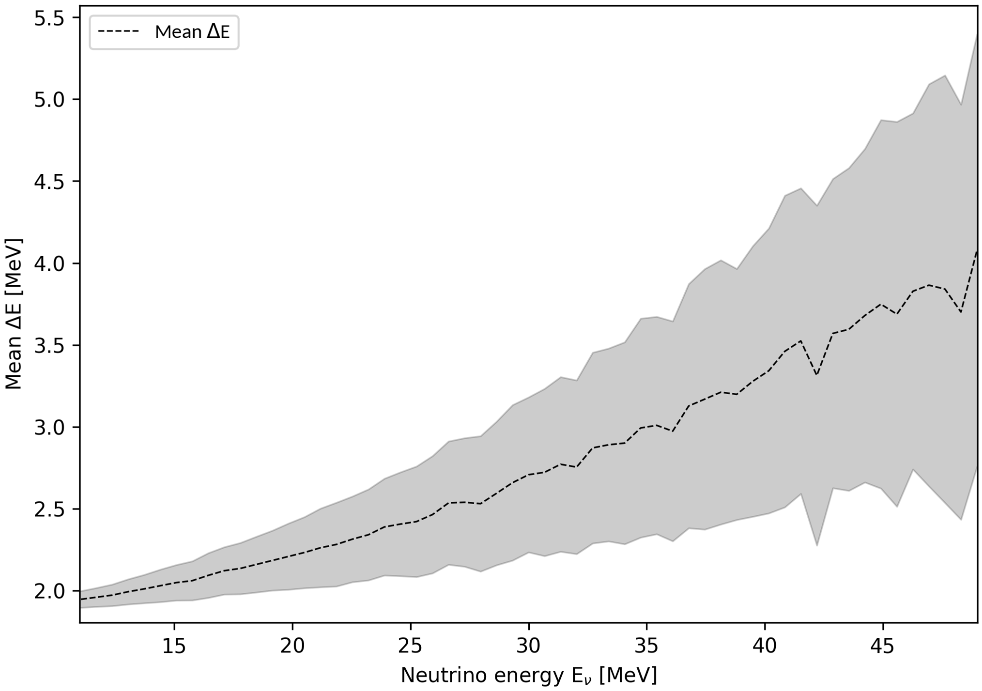

Figure 33: Bin averaged-energy difference between the emitted positron and the incoming antineutrino, for the IBD process, in terms of the incoming neutrino energy bin center. The grey band represents the standard deviation in each energy bin. The mean value in the whole range is 2.4 ± 0.6 MeV; at low energy, it is compatible with the 1.806 MeV energy threshold.

3.2 Montecarlo simulations in the XENONnT Water Cherenkov Vetoes

3.2.1 Simulation framework of XENONnT: GEANT4

The XENONnT simulations are based on the GEANT4 [78] toolkit, with the Montecarlo (MC) framework built upon the simulation package originally developed for XENON1T. GEANT4 is an open-source toolkit developed at CERN for simulating the transport and interactions of particles in matter, used in several nuclear and subnuclear fields such as high-energy physics, medical physics, space sciences, and radiation protection. Particle transport is tracked step by step, considering interactions such as energy loss, scattering, or interactions with electromagnetic fields. This transport ends when the particle loses all its kinetic energy, disappears as a consequence of an interaction, or reaches the boundaries of the simulation. The signals observed by the XENONnT detectors, consequence of photons hitting the PMTs' photocathode, are then simulated with custom-developed waveform or hitlet simulators (see Section 3.2.2) to reproduce the same raw data format as recorded with real data.

For particle generation and propagation, GEANT4 version 10.06-patch02 is employed in the XENONnT simulations, whose general idea is to connect all subdetectors in a unique framework to produce complete and consistent simulations of the entire experiment.

The Neutron Veto is modeled in GEANT4 consisting in various ePTFE reflective panels and PMTs mainly designed to detect Cherenkov photons produced by neutron captures in water. The Muon Veto was modeled, as already mentioned, for XENON1T in an analogous way to the Neutron Veto. The NV and MV model and the core cryostat surrounding the TPC, as implemented in GEANT4 is shown in Fig. 34. The optical properties of both vetoes have been extensively characterized, considering the Cherenkov photon absorption, reflection and transmission within the systems.

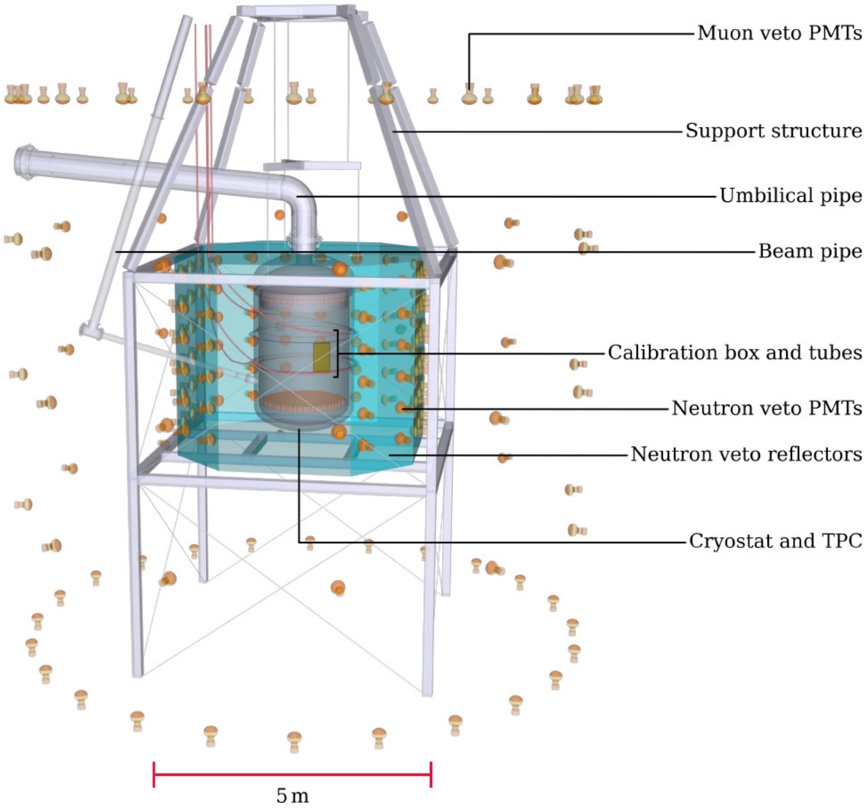

Figure 34: GEANT4 rendering of the whole XENONnT detector setup, including the Muon Veto and Neutron Veto systems. The water tank walls, responsible for housing the MV PMTs, the Neutron Veto support structure, and other components, are not shown in this picture for clarity. The NV ePTFE reflective panels, isolating NV from the MV region, are shown as translucent blue surfaces. The detection area of the NV PMT windows is positioned in their dedicated panel openings.

The NV and MV PMT geometry, including its body and head, is accurately incorporated in GEANT4, whereas simpler methods are performed to model the internal parts to avoid performance degradation. The NV and MV PMTs geometry is equal and shown in Fig. 35-right. Currently, the PMT photocathode (represented in red in Fig. 35-right) is modeled as a fully opaque surface that absorbs and records hitting photons. However, its complete reflectivity is under consideration pending dedicated measurements on the specific PMT model.

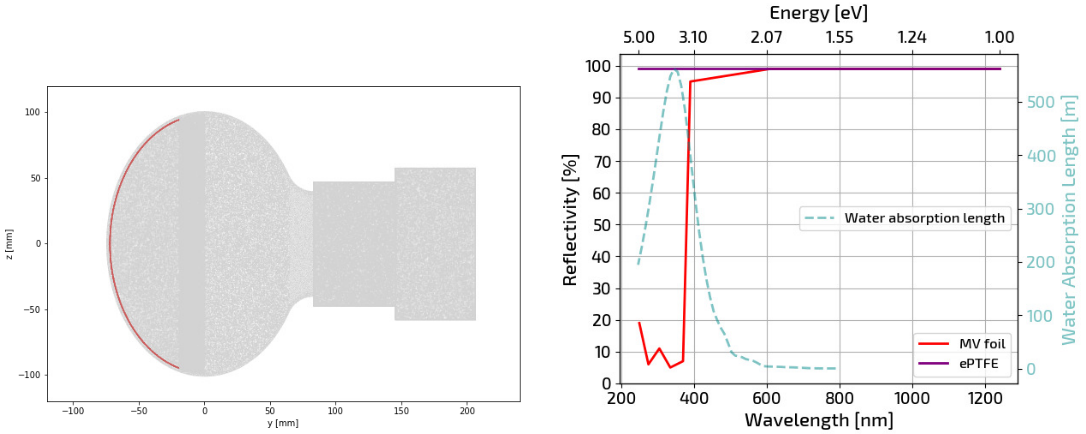

Figure 35: (Left) NV PMT rendering, as reproduced in GEANT4. The red line represents the PMT photocathode. (Right) MV and NV water absorption length (blue right axis) model displayed along with the reflectivity of reflective foil present in the water tank walls (red) and the one from the ePTFE panels forming the NV.

As mentioned, the optical properties of the vetoes are critical factors that must be correctly reproduced in GEANT4. One of these properties is the water absorption length (shown in Fig. 35), which is modeled employing parameters from Super-Kamiokande calibrations, including data on refractive index, absorption length, and Rayleigh scattering length across the energy range [1.57, 5.03] eV. The ePTFE panels that enclose the NV volume presents a reflectivity of 99.35%. The cryostat is also clad with the same ePTFE reflector. This high reflectivity is critical to ensure that most photons are reflected inside the system until they eventually reach the PMTs, enhancing the detection efficiency.

The walls of the water tank are clad with the highly reflective DF2000MA foil with a specular reflectance close to 100% for wavelengths larger than 400 nm, while $\sim$ 90% of the incoming light below 370 nm is absorbed by the foil. This dependence of the MV foils on the photon wavelength is shown in Fig. 35-right.

3.2.2 Neutron Veto and Muon Veto Hitlet Simulators: PMT response to photon detection

NV Hitlet Simulator

A custom package, the *NV Hitlet Simulator* (HitSim), is used to simulate the response of the PMTs to incident Cherenkov photons, complementing the GEANT4-based NV simulations. Its purpose is to generate low-level signal information identical to that of real data, thus allowing the same data processing chain to be applied to both experimental and simulated Neutron Veto data. In fact, it is designed as a fast tool to build NV hitlets (introduced in Section 2.6.6) and events, assuming ideal delta-shaped PMT signals, since the full waveform time evolution is not considered in the analysis process of this detector.

For each Cherenkov photon reaching a NV PMT, information such as the impact time on the photocathode, the PMT channel and the photon's wavelength, is stored in the GEANT4 Root TTree format output. This file is later processed by the HitSim. As introduced in Section 2.6.6, the processing of raw data waveforms is performed by strax and straxen. In the simulation workflow, the first step is to convert impinging photons into detected photons with a properly simulated charge signal amplitude in order to finally convert PMT hits into straxen events.

Photon detection occurs when a photon generates a photoelectron (PE) at the PMT photocathode with a probability dependent on the wavelength and the PMT quantum efficiency (QE). Once the PE is generated, it must arrive to the first dynode of the amplification stage. The corresponding probability is absorbed into the PMT collection efficiency (CE).

The HitSim uses three inputs to model the full detection probability and to convert each photon hit into an area in units of photoelectrons (PE), following:

$$p_{det}(\lambda) = \mathrm{Binom}(n = 1, p = QE_i(\lambda) \cdot \mathrm{SPE}_{Acc} \cdot eCE) \tag{32}$$

This probability determines whether a photon hit survives and, if so, how its charge is sampled.

We can see an additional parameter, SPE_{Acc}, the Single PE Acceptance, which, together with the other two, will be described in the following paragraphs.

Quantum Efficiency

The wavelength-dependent QE_i is the quantum efficiency for each PMT provided by Hamamatsu. Fig. 36 shows the impact of applying QE on the Cherenkov photon spectrum, also including the absorption length model of water used in the simulation.

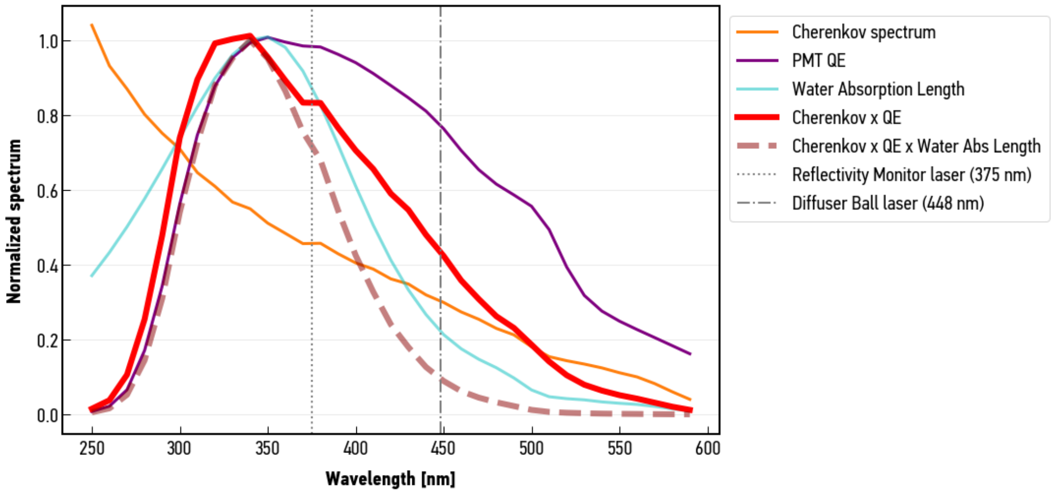

Figure 36: QE curve of one PMT overlapped and convoluted to the energy spectrum of the Cherenkov photon hit from GEANT4 output. The model of water absorption length is also considered and convoluted with the two previous ones. The dotted and dashed-dotted thin lines are the wavelengths of the Reflectivity Monitor and Diffuser Ball lasers' calibrations.

The wavelengths to which the NV is most responsive fall within approximately [300, 400] nm, with about 75% of the Cherenkov spectrum contained within the [290, 440] nm range. Even if the QE reaches its maximum around 350 nm, the number of emitted Cherenkov photons per unit wavelength is inversely proportional to the wavelength squared, which shifts its maximum sensitivity slightly below 350 nm.

Effective Collection Efficiency

The effective Collection Efficiency or eCE, accounts for the probability that a generated PE reaches the first dynode and is successfully amplified. Although each PMT should have its own CE, HitSim uses a single effective value per science run. This eCE is tuned through a Monte Carlo–Data matching procedure using AmBe calibration data. It encapsulates all potential uncertainties and discrepancies between the real detector optical performances and the simulation. The eCE determined for SR1 (with pure water condition, no Gd-doping) and adopted in this work is [79] $eCE = 87\%$.

SPE PDF and Acceptance

The factor SPE_{Acc} accounts for the probability that a low-amplitude signal surpasses the NV DAQ hardware threshold (typically 15 ADC counts). This acceptance depends on the SPE model, which incorporates:

- fully-amplified photoelectrons,
- sub-amplified PEs (due to incomplete first-dynode multiplication, inefficient electron collection, or photons reaching the first dynode directly),
- pedestal contributions (charge present in PMTs without light arriving to them),
- double-photoelectron (DPE) emission, which accounts for cases in which two photoelectrons are created when one photon arrives to the photocathode.

The SPE model used in HitSim consists of two components: one describing the under-amplified photoelectrons through a smoothed box function, and another representing fully amplified photoelectrons using a Poissonian-Gaussian distribution. However, due to the DAQ hardware threshold, a significant fraction of under-amplified electrons is not recorded, which leads to inaccuracies when relying solely on the raw SPE model.

To address this issue, HitSim employs a hybrid charge-sampling approach that combines real data distributions with theoretical fit functions, thereby compensating for the impact of the ADC threshold on the charge spectrum. The resulting charge-sampling PDF merges measured data with theoretical predictions, as illustrated in Fig. 37.

The SPE acceptance is computed as the fraction of the SPE PDF lying above the DAQ amplitude threshold.

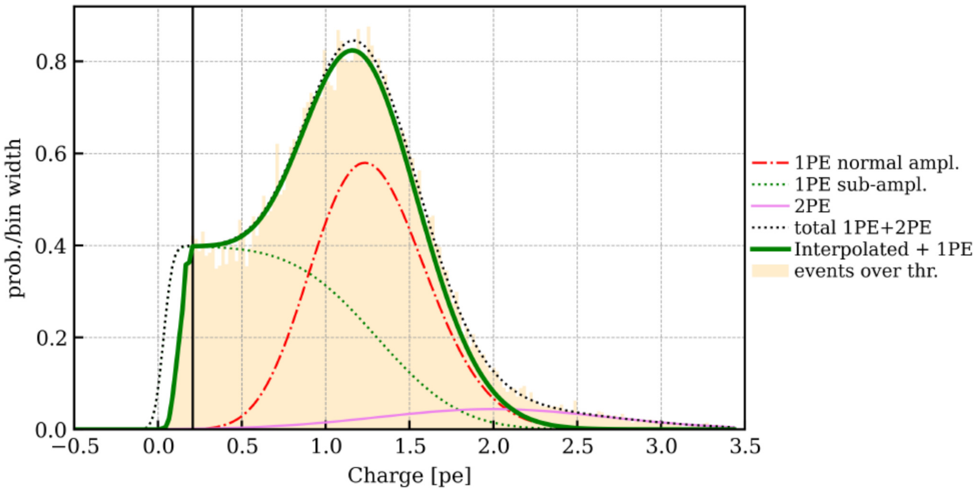

Figure 37: Charge distribution of a NV PMT obtained with LED calibrations. The final SPE model used by the HitSim (solid green line) is a combination of the data with the 15 ADC count amplitude threshold applied (orange distribution) and of the SPE fit function (dashed thin black line). Up to the first intersection point (marked with the solid vertical line), the distribution follows the data, then it continues with the fit function, excluding the DPE (or 2PE) component. .

From the SPE$_{Acc}$, QE, and eCE the detected photons are obtained thanks to Eq. 32, then, HitSim samples the charge associated with each detected hit using the SPE model. Finally, once charge sampling is performed, the resulting pseudo-hitlets are converted into hitlets and eventually into events via the corresponding straxen plugin. These resulting events are compared with real experimental data to assess the accuracy of the simulation.

MV Hitlet Simulator

The preliminary *MV Hitlet Simulator*, similarly to that of the NV, has a detection probability defined as

$$p_{det}(\lambda) = \mathrm{Binom}(n = 1, p = QE_i(\lambda) \cdot eCE) \tag{33}$$

where QE_i is also the wavelength-dependent quantum efficiency of the i-th PMT, reported in Hamamatsu datasheets and eCE the effective collection efficiency obtained from Montecarlo-muon data match accounting for both CE effects (collection of the created photoelectron at the first dynode) and

possible mismodeling of the MV optical properties in GEANT4. The value obtained from the mentioned MC-data match was eCE =1.31 [80].
In this simplified version, the Single PE response is modeled by a Gaussian distribution with a mean area of 1 PE and a standard deviation of 0.5 PE. Even if this model neglects the detailed shape of the real SPE spectrum, it still considers the PMT gain fluctuations due to the multiplication process in the dynode chain.

Another consideration in order to account for all the conditions present in the Muon Veto data acquisition system, is its trigger. As already mentioned in Section 2.6.6, the MV DAQ trigger register possible physical signals when 5 PMTs detect at least 1 PE (~100 ADC) within a 300 ns time window. As a consequence, MV HitSim registers the event whenever these conditions are satisfied.

Even if this MV HitSim is a preliminary version and must be further developed, it shows an actually good agreement between muon MC data and real muon data [80], so this tool has been used to convert hits in MV PMTs into PE area in our study.

3.3 Supernova positron and neutron simulations in the XENONnT Vetoes

Considering the model implemented for XENONnT in GEANT4, we have isotropically generated 10^4 neutrons and $2 \cdot 10^4$ positrons separately, through these Monte Carlo simulations in the whole water tank. The positron spectrum is the one obtained from the neutrino flux without considering oscillations of a $27 M_\odot$ at 10 kpc and in LS220 EoS supernova model (see Figure 32).
On the other hand, neutrons have been generated with a fixed energy of 1 keV, consistent with their expected recoil at low neutrino energies.

The visible energy caused by the positron, which carries away most of the kinetic energy of the neutrino, is detected via its Cherenkov radiation until its annihilation with an orbital electron, emitting two photons with total energy 1.022 MeV, takes place. Neutrons are subsequently moderated and captured by protons (E_γ = 2.2 MeV), with an average capture time of ~200 μs. This delayed time and spatial coincidence forms a clear IBD signature, characterized by the prompt positron annihilation followed by a delayed gamma signal, which allows background discrimination. However, in our case, we have simulated the two products separately to study their detection efficiency. A deeper study on this SN neutrino interaction by estimating the coincidence tagging efficiency of these two particles could be done in the future.

Note that to emit Cherenkov radiation, a charged particle's speed must exceed the phase velocity of light in water, which is c/n, where n $\approx$ 1.33 is the refractive index of water and c is the speed of light in vacuum. This sets a theoretical threshold for the lowest-speed particles that can be detected, β_{th} = 1/n $\approx$ 0.75, or a Lorentz factor γ_{th} $\approx$ 1.51. For electrons/positrons, muons, pions, and protons, this corresponds to total energies of 0.77, 159.55, 210.75, and 1416.79 MeV, respectively. In practice, to be detectable, the total energies must be somewhat higher. In our case, the positron spectrum peak is at about 20 MeV, which is far above the Cherenkov threshold.
The Cherenkov angle, is defined as cos θ_C = 1/nβ. For ultra-relativistic particles, θ_C = 42^o is constant, while this angle diminishes as the particle becomes slower. In our setup, the Cherenkov angle is not relevant due to the design of our vetoes, which present very high reflectivity, diffusing particle's trajectory, quite low PMT coverage, and small dimensions in the case of the NV.

After obtaining the Root TTree output file of GEANT4, which contains the photon hits registered in both the MV and NV PMTs, this file is processed by the corresponding MV and NV Hitlet Simulators. Each simulator selects its own PMTs based on the PMT hit ID variable (IDs 1000–1083 correspond to MV PMTs, while 2000–2119 correspond to NV PMTs). The full simulation chain specific to each detector is then applied, ultimately producing an output file containing the generated events with areas expressed in units of photoelectrons. Note that in the case of NV events, the NV selection cut is applied afterwards, for which the events must have an area larger than 5 PE.

3.3.1 Event area for SN neutrino-induced positrons and neutrons

The primary positron event position, given by its x, y, and z coordinates inside the water tank, is stored in the GEANT4 TTree output. By exploiting this information together with the event ID, common to both the GEANT4 and HitSim outputs, we can identify and select detected events originating either in the MV or in the NV, as illustrated in Fig. 38.

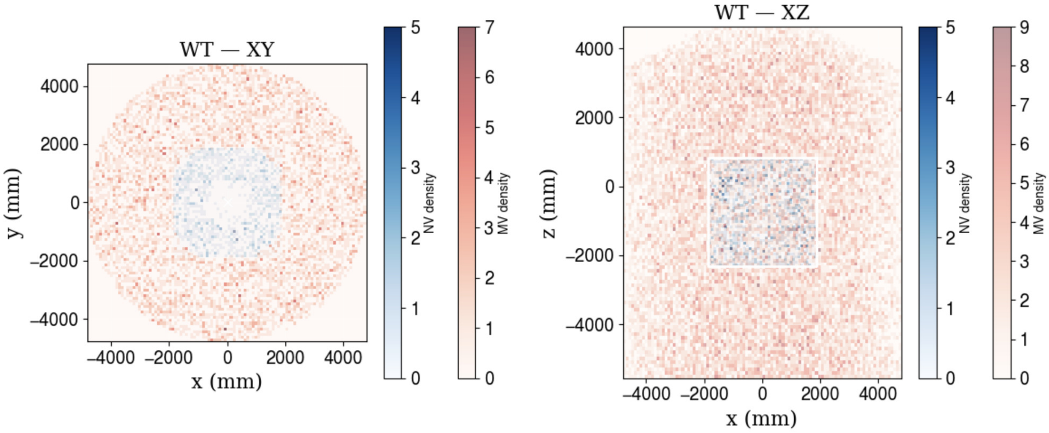

Figure 38: Positron event position inside the water tank (WT): the left picture shows a XY plane of the WT in which the two sections above and below the NV have been removed for illustration purpose. The right picture displays the whole WT in the XZ plane, where the MV generated events are clearly represented in red surrounding the NV (blue).

Once the MV and NV generated positron events have been selected, the event area registered by the two detectors, differentiating the position of generation of the event, is shown in Fig. 39 for the NV PMTs and in Fig. 40 for the MV PMTs. The same procedure has been performed with simulated neutrons; however, the Muon Veto is not expected to see the light emitted by neutron capture in water with significant efficiency ($< 1\%$), so only neutron events detected by the NV PMTs will be shown (see Fig. 41).

In both figures, we observe a region at a low event area corresponding to events originating in the other detector. This is expected, since an event occurring inside one detector produces most of its Cherenkov light within that same volume. In addition, the events with very small areas, around 5 PE or so, detected in the other detector are likely due to photons that travel through the few and small openings present in the NV roof. In fact, the NV detects about 3% of the positron events generated in the MV (pink). Of these, less that 0.5% are observed exclusively by the NV. Therefore, their contribution is negligible. In contrast, the MV detects about 2% of the positron events generated in the NV (blue), but none of them are seen exclusively by the MV.

Another fact to address is the higher amount of photoelectrons detected by the NV thanks to its smaller volume, higher PMT coverage (120 PMTs compared to 84 MV PMTs, in a 5% of water volume), and higher wall reflectivity.

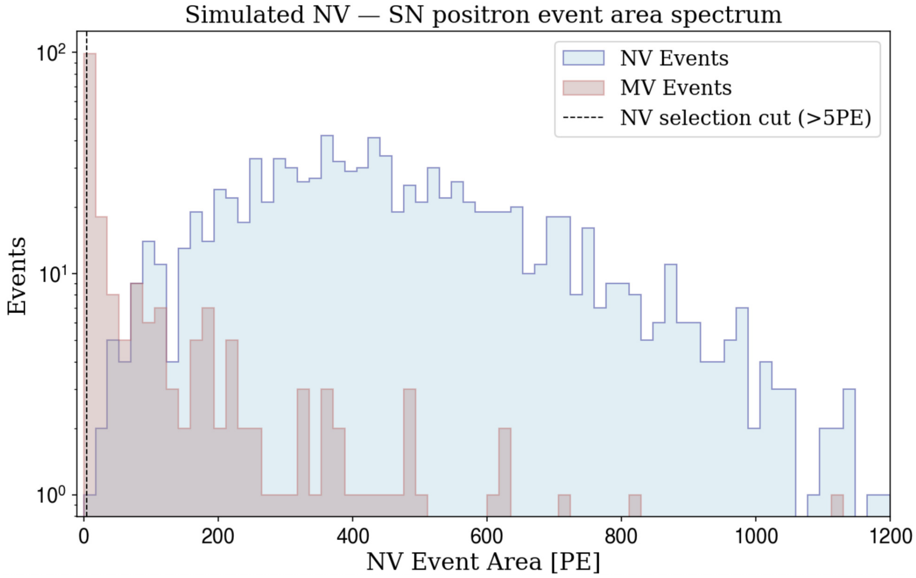

Figure 39: Simulated event area [PE] from positron events detected by the Neutron Veto PMTs, for events generated in the NV (blue) and MV (pink). The NV selection cut (> 5 PE) is also displayed as a black dashed line. The selection cut has already been applied.

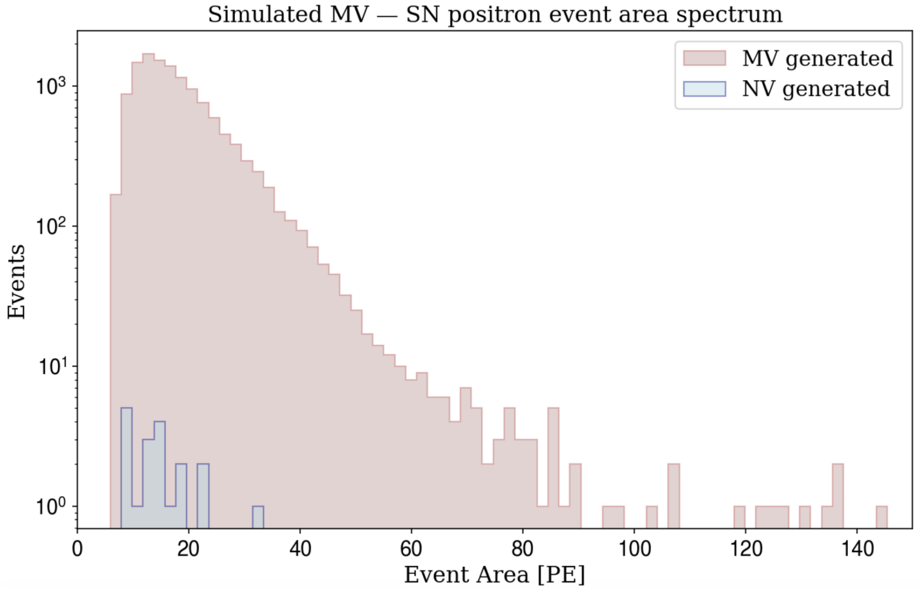

Figure 40: Simulated event area [PE] from positron events detected by the Muon Veto PMTs, for events generated in the NV (blue) and MV (pink).

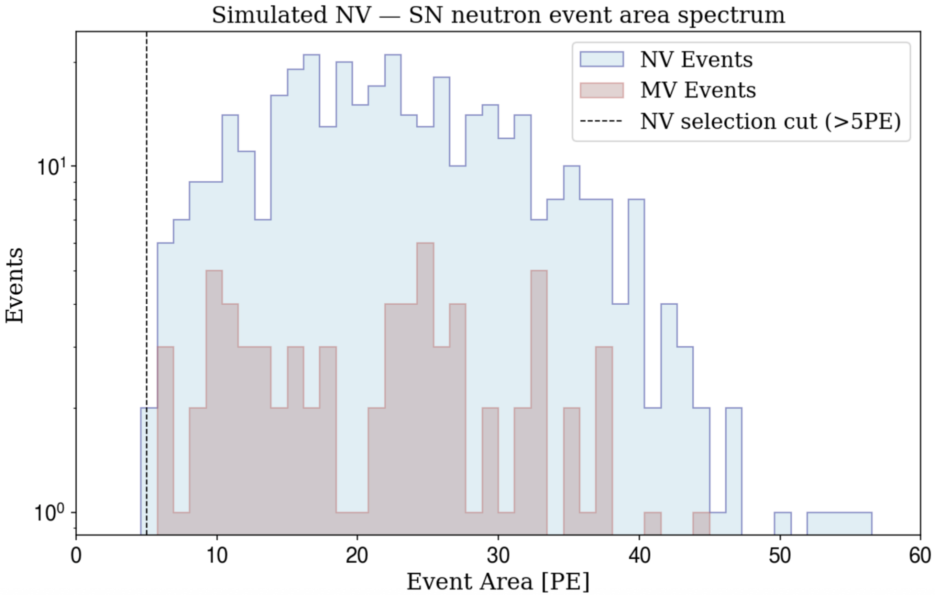

Figure 41: Simulated event area [PE] from neutron events detected by the Neutron Veto PMTs, for events generated in the NV (blue) and MV (pink). The NV selection cut (> 5 PE) is also displayed as a black dashed line. The selection cut has already been applied.

The NV positron region of interest (ROI) is found between 50 and 800 PEs, whereas in the MV is located between 10 and 80 PEs. On the other hand, neutron ROI in the NV is contained in the range that goes from 5 to 40 PEs.

3.3.2 Simulated supernova $\bar{\nu}_e$ detection efficiency in pure water

Simulated neutron detection efficiency

Given the 10^4 neutron events generated in the whole water tank and shown in Fig. 41, those generated inside the NV are selected in order to obtain the Neutron Veto neutron detection efficiency:

$$\varepsilon_{\mathrm{n}}^{\mathrm{NV}}(\text{NV generated events}) = (81 \pm 2)\% \tag{34}$$

whose value is compatible with the obtained neutron detection efficiency during Science Runs 0 and 1, which is $\varepsilon_{\mathrm{n}} = (82 \pm 1)\%$, as mentioned in Section 2.6.2. The efficiency uncertainty has been computed assuming a Binomial distribution.

Simulated positron detection efficiency spectrum

An analog calculation for the Neutron Veto and Muon Veto positron detection has been performed obtaining the following detection efficiencies:

$$\begin{aligned} \varepsilon_{e^+}^{\mathrm{NV}}(\text{NV generated events}) &= 100\% \\ \varepsilon_{e^+}^{\mathrm{MV}}(\text{MV generated events}) &= (67.6 \pm 0.3)\% \end{aligned} \tag{35}$$

In addition to the total positron detection efficiency in both Neutron and Muon Vetoes, we have also obtained the distribution of their efficiency curves in terms of the incoming positron total energy. This means that binned data consists in ratios of simulated events that pass all cuts and detector thresholds over the total number of simulated events, represented in terms of the incident positron energy.

The dependence can be interpreted as a sharp threshold (step function) smeared by the detector energy response, which is typically gaussian. In this way, we convolute a step function or Heaviside function with a skewed Gaussian kernel, in order to smooth the distribution and also consider a tail at high energies, which is caused by a slower response in this range possibly due to the PMT coverage of the detectors with regard to its dimensions, in fact, this effect is more relevant for the MV (see Fig. 43).

In the simplest case, the response is modeled as a Gaussian with width σ, so the efficiency is given by the convolution of a Heaviside step function $H(E-E_0)$ with a normalized Gaussian kernel,

$$g(E;\sigma) = \frac{1}{\sigma\sqrt{2\pi}} \exp\left(-\frac{E^2}{2\sigma^2}\right) \tag{36}$$

The resulting efficiency curve is

$$\eta(E;\sigma) = \eta_{\max} \int_{-\infty}^{+\infty} H(E' - E_0)\, g(E - E';\sigma)\, \mathrm{d}E' \tag{37}$$

which can be written in closed form in terms of the error function as

$$\eta(E;\sigma) = \frac{\eta_{\max}}{2} \left[1 + \mathrm{erf}\left(\frac{E - E_0}{\sqrt{2}\,\sigma}\right)\right] \tag{38}$$

Here, E_0 is the effective threshold energy, $\eta_{\max}$ is the maximum efficiency and σ parametrizes the width of the turn-on region.

If the detector response exhibits an asymmetric tail, the Gaussian kernel can be replaced by a skewed Gaussian distribution $g_{\mathrm{skew}}(E;\sigma,\alpha)$, characterized by an additional asymmetry parameter α.

$$g_{\mathrm{skew}}(E;\sigma,\alpha) = \frac{1}{\sigma\sqrt{2\pi}} \exp\left(-\frac{E^2}{2\sigma^2}\right) \mathrm{erf}\left(-\frac{\alpha E}{\sqrt{2}\,\sigma}\right) \tag{39}$$

In that case, the efficiency is still given by the convolution of the step function with the response function,

$$\begin{gathered} \eta(E;\sigma,\alpha) = \eta_{\max} \int_{-\infty}^{+\infty} H(E'-E_0)\, g_{\mathrm{skew}}(E-E';\sigma,\alpha)\,\mathrm{d}E' = \\ \eta_{\max}\left(\Phi\left(\frac{E-E_0}{\sigma}\right) - 2T\left(\frac{E-E_0}{\sigma},\alpha\right)\right) \end{gathered} \tag{40}$$

which corresponds to the cumulative skew-normal function. The final result of Eq. 40 is expressed in terms of the cumulative Gaussian distribution function $\Phi(x)$, which corresponds to Eq.38. Moreover, a new term appears corresponding to the Owen's T function $T(x,\alpha)$, with $x = (E-E_0)/\sigma$, which is related to the bivariate Gaussian distribution.

For $\alpha = 0$, the skewed kernel reduces to a symmetric Gaussian and the standard error-function parametrization is recovered.

In the skew-normal distribution, the mean is defined as

$$\mu = E_0 + \sqrt{\frac{2}{\pi}} \frac{\alpha\sigma}{\sqrt{1+\alpha^2}} \tag{41}$$

Therefore, considering $\alpha = 0$ a mean corresponding to E_0 would be recovered, which in the symmetric gaussian smeared response function would correspond to the value $\eta_{\max}/2$. In our case, the mean is shifted to higher energies as will be detailed below.

The fit of the distribution shown in Eq. 40 to the energy-dependent positron efficiencies of the Neutron Veto and Muon Veto are displayed in Figs. 42 and 43. Additionally, the best fit parameters as well as their uncertainties are shown in Table 3. Note that the fit has been performed by fixing the maximum efficiency to 1.

Fit parameter	Neutron Veto	Muon Veto
E_0 (MeV)	0.508 ± 0.007	5.0 ± 0.2
σ (MeV)	0.243 ± 0.009	12.6 ± 0.3
α	11 ± 12	7 ± 3

Table 3: Fit parameters obtained from the fitting of skewed-Gaussian convoluted to the step function and the energy-dependent efficiency computed from positron MC simulations. E_0 is the energy threshold, σ the width of the slope, and α the parameter that measures the asymmetry of the skewed distribution.

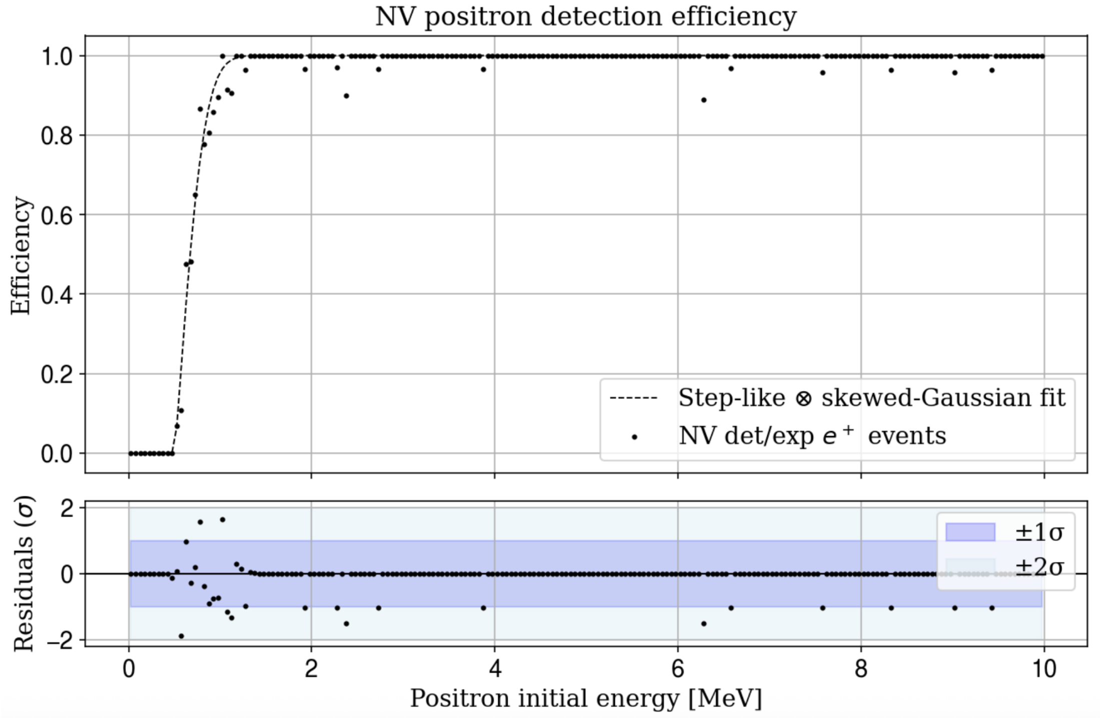

Figure 42: The upper panel shows the step function convoluted to a skewed Gaussian distribution (black dashed line) fitted to the positron efficiency, obtained from NV simulations (black dots). The bottom panel shows the fit residuals.

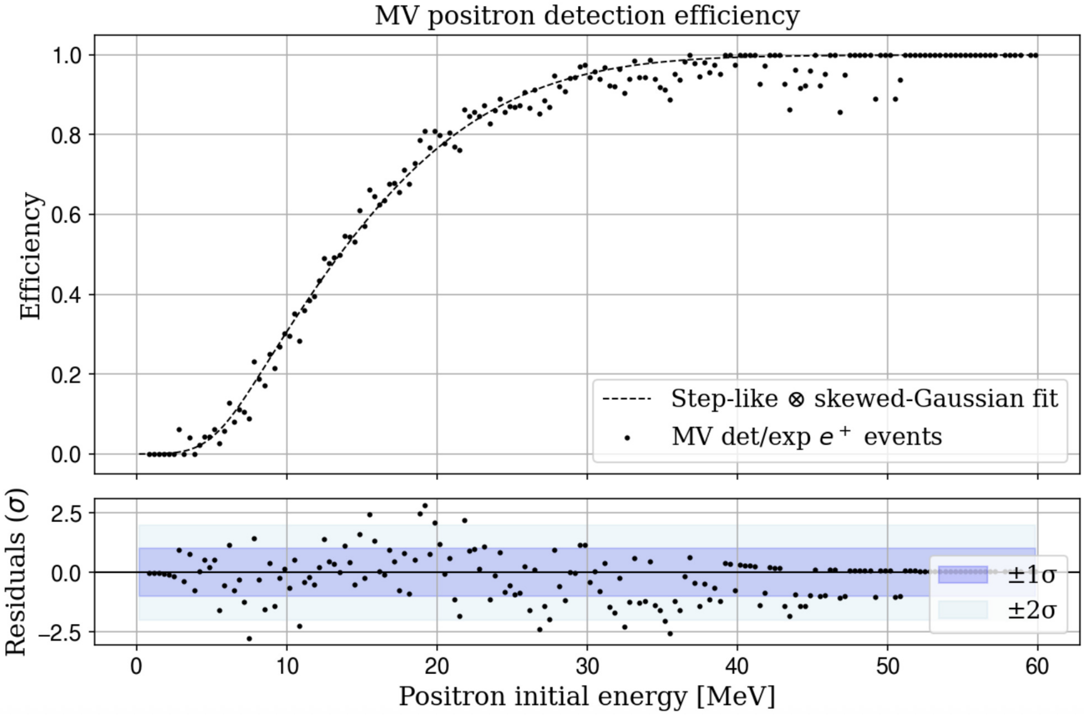

Figure 43: The upper panel shows the step function convoluted to a skewed Gaussian distribution (black dashed line) fitted to the positron efficiency, obtained from MV simulations (black dots). The bottom panel shows the fit residuals.

Detected supernova neutrino IBD events in the Muon and Neutron Vetoes

In this study, the detection of the IBD neutrino interaction will only be analyzed through its positron signal, neglecting the one created by the neutron, due to the former higher efficiency compared to the latter.

Having obtained the efficiency curve parameters, an extrapolation to the other SN neutrino flux models described in this work (Section 1.2.2) can be performed. So, convoluting the energy-dependent positron efficiency curve with the computed expected values of supernova electron antineutrinos interacting through IBD in the water tank (see Tables 1 and 2), we obtain Table 4. Accordingly to what was seen in the two expressions of Eq. 35, Neutron Veto should detect all IBD positron events in the energy range considered in a SN signal, so the model associated efficiencies are not displayed. On the other hand, MV should detect about 60-70% of events. However, in this case we should also consider the energy value at the peak of the neutrino spectrum, recalling Fig. 27, for a SN progenitor of 11.2 $M_\odot$ the neutrino energy at the spectrum maximum is slightly smaller than the one for a 27 $M_\odot$ progenitor, reducing its detection efficiency accordingly to Fig. 43. The last column of Table 4 shows the MV detection efficiency associated to each SN progenitor model in order to describe this effect. However, all efficiencies are found to be compatible.

Figs. 44 and 45 show the expected (black line) and detected (blue line) positron rate in the Neutron and Muon Vetoes, respectively. The latter has been obtained by convolving the black line with the efficiency curve obtained from the fit (Figs. 42 and 43) and shown as a red dashed line. It is worth mentioning that the ~0.5 MeV NV detection threshold allows detecting all positron events.

Model	Exp. NV	Det. NV	Exp. MV	Det. MV	Eff. MV
LS220, 11.2 $M_\odot$	4.3	4.3	84.2	52.4	62 ± 5 %
LS220, 27 $M_\odot$	8.3	8.3	161.6	108.0	67 ± 4 %
SFHo, 27 $M_\odot$	8.6	8.6	167.5	109.5	65 ± 4 %
LS220, 27 $M_\odot$, NO osc.	8.1	8.1	159.5	107.3	67 ± 4 %
LS220, 27 $M_\odot$, IO osc.	7.9	7.9	155.1	106.0	68 ± 4 %

Table 4: Expected IBD interactions with (det.) and without (exp.) considering the positron detection efficiency, obtained from MC simulations, in the NV and MV for different SN models at 10 kpc. Note that in the first three rows, oscillations are not considered, and when NO and IO oscillations are mentioned, we refer to adiabatic conditions. The MV efficiency for each SN model is displayed in the final column.

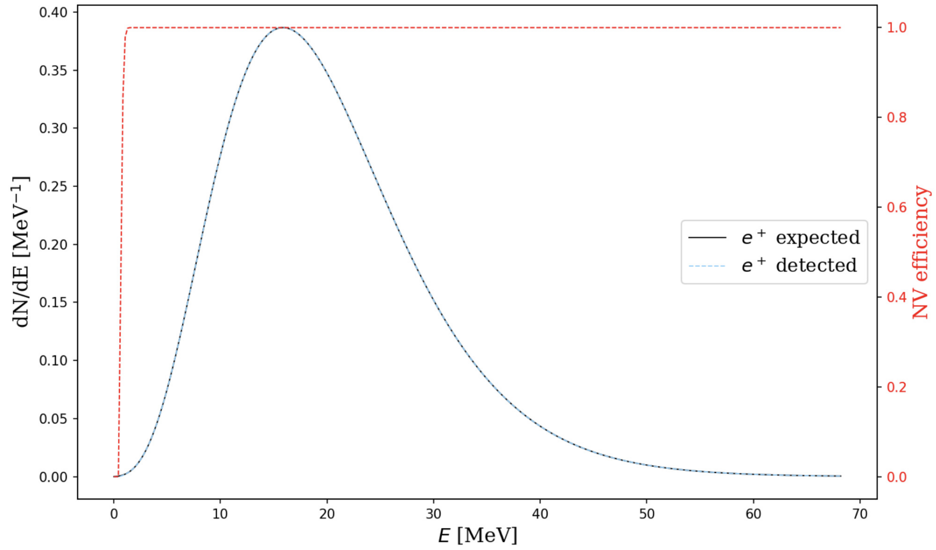

Figure 44: Expected (black) and detected positron spectrum (blue) obtained by convolving the black spectrum with the Neutron Veto efficiency curve (red dashed line) obtained from MC simulations. The SN model considered is a 27 $M_\odot$ SN progenitor at 10 kpc with the LS220 EoS flux without oscillations.

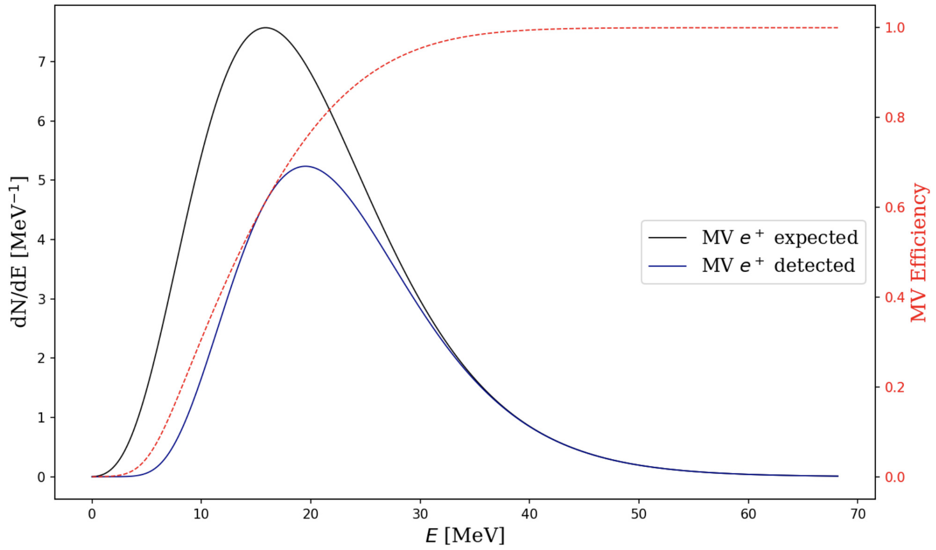

Figure 45: Expected (black) and detected positron spectrum (blue) obtained by convolving the black spectrum with the Muon Veto efficiency curve (red dashed line) obtained from MC simulations. The SN model considered is a 27 $M_\odot$ SN progenitor at 10 kpc with the LS220 EoS flux without oscillations.

3.3.3 XLZD projection for supernova neutrino detection

The XLZD observatory [69] is expected to represent the next generation of direct Dark Matter detectors. Based on the expectations of supernova neutrino detection via IBD obtained in this chapter for the XENONnT vetoes, we provide an estimate of the required volume of the XLZD vetoes, for several SN distances of emission. For reference, one proposed configuration for the XLZD vetoes includes having a Neutron Veto similar to that of XENONnT, but with a cylinder structure with an 8 m height, an 8 m diameter (337 tonnes, considering the volume occupied by the cryostat) and 316 PMTs. In addition, the design foresees a Muon Veto with a height and diameter of 12 m (955 tonnes, accounting for the internal NV volume) equipped with 129 PMTs. The cryostat is assumed as a cylindrical structure with a 4 m diameter and a 5.2 m height that occupies a volume of about 65 m^3.

In this study, we assume that the XLZD vetoes will achieve supernova neutrino-induced positron detection efficiencies comparable to those of XENONnT (see Figs. 42 and 43) by maintaining a similar PMT coverage, reflectivity, and water absorption length. Considering Eq. 30 and 20, a relation between the distance from the SN progenitor and the detector volume is obtained. The SN model of a 27 $M_\odot$, LS220 EoS progenitor star is considered.

Table 5 presents three possible supernova distance scenarios and the corresponding Neutron and Muon Vetoes pure water volumes required to detect 100 positrons produced by supernova neutrino inverse beta decay. For comparison, the first NV configuration (shown as a blue vertical dotted line in Fig. 46) displayed in the table would be similar to the proposed one, whereas the second would already be almost five times larger. In fact the second and third NV volumes reported are not realistic but included for completeness. Similarly for the MV results, the first configuration would be smaller than the proposed one (and the XENONnT MV), whereas the second one would be more than twice its size. This configurations are shown as red vertical dotted lines in Fig. 46.

Fig. 46 shows the relation between the distance from the supernova and the XLZD NV (blue) and MV (red) water volume, in order to detect 100 events with their respective efficiencies. The sum of the benchmark 337 t NV volume and the full MV range considered in the plot, is shown as a black curve. The total XLZD water tank volumes needed to detect 100 supernova neutrino-induced positron events within a 10 s burst at a distance of 20 and 30 kpc are 2297 and 5380 tonnes of pure water, approximately. The proposed configuration of about 1.3 kilotonnes of pure water would be able to detect at least 100 events up to SN distances of about 15 kpc as shown in Fig.46.

SN distance [kpc]	XLZD NV volume	XLZD MV volume
10	410 tonnes	617 tonnes
20	1649 tonnes	2467 tonnes
30	3711 tonnes	5550 tonnes

Table 5: XLZD projection: NV and MV water volumes for three different supernova distances in order to detect approximately 100 supernova neutrino-induced positron events. The detection efficiencies are assumed to be those of XENONnT (Figs. 42 and 43).

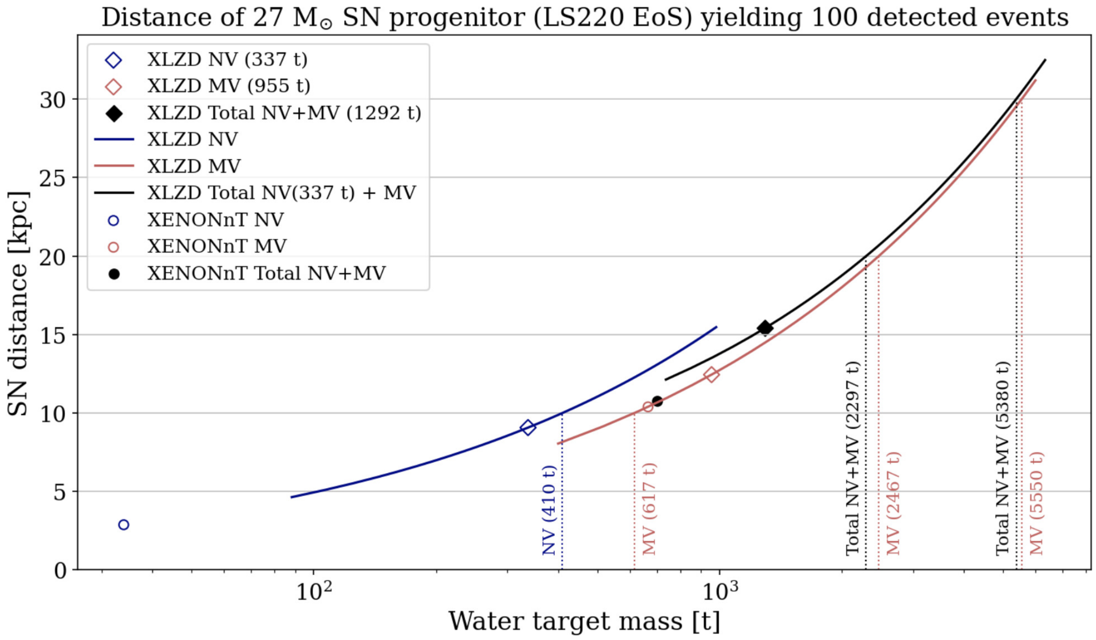

Figure 46: Water volume of the XLZD Neutron (blue) and Muon (red) Vetoes needed to detect 100 events for different SN distances (as shown in Table 5), assuming a 27 $M_\odot$ SN progenitor with LS220 EoS. The black solid line represents the whole XLZD water tank volume as the sum of the benchmark NV volume (337 t) and the full MV volume range (red solid line). Colored squares and circles represent the SN distances at which the proposed XLZD and XENONnT NV, MV and MV+NV configurations yield 100 positron events, respectively. Vertical dotted lines indicate the corresponding veto water mass for the detection of 100 events due to a SN a distance of 10, 20 and 30 kpc.

4 Study of atmospheric neutrinos with the XENONnT Vetoes

The effects that atmospheric neutrinos would induce in next-generation direct Dark Matter detection experiments were introduced in Section 2.7. This Chapter will examine in more detail the characteristics and flux uncertainties of this type of neutrinos in Section 4.1.1, followed by a description of the interactions that low-energy atmospheric neutrinos undergo in water in Section 4.1.2. Finally, by convolving the two previous components, the expected number of interactions per year and per tonne of detector mass, considering either the entire water tank or its two veto subsystems, the Neutron Veto and Muon Veto, will be obtained in Section 4.1.3.

Building on this, Section 4.2.1 will analyze, using GEANT4 simulations, the event area distributions for the four most relevant neutrino flavors in this energy regime, followed by an evaluation, in Section 4.2.2, of the detection efficiency of these events in both the Neutron Veto and Muon Veto. Lastly, the projection to the next-generation XLZD observatory will be presented in Section 4.2.3.

4.1 Expected atmospheric neutrino rate in the water Cherenkov Vetoes

4.1.1 The low-energy atmospheric neutrino flux and its uncertainties

The low-energy regime of atmospheric neutrinos is the focus of this work, as it significantly impacts the coherent neutrino-nucleus scattering background in the XENONnT WIMP region of interest within the nuclear recoil spectrum of the Time Projection Chamber.

In this regime, the flavor ratio is well under control, since these low-energy neutrinos are produced in a regime where the decay chain $p \rightarrow \mu \rightarrow \nu$ is fully effective since most muons decay before hitting the ground, and the kaon contribution to neutrino production is practically negligible here. On the other hand, at higher neutrino energies, above 1 GeV, the fraction of muons hitting the ground before decaying increases, leading to a higher fraction of muon neutrinos and antineutrinos with regard to the electronic flavor.

Neutrino flux Φ is defined as the energy spectrum $\mathrm{d}N/\mathrm{d}E$ of neutrinos produced per unit area A, unit time t, and solid angle Ω as viewed from the detector:

$$\Phi_\nu(E,\Omega) = \frac{\mathrm{d}N}{\mathrm{d}E\,\mathrm{d}A\,\mathrm{d}t\,\mathrm{d}\Omega}. \tag{42}$$

In spherical coordinates, the unit solid angle is $\mathrm{d}\Omega = \mathrm{d}\cos\theta_{\mathrm{zen}}\,\mathrm{d}\varphi$, where θ_{zen} is the zenith angle, defined by the orientation of the neutrino arrival direction relative to the detector axis, and φ is the corresponding azimuthal angle.

Assuming that neutrinos do not change flavor during propagation from the production point in the atmosphere to the detector, one can obtain two fundamental and very robust properties: at energies below a few GeV, the flux of ν_μ is approximately twice as large as the flux of ν_e, $\Phi_{\nu_\mu} \simeq 2\Phi_{\nu_e}$, due to the multiplicities of each of the two neutrino flavors, described in Eqs. 12 and 13. Moreover, the fluxes of all neutrino species are up-down symmetric in the zenith angle θ, which means that $\Phi_{\nu_x}(E_\nu,\theta) = \Phi_{\nu_x}(E_\nu,\pi-\theta)$. This phenomenon is shown in Fig. 8-right.

If oscillations occur, the up-down symmetry would be broken and the effect could be easily observed by measuring a difference in the rates of upgoing and downgoing events of different flavors [3], [4], [23], [76].

Uncertainties and flux variations

The cosmic ray flux at the lowest energies is modulated by the solar cycle, inducing a time variation that is expected to propagate into the atmospheric neutrino flux at these energies. This is because cosmic rays reaching the top of the atmosphere interact with the solar wind and the solar magnetic field within the heliosphere. The solar cycle has a period of 11 years from one minimum to the next, in which more incoming interstellar particles are allowed.

It has been found [81] that between a solar minimum and a solar maximum, the normalization of the flux changes by approximately 30% at a high-latitude location such as the Sanford Underground Research Facility, while it changes by a smaller amount, of the order of less than 10%, at the Laboratori Nazionali del Gran Sasso. A Dark Matter detector that runs for a period extending through solar cycles will be most effective at identifying this time variation. This opens the possibility to distinguish such neutrino-induced nuclear recoils from Dark Matter-induced nuclear recoils, thus allowing for the possibility of using timing information to break through the “neutrino fog.”

A second challenge to predict the interaction rate of a flux of atmospheric neutrinos involves properly modeling the geomagnetic field. When low-energy (≤ 10 GeV) cosmic rays approach the Earth, they are deflected by the geomagnetic field due to the rigidity cut-off. The rigidity cut-off determines which cosmic rays can enter the Earth, and it varies with the arrival direction at each location on Earth. As a consequence, the flux of low-energy neutrinos is higher for detectors located near the poles than for those near the equator.

A futuristic detection of these neutrinos could provide new insight into the structure of the geomagnetic field and cosmic ray flux at low energy, as the latter is one of the most relevant contributions to the flux uncertainty.

Other contributions to this uncertainty include cross section uncertainties from the interactions between protons and the nuclei present in the atmosphere.

Atmospheric-neutrino mixing

At low energies, the flux ratio combining neutrinos and antineutrinos is approximately $\nu_e : \nu_\mu : \nu_\tau \simeq 1 : 2 : 0$ before oscillations. In vacuum, neutrino oscillations depend on the energy and the baseline (or, equivalently, the zenith angle), and the dominant $\nu_\mu \rightarrow \nu_\tau$ oscillation, with an associated mixing angle of about 45^o [71], drives the flavor ratios towards $\nu_e : \nu_\mu : \nu_\tau \simeq 1 : 1 : 1$.

As atmospheric neutrinos propagate through the Earth, however, the situation becomes more complex because matter effects modify the vacuum oscillation pattern. The Earth is composed of layers with very different densities: crust, mantle, and core, so neutrinos crossing different trajectories experience different matter potentials. This leads to characteristic distortions in the oscillation probabilities as a function of energy and zenith angle, particularly for neutrinos between 0.1-1 GeV and those around 6 GeV or so, where MSW resonances, mentioned in Section 3.1.1, happen. Although these enrich the overall oscillation pattern, their impact is still smaller than the uncertainties associated with the atmospheric flux itself [4], [13], [82].

FLUKA atmospheric neutrino flux at LNGS

Figs. 47 shows, as red and black dots, flux tables for the LNGS made with FLUKA calculations [23] without taking into account the effect of local atmosphere and ground profile (mountain shape, elevation...) that may account for a few percent systematics in the determination of low-energy atmospheric neutrino fluxes. These fluxes are angle integrated and solar-cycle averaged for energies from 10 MeV to 1 GeV. Solar-averaged fluxes are indeed appropriate for long data runs. Moreover, neutrino oscillations are not taken into account in these tables.

The structures visible in the shape below 100 MeV come from the decay at rest of pions and muons, which stop as they arrive at the end of their range.

The monochromatic spike in the ν_μ and $\bar{\nu}_\mu$ fluxes (Fig. 47–right) at about 30 MeV is due to the two-body decays $\pi^+ \rightarrow \mu^+ + \nu_\mu$ and $\pi^- \rightarrow \mu^- + \bar{\nu}_\mu$. The decay $\pi^+ \rightarrow e^+ + \nu_e$ is also accounted for, but due to the much smaller branching ratio the effect is negligible on the electron neutrino flux, shown in red in Fig.47–left . The shoulder at about 53 MeV in both muon and electron neutrino plots is due to the decay at rest of muons ($\mu^+ \rightarrow e^+ + \nu_e + \bar{\nu}_\mu$ and its charge conjugate). Negative pions captured undergoing nuclear interactions, and the atomic capture probability of negative muons are also accounted for, where neutrinos can be produced through scattering with one or more nucleons.

The differences between neutrinos and antineutrinos, for both flavor cases, show the different abundances of π^+ and π^- produced in p-nucleus collisions and the capture probabilities of pions and muons. This latter essentially explains why electron neutrinos and muon antineutrinos (both from μ^+ decay) have larger fluxes than their associated antineutrinos and neutrinos, respectively. At high energies, the spectra of ν_μ and $\bar{\nu}_\mu$ follow the well-known power law of the parent cosmic rays, $dN/dE \sim E^{-2.7}$, while the spectra of ν_e and $\bar{\nu}_e$ are steeper due to those muons reaching the ground before decaying.

These fluxes are provided as a histogram with the energy values located at the bin centers for 40 equally spaced logarithmic energy bins between 10 MeV and 1 GeV.

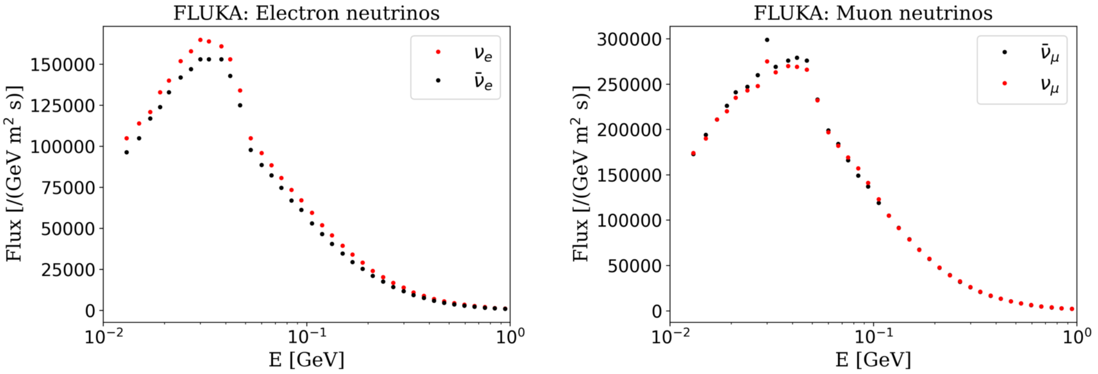

Figure 47: Atmospheric neutrino fluxes for the four relevant flavors, $\nu_e, \bar{\nu}_e, \nu_\mu$ and $\bar{\nu}_\mu$, taken from FLUKA [23] tables for LNGS site. Neutrinos are illustrated in red whereas antineutrinos are shown in black. A spike at about 30 MeV is present in the muon neutrinos spectra.

The total energy-integrated atmospheric fluxes for each neutrino flavor, shown in Table 6, are computed considering that the flux values are distributed in equally spaced logarithmic energy bins. Being conservative, the neutrino flux uncertainties adopted, considering the effects mentioned above, are ~ 25% for 10–100 MeV and ~ 20% for 0.1–1 GeV.

	dΦ/dtdA ($m^{-2}s^{-1}$)
ν_e	$1.85 \cdot 10^4$
$\bar{\nu}_e$	$1.66 \cdot 10^4$
ν_μ	$3.53 \cdot 10^4$
$\bar{\nu}_\mu$	$3.54 \cdot 10^4$

Table 6: Energy-integrated FLUKA [23] atmospheric fluxes for ν_e,$\bar{\nu}_e$, ν_μ and $\bar{\nu}_\mu$ neutrinos.

The flux predictions used [23] are based on old cosmic-ray data. Other references, such as [81], could be used in future works since they adopt more recent measurements with smaller uncertainties, so they could reduce the flux-prediction uncertainties by about a factor of two.

4.1.2 Atmospheric neutrino interactions in water

Supernova neutrinos, as seen in Chapter 3, create signals that range up to a few tens of MeV, and the most important interaction is the electron antineutrino inverse beta decay on hydrogen. At these neutrino energies, their interactions with compound nuclei and those with electrons are suppressed.

For atmospheric neutrinos, which range from several tens of MeV to a peak in the GeV range with a falling spectrum at higher energies, the dominant interactions are with bound nucleons in oxygen (a pure water target is composed of 88.79% ^{16}O and 11.21% H). Except at the lowest neutrino energies, interactions with hydrogen are suppressed by the low number density. Neutrino-nucleus interactions are complex and hard to handle analytically; for this reason, it was decided to adopt a full simulation with GENIE.

The ROOT-based GENIE Neutrino Montecarlo Generator [76] has the long-term goal of developing a "canonical" neutrino interaction physics Montecarlo, whose validity extends to all nuclear targets and neutrino flavors from MeV to PeV energy scales. The origin and focus of this generator came from long-baseline precision neutrino experiments using accelerator-made beams.

GENIE takes into account the neutrino-nucleus interaction vertices, nuclear effects, hadronization, final-state interactions, de-excitation of the final-state nucleus, and other processes. The results of GENIE are surely not perfect, but they are adequate to guide the exploration of the physics of neutrino interactions.

In this work, GENIE v3.06.00 is used with two different model sets and their two specific physics tunes [83], [84]. The first, which is the default model tune of this version, is "G18_02a_00_000". It uses a relativistic Fermi gas (RFG) nuclear model and the Llewellyn-Smith (LS) model [85] for CC quasi-elastic scattering interactions. Especially for both CC and NC multi-nucleon processes, it is expected to somehow overestimate the cross sections. This model will be referred to as RFG-LS. On the other hand, the model tune "G18_10a_02_11b" embeds the best theoretical model implemented in GENIE so far. It uses the local Fermi gas nuclear (LFG) model and the theory calculations of Nieves, Amaro, and Valverde (NAV) for the CC quasi-elastic [86] and multi-nucleon processes. This model will be referred as LFG-NAV.

The neutrino-nucleon cross sections, belonging to the GENIE models [77] just introduced, are summarized in Figs. 48 and 49, where the contribution to the total CC cross section of the interactions with the two different targets is shown for the two models, RFG-LS and LFG-NAV. The former displays electron neutrinos, whereas the latter presents the muon ones. As seen in both figures, the default model considered tends to overestimate the cross section, so from now on the LFG-NAV model will be used. It is worth noting that in the energy region relevant for supernova neutrino IBD, both cross sections coincide. Consequently, the simplified RFG-LS model remains fully applicable in that range.

At lower energies in Figs. 48 and 49, the steeper slope indicates the importance of nuclear effects and hence greater uncertainties. For nuclear targets, antineutrinos have smaller cross sections than neutrinos; note that hydrogen targets are a special case due to the lack of neutrons (CC quasi-elastic scattering of neutrinos). The most important target is oxygen, due to its large number of nucleons compared to hydrogen; this changes only at the lowest energies, due to kinematic effects caused by the nuclear binding, which is of the order of 10 MeV in oxygen.

Then, in Figs. 50 and 51, the different contributions from CC and NC interactions are shown for the two hydrogen and oxygen targets. Accordingly to kinematical constraints, NC cross sections have lower energy thresholds; however, their values are clearly smaller than the CC ones. These behaviors explain the difference in CC and NC contributions to each type of interaction, shown in Table 7.

The neutrino-nucleus cross sections relevant to this work have large uncertainties. In works like [82] overall uncertainties of $\sim 20\%$ in this energy range are assumed.

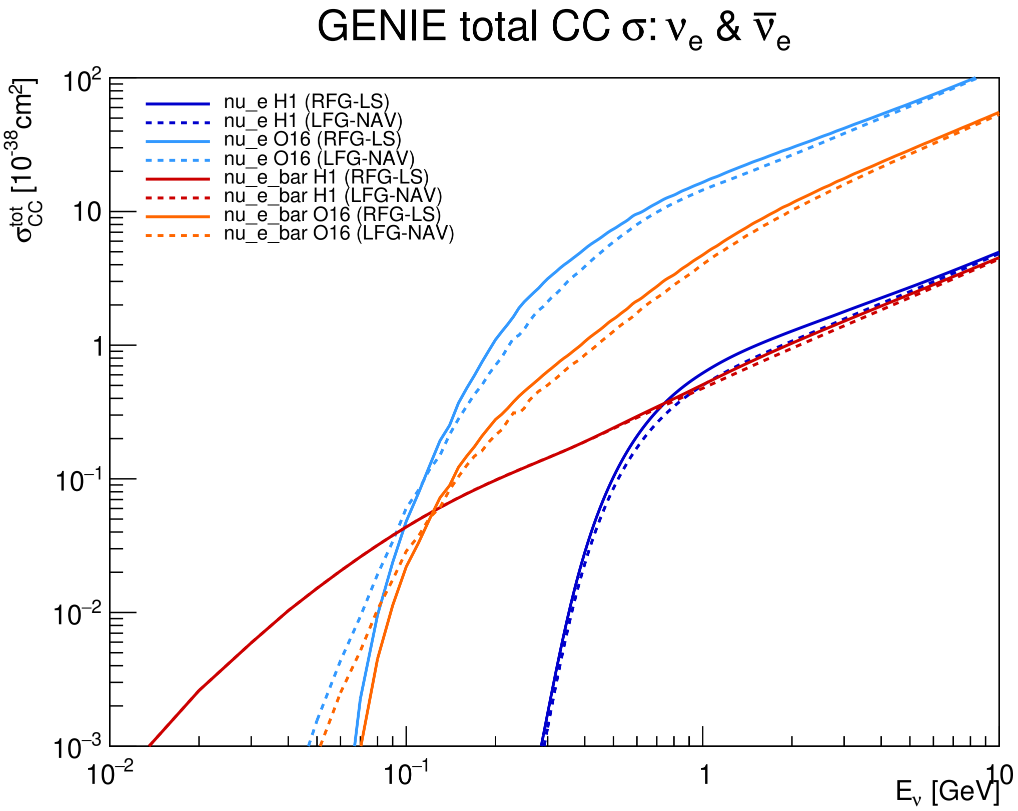

Figure 48: Atmospheric neutrino charged current interactions on H and ^{16}O for ν_e and $\bar{\nu}_e$ taken from GENIE [77] splines. The two models considered, RFG-LS and LFG-NAV are shown. The well-known inverse beta decay is illustrated as a red line.

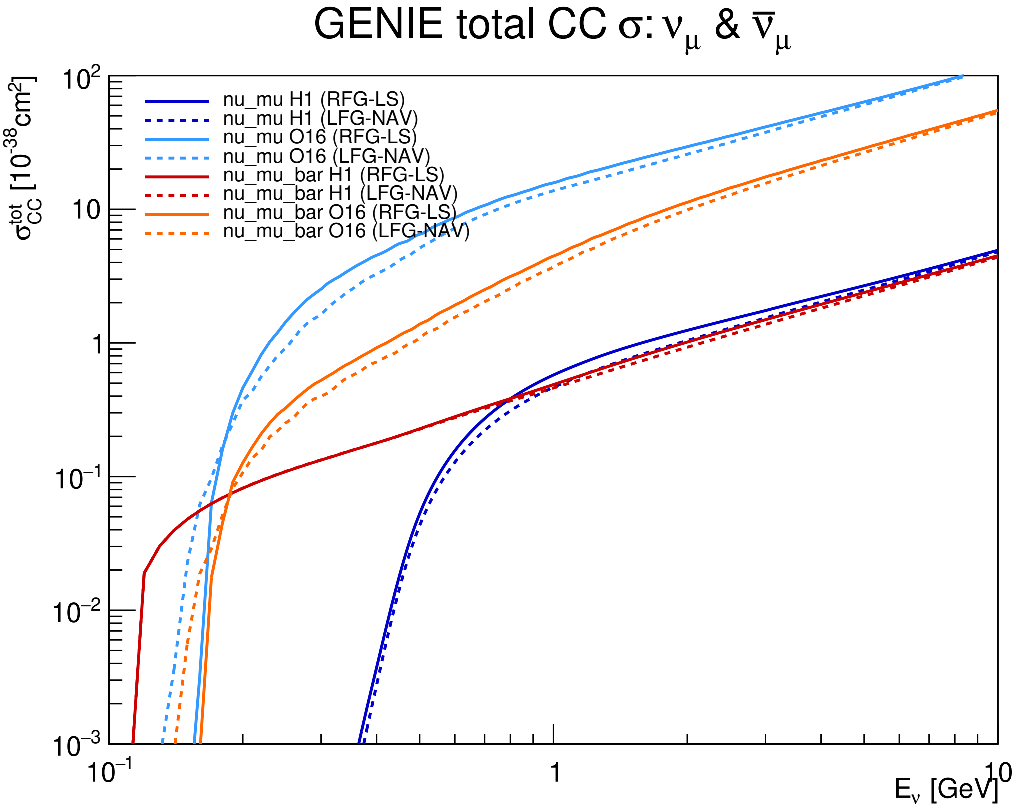

Figure 49: Atmospheric neutrino charged current interactions on H and ^{16}O for ν_μ and $\bar{\nu}_\mu$, taken from GENIE [77] splines. The two models considered, RFG-LS and LFG-NAV are shown, with a range starting from 100 MeV due to the process thresholds.

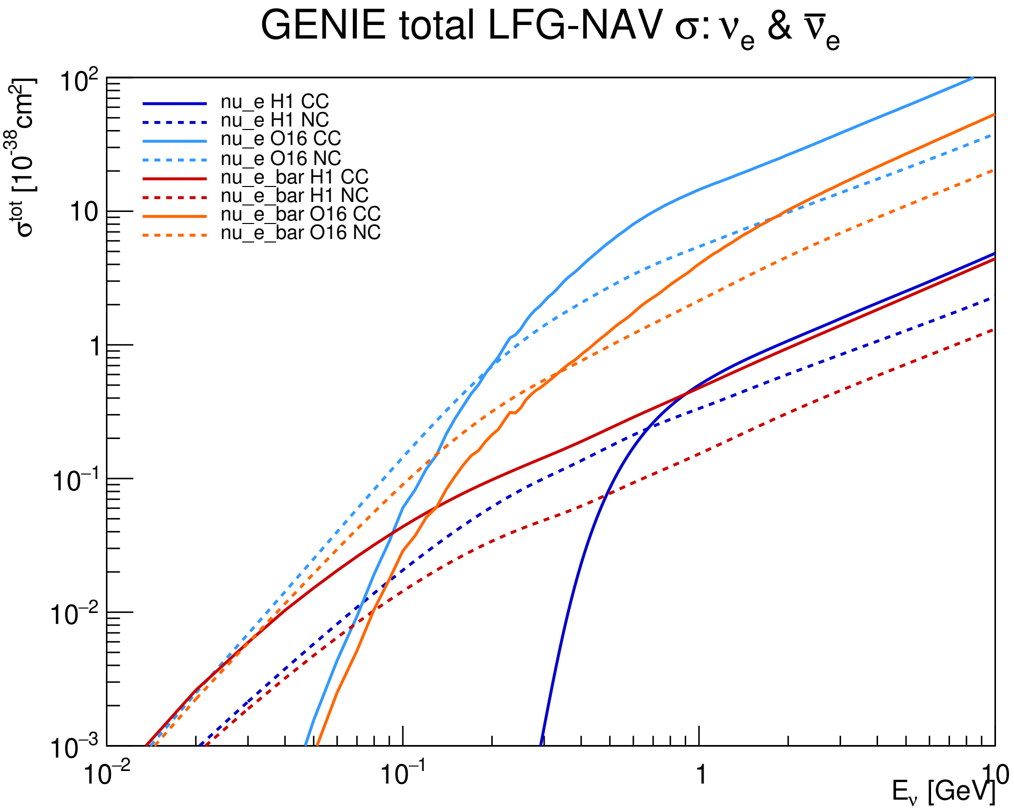

Figure 50: Atmospheric neutrino charged and neutral current interactions on H and ^{16}O for ν_e and $\bar{\nu}_e$, taken from GENIE [77] splines. Only the LFG-NAV model is shown.

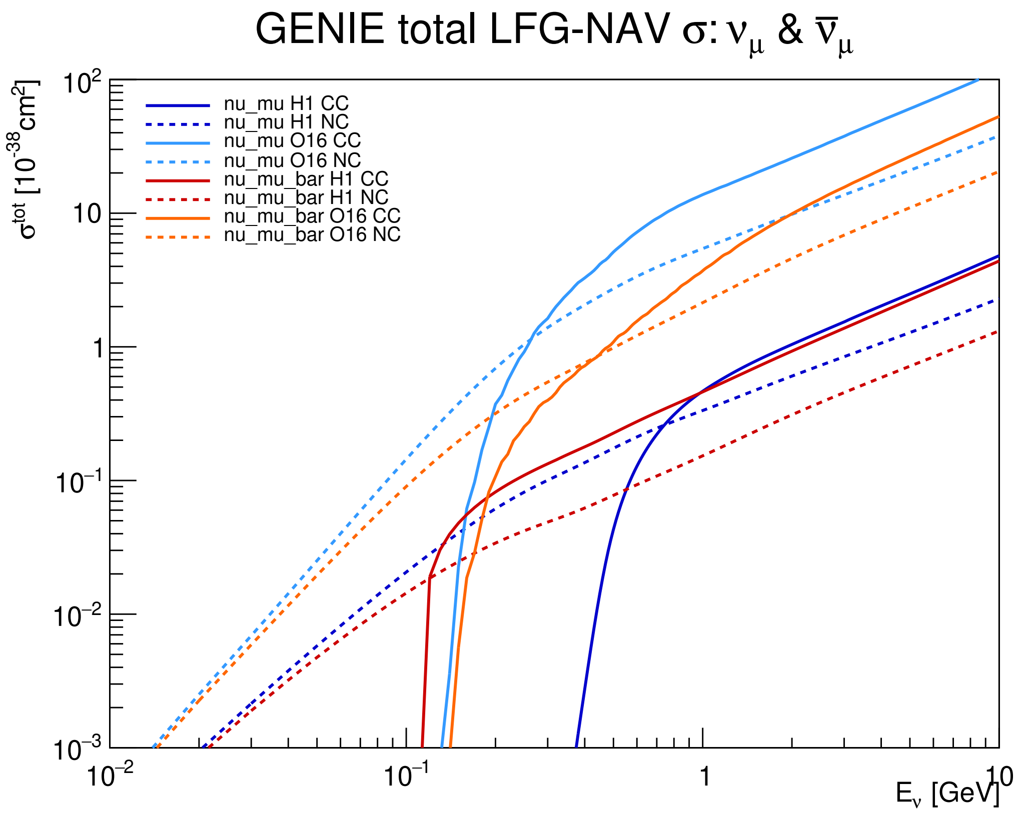

Figure 51: Atmospheric neutrino charged and neutral current interactions on H and ^{16}O for ν_μ and $\bar{\nu}_\mu$, taken from GENIE [77] splines. Only the LFG-NAV model is shown.

Neutrino-nucleon interactions at these energies, introduced in Section 1.1.3, can be mainly described as quasi-elastic scattering (QES), which is dominant below 1 GeV. Charged current QES (CCQES) interactions are dominant, with some contributions neutral current elastic scattering (named as NCQES in Table 7), CC and NC resonant pion production (RES), and multi-nucleon processes (MNP), essentially mediated by CCs. The deep-inelastic scattering (DIS) slightly contributes to the total cross section. Even smaller contributions come from diffractive and coherent pion production, through interactions with hydrogen and oxygen, respectively. Table 7, shows the contribution provided by QES, RES, MNP, and DIS, as well as their respective division into CC and NC mediated interactions.

In Fig. 52, ν_e+^{16}O CC interaction is taken as an example to show the several possible interactions in the energy range considered (between 0.01 and 1 GeV), as explained above. Neutron nuclear binding is one of the main causes of the energy threshold of the CCQES. Following this interaction, MNP and RES have the highest contributions, which is compatible with the results of the table.

Int.	QES			RES			MNP			DIS		
+H_2O	Tot.	CC	NC	Tot.	CC	NC	Tot.	CC	NC	Tot.	CC	NC
ν_e	75%	59%	41%	15%	73%	27%	10%	73%	27%	<1%	37%	63%
$\bar{\nu}_e$	83%	57%	43%	7%	57%	43%	9%	70%	30%	<1%	38%	62%
ν_μ	77%	54%	46%	13%	66%	34%	9%	68%	32%	<1%	31%	69%
$\bar{\nu}_\mu$	84%	51%	49%	6%	44%	56%	9%	64%	36%	<1%	31%	69%

Table 7: Summary of GENIE simulated interaction fractions for atmospheric neutrinos in water. Each interaction mode (QES, RES, MNP, DIS) lists its total fraction of events and the CC/NC sharing.

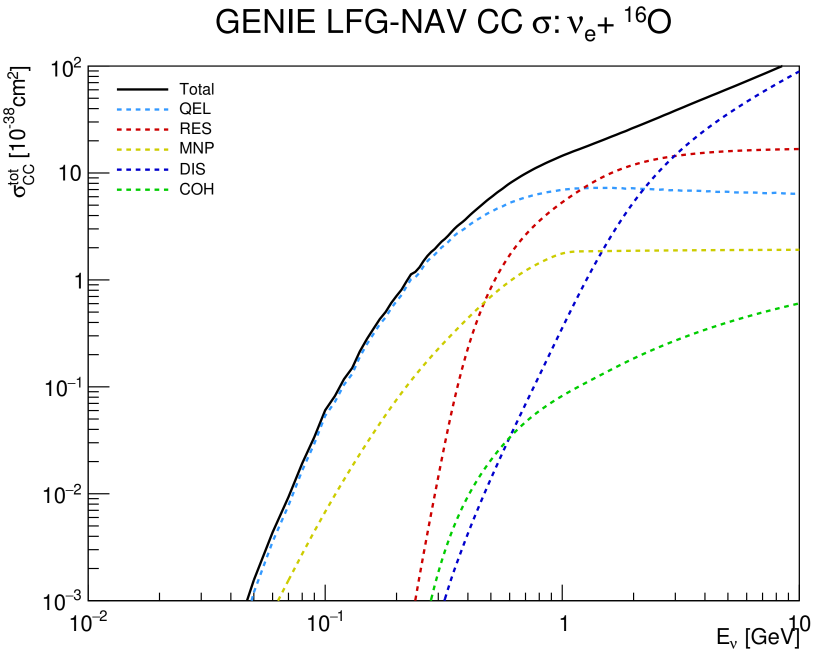

Figure 52: Atmospheric electron neutrino charged current interactions on ^{16}O taken from GENIE [77] splines. Only the LFG-NAV model is shown. The contributions of the different interaction channels are displayed as different dashed colored lines, with their total sum given as a solid black line.

4.1.3 Expected interaction spectrum in the Vetoes

The total rate of expected atmospheric neutrinos of different flavors, ν_x, for each energy bin, E_i, and integrating over the arrival direction, is defined by:

$$\frac{dN_i^{\nu_x}}{dE_i} = \Delta t \frac{d\Phi_i^{\nu_x}(E_i)}{dE_i dt} (N_H \sigma_i^H(E_i) + N_O \sigma_i^O(E_i)) \tag{43}$$

where N_H and N_O are the number of targets of H and O in water molecules in the considered amount of tonnes, Δt is the exposure time, Φ_i is the flux in the energy bin i in units of $\mathrm{GeV^{-1}m^{-2}s^{-1}}$ and σ_i^N is the cross section in the energy bin i, in units m^2 for each target nuclei and considering charged and neutral currents.

Analogously to the expected interaction spectrum computed for supernova neutrinos in the whole water tank, the atmospheric neutrino rate is obtained using as input the FLUKA LNGS flux for each neutrino flavor and GENIE cross section splines of the LFG-NAV model, considering the total cross section on hydrogen and oxygen targets (CC+NC). Additionally, as shown in Eq. 43, this convolution is performed by considering the number of H and ^{16}O targets in 700 tonnes of water and their associated cross sections. An exposure time of one year is considered, due to the low atmospheric rate. The obtained spectra considering Eq. 43 are shown in Fig. 53. Note that the FLUKA tables provide the flux at the center of equally spaced $\log_{10}$E bins in the 0.010 and 1 GeV range.

It is worth noting that in the low-energy region, the only interaction significantly contributing to the spectrum is that of electron antineutrinos on free protons. Furthermore, according to the previously introduced predictions, the dominant interactions across the full energy range are those of muon and electron neutrinos with oxygen. This is due to their relatively large charged-current cross sections and fluxes, combined with the fact that oxygen constitutes the majority of the water's mass.

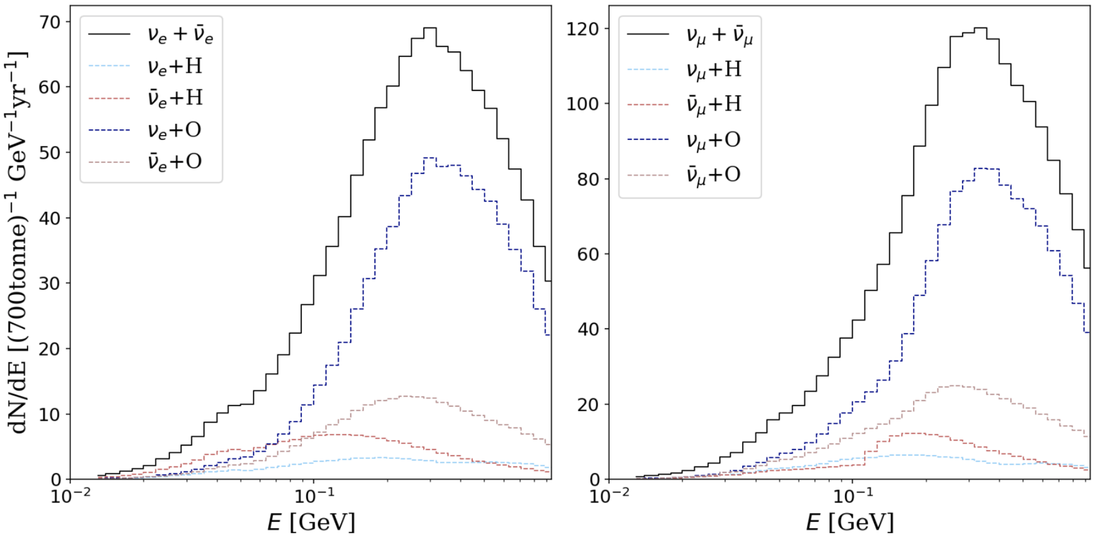

Figure 53: Differential atmospheric neutrino interaction spectrum in one year and the whole water tank. The left figure shows the sum of the two electron neutrino contributions as a solid black line and the ones with the two targets, hydrogen and oxygen, separately for each neutrino. The right figure displays the same, but in the case of muon neutrinos.

Expected atmospheric events in one year: WT, MV and NV

From these spectra, and considering that the NV contains approximately 34 tonnes of water while the MV corresponds to the remaining volume, we integrate over the full energy range Eq. 43 and obtain the following total number of atmospheric neutrino–induced events in the Water Tank, with their sharing between the Neutron and the Muon Veto.

Flavor	NV	MV	NV + MV
ν_e	1.2	24.3	25.5
$\bar{\nu}_e$	0.4	7.9	8.3
ν_μ	2.1	40.8	42.9
$\bar{\nu}_\mu$	0.8	15.3	16.1
Total [yr^{-1}]	4.5	88.3	92.8

Table 8: Expected atmospheric neutrino interactions per year for each flavor in the Neutron Veto, Muon Veto, and in the whole Water Tank.

The uncertainties of these values, according to what was mentioned earlier in Sections 4.1.1 and 4.1.2 and considering that flux and cross section uncertainties are independent, should be of about 30%.

Final-state spectra of atmospheric neutrino interactions in water

In contrast to the simplified analytical computation of the positron spectrum that was performed in the supernova neutrino study, in the case of atmospheric neutrinos the multi-particle final-state spectra must be obtained from simulations. To do so, we have generated four simulations, one for each flavor, of 10^5 neutrinos interacting with a water target, using as inputs the FLUKA LNGS atmospheric neutrino flux and the LFG-NAV cross section splines.

In the following, some of the output spectra of these simulations will be presented. Charged leptons of the same flavor are represented in the same figure, as shown in the first row of Fig. 54. Charged (red) and neutral (blue) pions produced by different interactions are also shown in the second and third rows of Fig. 54.

Considering the Cherenkov thresholds of the particles shown, which are associated with total energies of 0.77, 160, and 211 MeV for $e^{\pm}$, $\mu^{\pm}$, and $\pi^{\pm}$, respectively, it should be noted that most of these particles have energies above their corresponding thresholds, so they will contribute to the overall signal.

Moreover, as summarized in Table 7, in fact the only interaction that will significantly contribute to pion generation is the resonant pion production (RES) since the other three channels account for only ~1% in this energy region. It is worth mentioning that some leptons are not generated by their corresponding CC neutrino interaction, but can instead arise from other processes. Electrons generated in NC neutrino-electron elastic scattering are an example, although their contribution accounts for less than 1%.

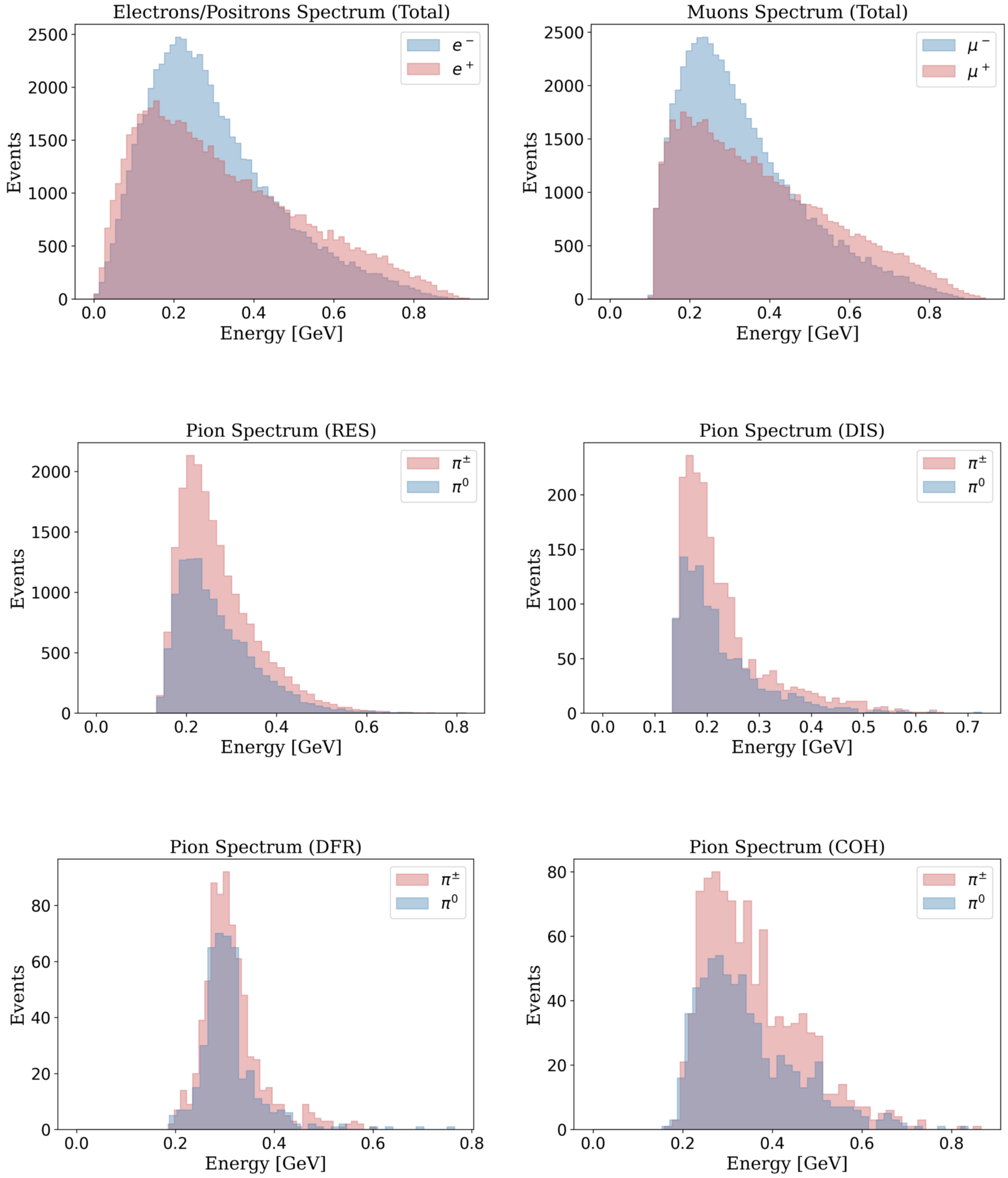
Electrons/Positrons Spectrum (Total)

Muons Spectrum (Total)

Pion Spectrum (RES)

Pion Spectrum (DIS)

Pion Spectrum (DFR)

Pion Spectrum (COH)

Figure 54: Atmospheric neutrino final state spectra for ν_e, $\bar{\nu}_e$, ν_μ and $\bar{\nu}_\mu$. The total spectra, from all neutrinos and interactions, of electrons and positrons are shown in the left figure of the 1st row, while ± muons are displayed in the right one. The four dominant pion production channels are shown in the 2nd and 3rd rows, with charged pions (red) and neutral pions (blue) spectra.

4.2 Atmospheric neutrino simulations in the XENONnT Water Cherenkov Vetoes

4.2.1 Event area for atmospheric neutrino products

The GENIE simulation output files shown in the panels of Fig. 54 were converted into a format suitable for a multi-particle vertex GEANT4 generator. This generator was custom-designed to read a plain-text file containing, for each neutrino interaction generated with GENIE, the event ID, the number of final-state particles, followed by one line per particle with its PDG code, three-momentum, and total energy.

In this way, we generated $5{\cdot}10^3$ isotropically distributed events within the XENONnT model in GEANT4, sampled from the original 10^5 GENIE interactions. To increase the Neutron Veto statistics, two independent sets of simulations were produced, one confined to a volume slightly larger than the NV and another covering the full water tank. These outputs were subsequently processed by the MV and NV Hitlet Simulators, applying afterwards the NV selection cut, following the same procedure used for supernova-induced positron and neutron simulations. The primary interaction vertex position was also selected in the same way as in the SN simulations.

A relevant difference in the NV detected output is that the NV Hitlet Simulator groups hits depending on their arrival time at the PMT (within a ~200 ns processing window). As a result, more detected events are obtained than were originally generated, since some particles within the same GEANT4 event produce hits recorded more than 200 ns after the previous ones. However, as these events are associated with their corresponding GEANT4 event ID, both the selection and the final efficiency calculation remain correct.

The event area results of the NV and MV Hitlet Simulators, after applying the NV selection cut and vertex position selection, are shown in Figs. 55 and 56, respectively, only for events generated inside the detector considered (internal events).

Moreover, note that some non-relativistic charged particles are detectable. For instance, while sub-Cherenkov muons and charged pions are themselves invisible, their decays or nuclear captures almost always produce detectable signals. Also, neutral pions quickly decay to gamma rays which produce detectable electrons through Compton scattering and pair production.

A relevant example supporting the former statement is the bump visible in the muon spectra of both detectors. Figs. 39 and 40 show the positron spectra peak at approximately at 400 PE in the NV and 20 PE in the MV, which could correspond to the 20 MeV maximum of the positron spectra. Accordingly, the bump observed at about 1000 PE in the NV detected signal and at ~50 PE in the MV is compatible with a characteristic signal in the 40-50 MeV range, corresponding to the Michel spectrum from muon decay (Eq. 13) to one $e^{\pm}$, with a maximum energy of 53 MeV, and two neutrinos.

MV generated events also contribute to the signal detected in the NV, as illustrated in Fig. 57-left. This is mainly due to events generated close to the openings present in the NV roof, allowing in some cases the light generated outside the NV to penetrate into it and be detected by the NV PMTs. A similar effect occurs in the reverse direction (right), although with a significantly smaller contribution as a consequence of the smaller NV volume and MV detection efficiency.

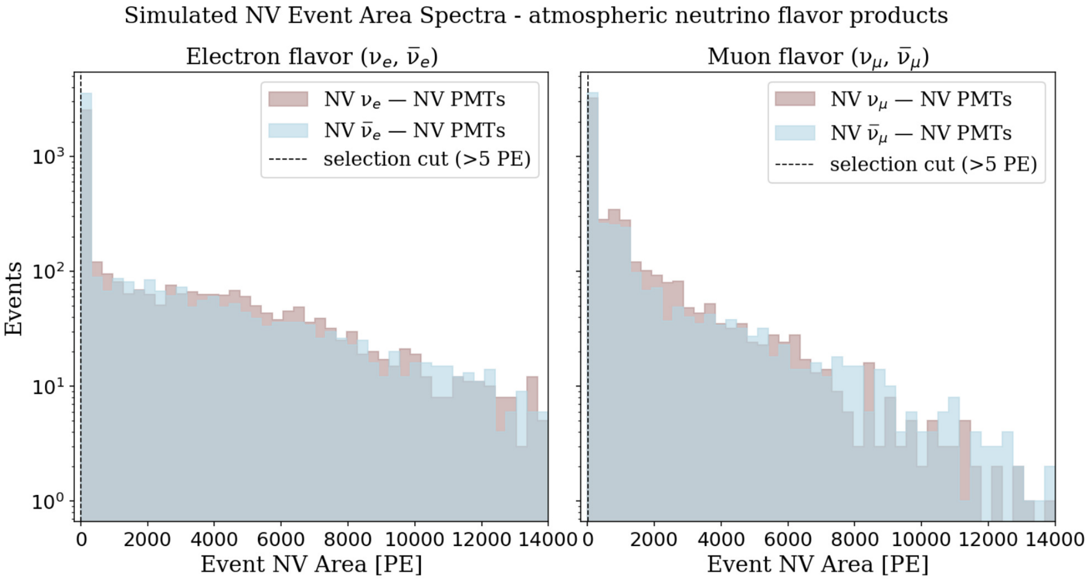

Figure 55: Simulated event area [PE] for all neutrino-induced products detected by the Neutron Veto. The left panel shows electron flavor neutrino products, while the right panel displays the muon flavor ones. Final-state interactions are color-coded, showing only the events generated in the NV. The dashed black line in both panels indicates the NV selection cut.

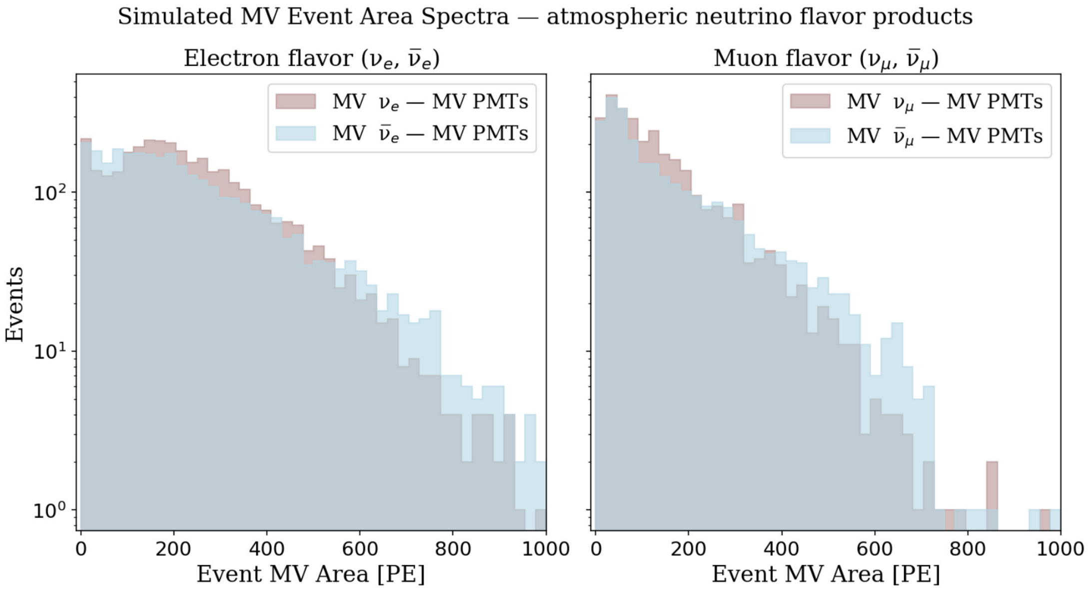

Figure 56: Simulated event area [PE] for all neutrino-induced products detected by the Muon Veto. The left panel shows electron flavor neutrino products, while the right panel displays the muon flavor ones. Final-state interactions are color-coded, showing only events generated in the MV.

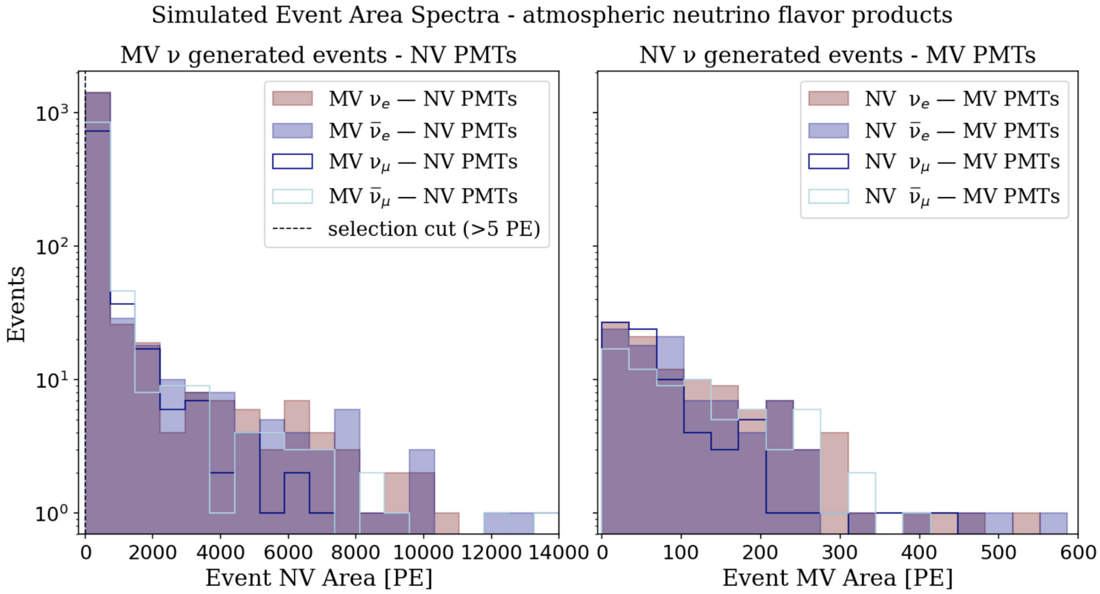

Figure 57: Simulated event area [PE] for all neutrino-induced products detected by the NV (left) and MV (right). Final-state interactions are color-coded, showing only events generated outside the detector under consideration. Muon neutrino histograms are left unfilled for visualization purposes.

4.2.2 Simulated atmospheric neutrino detection efficiency

Considering the initial $5{\cdot}10^3$ GEANT4 simulated events in the full WT and the MV HitSim output, the MV atmospheric neutrino-induced particle detection efficiency has been estimated as the ratio of the latter to the former. This estimation has been performed after selecting only the MV generated events. Similarly, for the $5{\cdot}10^3$ GEANT4 simulated events in the reduced volume surrounding the NV and after the selection of its generated events, we have obtained the GEANT4 events that posses at least one associated NV HitSim event. Consequently, the ratio between the events processed by the HitSim over the NV generated GEANT4 events was computed.

Note that less than 1% of GEANT4 output events producing light in water were not neutrino-induced particles. This is produced by a function contained in the XENONnT model in GEANT4 that separates events of radioisotopes activated through the interaction of primary particles with water and detector materials. These isotopes have half-lives long enough to produce a signal separated from the primary particle signal. An example is ^{15}O, which has a half-life of about 2 minutes. Nevertheless, this only changes the efficiency by $\lesssim$0.1%.

The Neutron Veto and Muon Veto detection efficiencies of electron and muon neutrino- and antineutrino-induced products are shown in Table 9. Note that the detection efficiencies of the two detectors are summarized in decreasing order for the four neutrino flavors. This effect may be due to the lower antineutrino cross section compared to that of neutrinos, as well as to the lower muon Cherenkov light yield relative to electrons and positrons in the same total energy range (0.01-1 GeV), among other factors (steeper fall-off of the event area spectrum at higher amount of collected PEs in Figs. 55 and 56).

The Neutron Veto detects about 55% of the events generated in the Muon Veto. Of these, roughly 1.3% are observed exclusively by the NV. Although these "external" events are not produced inside the NV, their number is non negligible, corresponding to about 15-20% of the internally NV generated events.

In contrast, the Muon Veto detects about 30% of the events generated in the NV, but less than 1% are seen exclusively by the MV. This contribution in therefore negligible since the NV water volume is about 20 times smaller than the MV.

Flavor	ε_{NV} (%)	ε_{MV} (%)
ν_e	87.0 ± 0.7	69.0 ± 0.7
$\bar{\nu}_e$	83.7 ± 0.7	65.4 ± 0.7
ν_μ	83.7 ± 0.7	62.6 ± 0.7
$\bar{\nu}_\mu$	79.8 ± 0.8	57.2 ± 0.7

Table 9: Simulated atmospheric–neutrino detection efficiency in the Neutron Veto and the Muon Veto, only for events generated inside the detector considered.

The relative contributions of CC and NC interactions to the total cross section for all neutrino flavors are typically of about 60% CC and 40% NC. Taking into account that only ~30% from 40% NC component can be detected through γ-rays or neutrons, we conclude that at least ~10% of atmospheric neutrino final states are intrinsically undetectable.

As an example, for ν_μ-induced interactions detected in the NV, where the neutron detection efficiency is ~80%, an additional 3–5% of events may be missed. This is fully compatible with the efficiency of the third row of Table 9.

Table 10 summarizes the expected number of atmospheric neutrino interactions in the Neutron and Muon Vetoes (Table 8), considering the LNGS FLUKA angle- and solar-averaged flux without taking into account oscillations, and cross section splines from GENIE LFG-NAV model. Then, their convolution with the efficiencies, displayed in Table 9, yields the expected number of detected events with uncertainties of the order of 30%. The last column shows the additional contribution from Neutron Veto detecting events generated outside it and not observed by the Muon Veto, the so-called NV external events.

Flavor	Exp. NV	Det. NV (int)	Exp. MV	Det. MV (int)	Det. NV (ext)
ν_e	1.2	1.1	24.3	16.8	0.3
$\bar{\nu}_e$	0.4	0.3	7.9	5.2	0.1
ν_μ	2.1	1.7	40.8	25.6	0.7
$\bar{\nu}_\mu$	0.8	0.6	15.3	8.7	0.2
Total [yr^{-1}]	4.5	3.7	88.3	56.3	1.3

Table 10: Expected (Exp.) and detected (Det.) atmospheric–neutrino interactions per year in the Neutron Veto and the Muon Veto. Detected (internal) interactions refer to the application of the detection efficiency (Table 9), obtained from MC simulations, to its computed expected value in the NV or MV (Table 8). External interactions detected by the NV refers to MV-generated interactions which remain undetected by the MV itself.

4.2.3 XLZD projection for atmospheric neutrino detection

Based on the expectations for atmospheric neutrino detection obtained in this work for the XENONnT vetoes, we make projections based on the larger volume of the XLZD vetoes. For reference, the proposed configuration for the XLZD vetoes introduced in Section 3.3.3 will be considered. In this configuration the Neutron Veto and the Muon Veto contain 337 and 955 tonnes of water, respectively.

In this study and as in the SN case, we assume that the XLZD vetoes will achieve atmospheric neutrino-induced particle detection efficiencies comparable to those of XENONnT (see Section 4.2.2) by maintaining a similar PMT coverage, reflectivity, and water absorption length. By applying Eq. 43, and convolving their expected number of interactions with their corresponding detection efficiencies derived from simulations, the estimates displayed in Table 11 are obtained. Note that NV external events are not considered for simplicity. A total annual atmospheric rate of 118 events is obtained as the sum of the Neutron and Muon Veto contributions (black square in Fig. 58), for the benchmark configuration.

Fig. 58 shows the dependence of the XLZD NV (blue) and MV (red) detected annual rate as a function of the water volume. The blue vertical dotted lines indicate the NV configurations at which it would detect 10 and 100 events per year, corresponding to NV cylinder of 5.8 m and 11 m in diameter (and height), respectively, keeping the assumed 65 m^3 cryostat volume fixed. In contrast, the red vertical dotted lines show the MV configurations at which it would detect 100 and 1000 events per year, corresponding to MV cylinder with diameter (and height) of 12.6 m and 25 m.

For reference, the Neutron Veto volume of the two mentioned configurations would be approximately 90 and 900 tonnes of pure water while the ones from the Muon Veto would be of about 1.2 and 12 kilotonnes of pure water. For comparison, the first NV configuration would be four times smaller than the proposed one, whereas the latter would be approximately three times larger, as shown in the blue line and square of Fig. 58. Similarly for the MV results, the former configuration would be similar to the proposed one, whereas the latter would have a volume of about ten times larger, as shown in the red line and square of Fig. 58.

The total XLZD water tank volumes needed to detect 100 and 1000 atmospheric neutrino events per year are 1100 and 11700 t of pure water approximately, as show in the black line of Fig. 58. This curve has been obtained by assuming the benchmark NV configuration with a volume of 337 tonnes of pure water (cylinder of 12 m height and diameter), added to the full MV volume range considered in Fig. 58 (red line), which spans from 400 to 12000 tonnes.

Flavor	Exp. XLZD NV	Det. XLZD NV	Exp. XLZD MV	Det. XLZD MV
ν_e	12.3	10.7	34.8	24.1
$\bar{\nu}_e$	4.0	3.3	11.3	7.4
ν_μ	20.6	17.3	58.5	36.6
$\bar{\nu}_\mu$	7.7	6.2	21.9	12.5
Total [yr^{-1}]	44.6	37.5	126.5	80.6

Table 11: Expected (Exp.) and detected (Det.) atmospheric–neutrino interactions per year in a proposed XLZD Neutron (337 water tonnes) and the Muon (955 water tonnes) Veto configuration. Detected interactions refer to the application of the detection efficiency (Table 9), assumed to be equal to those of XENONnT, to its computed expected value in the NV or MV.

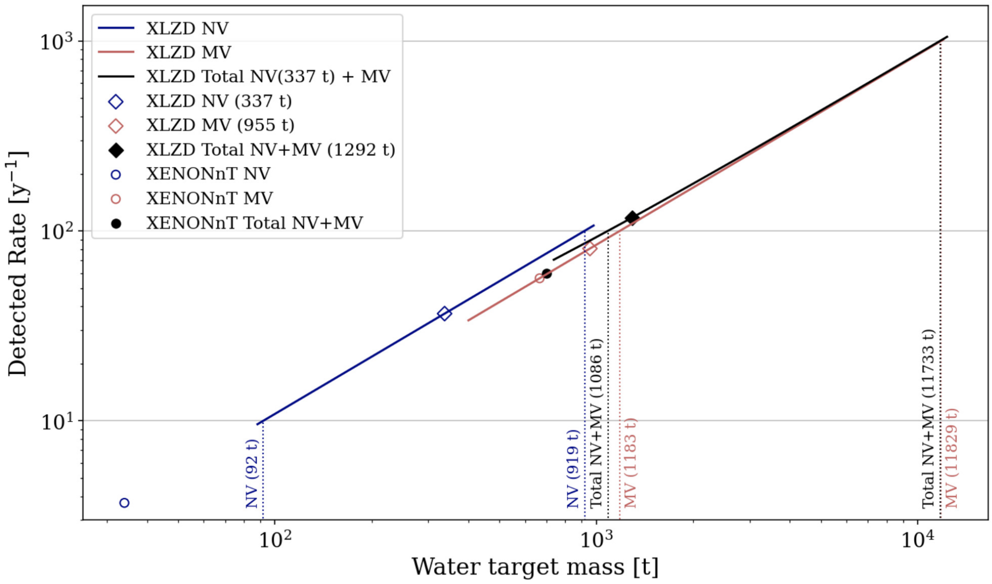

Figure 58: XLZD projection: atmospheric neutrino detected annual rate as a function of the water volume for the Neutron Veto (blue) and the Muon Veto (red). The black solid line represents the whole XLZD MV+NV configuration rate behavior considering the benchmark NV contribution (337 t) and the full MV volume range (red line). The XLZD proposed configuration for NV, MV and NV+MV and the simulation results from XENONnT (Table 10) are shown as colored squares and circles, respectively. Vertical dotted lines indicate the corresponding veto water mass for 10, 100 and 1000 detected events per year.

Conclusions

The XENONnT search for a rare WIMP Dark Matter signal in the nuclear recoil spectrum is primarily affected by neutron backgrounds and coherent neutrino-nucleus scattering. While neutrinos can represent one of the most significant backgrounds, particularly for the next generation of dark matter detectors, they remain an important signal on their own. The study presented in this work investigated the XENONnT veto system's ability to detect some of these neutrino sources, namely supernova and atmospheric neutrinos, by first reporting their fluxes and cross sections in pure water. The working principle and components of the XENONnT experiment were described to provide the experimental foundation for this work. After introducing the unified Monte Carlo simulation framework for its subsystems and the Neutron and Muon Veto Hitlet Simulators, their application to supernova and atmospheric neutrino interactions in the vetoes was described. All analyses were performed considering the demineralized water phase of the XENONnT Vetoes, developed during SR0 and SR1.

The results of these simulations showed that, in the scenario where a galactic core collapse supernova produced by a 27$M_\odot$ progenitor star with a LS220 equation of state occurs at 10 kpc from the Earth, the Neutron Veto would detect 8 events while the Muon Veto would register 108 out of the 170 total events generated over approximately 10 s through inverse beta decay (IBD) in the whole water tank. These estimates were obtained by focusing on the IBD positron signal, followed by the modeling of its detection efficiency curve in terms of the initial positron total energy. This study concluded that the NV would feature a positron detection threshold of about 0.5 MeV, while the MV would exhibit a ~5 MeV detection threshold. Convolving this curve with other supernova neutrino signals showed that the expected number of detected interactions varies significantly with the mass of the star, decreasing by roughly a factor of two for an 11.2 $M_\odot$ star.

This study has also helped to establish the relevant region of interest and characteristic features of these signals in the vetoes. These results imply that the IBD signals of the XENONnT Vetoes, used in coincidence with the Time Projection Chamber CEνNS signal, could enhance the supernova neutrino detection capabilities of XENONnT.

Moreover, the projections performed for the vetoes of the next–generation direct Dark Matter detector, XLZD, yielded an expected number of at least 100 detected IBD positrons up to a supernova distance of about 15 kpc in the 27 $M_\odot$, LS220 EoS supernova model. This result was obtained by assuming a benchmark XLZD veto configuration with NV and MV volumes of 337 and 955 tonnes of pure water, corresponding to two cylinders of 8 and 12 m in height and diameter, respectively.

A promising approach for further development would be to use an initial positron spectrum obtained directly from simulations rather than from an analytical approximation. Studying the sensitivity of the Vetoes to this signal in the presence of backgrounds is another possibility for further extensions of this work. In addition, deepening the study of coincidence between the prompt IBD positron and the ~200 μs delayed neutron signals, particularly considering the Gd-loaded water phase of the Vetoes, could provide a possibility of further background discrimination, increasing detection sensitivity.

The simulation study of atmospheric neutrino interactions in the vetoes, considering a flux given by the FLUKA for the INFN Laboratori Nazionali del Gran Sasso, yielded an expected annual rate of 4 events detected in the Neutron Veto and 56 in the Muon Veto, out of the 93 total events expected in the water tank. These numbers highlight the need for very large detector volumes to achieve significant statistics for the atmospheric neutrino source, even in extremely low-background environments.

Although the expected number of atmospheric neutrino events is relatively low, this study allows us to characterize their detectable signatures and define the range of photoelectron event area that contributes to the veto response, complementing the supernova neutrino analysis.

The detectability of atmospheric neutrinos in the vetoes of Dark Matter detectors will be of crucial importance for the next generation of detectors, where the "neutrino fog" will be approached. For reference, assuming the XLZD benchmark configuration mentioned above, a total annual atmospheric rate of 118 events was obtained in this work as the sum of the Neutron and Muon Veto contributions.

Furthermore, if phenomena such as the solar modulation of the atmospheric neutrino flux are taken into account, the resulting signal time variation could provide an additional method for identifying these events. In addition, employing atmospheric neutrino flux predictions that include vacuum and matter oscillations should be investigated to refine the expected interaction rates for each flavor.

References

[1] F. Reines, “Neutrino interactions,” *Annual Review of Nuclear Science*, vol. 10, no. 1, 1960.

[2] S. Braibant, G. Giacomelli, and M. Spurio, *Particles and fundamental interactions: an introduction to particle physics*. Springer Science & Business Media, 2011.

[3] C. Giunti and C. W. Kim, *Fundamentals of neutrino physics and astrophysics*. Oxford university press, 2007.

[4] M. Spurio, *Probes of Multimessenger Astrophysics. Charged cosmic rays, neutrinos, γ-rays and gravitational waves* (Astronomy and Astrophysics Library). Springer, 2018, ISBN: 978-3-319-96853-7, 978-3-319-96854-4. DOI: `10.1007/978-3-319-96854-4`.

[5] V. Paolone, “DONUT,” in *Aspen Winter Conference on Particle Physics at the Millennium*, Jan. 2001.

[6] M. Takita, “The Super-Kamiokande,” in *International Symposium on Neutrino Astrophysics*, 1992, pp. 135–145.

[7] M. C. Chen, “The SNO+ Experiment,” in *34th International Conference on High Energy Physics*, Oct. 2008. arXiv: `0810.3694 [hep-ex]`.

[8] A. Gando et al., “Reactor On-Off Antineutrino Measurement with KamLAND,” *Phys. Rev. D*, vol. 88, no. 3, p. 033 001, 2013. DOI: `10.1103/PhysRevD.88.033001`. arXiv: `1303.4667 [hep-ex]`.

[9] M. G. Aartsen et al., “Measurement of Atmospheric Neutrino Oscillations at 6–56 GeV with IceCube DeepCore,” *Phys. Rev. Lett.*, vol. 120, no. 7, p. 071 801, 2018. DOI: `10.1103/PhysRevLett.120.071801`. arXiv: `1707.07081 [hep-ex]`.

[10] D. Adey et al., “Measurement of the Electron Antineutrino Oscillation with 1958 Days of Operation at Daya Bay,” *Phys. Rev. Lett.*, vol. 121, no. 24, p. 241 805, 2018. DOI: `10.1103/PhysRevLett.121.241805`. arXiv: `1809.02261 [hep-ex]`.

[11] M. He, “Jiangmen Underground Neutrino Observatory,” *Nucl. Part. Phys. Proc.*, vol. 265-266, pp. 111–113, 2015. DOI: `10.1016/j.nuclphysbps.2015.06.027`. arXiv: `1412.4195 [physics.ins-det]`.

[12] Y. Fukuda et al., “Evidence for oscillation of atmospheric neutrinos,” *Phys. Rev. Lett.*, vol. 81, pp. 1562–1567, 1998. DOI: `10.1103/PhysRevLett.81.1562`. arXiv: `hep-ex/9807003`.

[13] P. A. Machado, “Neutrino Properties and Interactions,” in *The Encyclopedia of Cosmology: Set 2: Frontiers in Cosmology Volume 2 Neutrino Physics and Astrophysics*, World Scientific, 2024, pp. 9–53.

[14] J. A. Formaggio and G. P. Zeller, “From eV to EeV: Neutrino cross sections across energy scales,” *Reviews of Modern Physics*, vol. 84, no. 3, pp. 1307–1341, 2012.

[15] W. J. Marciano and Z. Parsa, “Neutrino electron scattering theory,” *J. Phys. G*, vol. 29, pp. 2629–2645, 2003. DOI: `10.1088/0954-3899/29/11/013`. arXiv: `hep-ph/0403168`.

[16] J. Kim, “Searching for Multi-nucleon Processes in Neutrino Interactions by Proton Identication in the Fine-Grained Detectors for T2K,” Ph.D. dissertation, British Columbia U., 2018. DOI: `10.14288/1.0371248`.

[17] F. Pompa, “Neutrino physics with the XENONnT experiment,” Master’s thesis, Università di Bologna, 2019. [Online]. Available: `https://amslaurea.unibo.it/id/eprint/19448/`.

[18] K. Abe et al., “Diffuse supernova neutrino background search at Super-Kamiokande,” *Physical Review D*, vol. 104, no. 12, p. 122 002, 2021.

[19] A. L. Baxter et al., “SNEWPY: A data pipeline from supernova simulations to neutrino signals,” *The Astrophysical Journal*, vol. 925, no. 2, p. 107, 2022.

[20] A. Mirizzi et al., “Supernova neutrinos: Production, oscillations and detection,” *La Rivista del Nuovo Cimento*, vol. 39, no. 1, pp. 1–112, 2016.

[21] T. Sukhbold, T. Ertl, S. Woosley, J. M. Brown, and H.-T. Janka, “Core-collapse supernovae from 9 to 120 solar masses based on neutrino-powered explosions,” *The Astrophysical Journal*, vol. 821, no. 1, p. 38, 2016.

[22] K. Scholberg, “Supernova neutrino detection,” *Annual Review of Nuclear and Particle Science*, vol. 62, no. 1, pp. 81–103, 2012.

[23] G. Battistoni, A. Ferrari, T. Montaruli, and P. Sala, “The atmospheric neutrino flux below 100 MeV: The FLUKA results,” *Astroparticle Physics*, vol. 23, no. 5, pp. 526–534, 2005.

[24] N. Aghanim et al., “Planck 2018 results-VI. Cosmological parameters,” *Astronomy & Astrophysics*, vol. 641, A6, 2020.

[25] P. Zyla et al., “Review of Particle Physics,” *PTEP*, vol. 2020, no. 8, p. 083C01, 2020, and 2021 update. DOI: `10.1093/ptep/ptaa104`.

[26] B. Penning, “The pursuit of dark matter at colliders—an overview,” *Journal of Physics G: Nuclear and Particle Physics*, vol. 45, no. 6, p. 063 001, 2018.

[27] H. Andernach and F. Zwicky, “English and Spanish Translation of Zwicky’s (1933) The Redshift of Extragalactic Nebulae,” *arXiv preprint arXiv:1711.01693*, 2017.

[28] G. Bertone and D. Hooper, “History of dark matter,” *Reviews of Modern Physics*, vol. 90, no. 4, p. 045 002, 2018.

[29] A. Afruni, G. Pezzulli, and F. Fraternali, “Inflow of low-metallicity cool gas in the halo of the Andromeda galaxy,” *Monthly Notices of the Royal Astronomical Society*, vol. 509, no. 4, pp. 4849–4864, 2022.

[30] J. De Swart, G. Bertone, and J. van Dongen, “How dark matter came to matter,” *Nature Astronomy*, vol. 1, no. 3, p. 0059, 2017.

[31] B.-L. Young, “A survey of dark matter and related topics in cosmology,” *Frontiers of Physics*, vol. 12, no. 2, p. 121 201, 2017.

[32] N. W. M. Team, *NASA Webb ‘Pierces’ Bullet Cluster, Refines Its Mass*, 2025. [Online]. Available: `https://science.nasa.gov/missions/webb/nasa-webb-pierces-bullet-cluster-refines-its-mass/`.

[33] A. Einstein, “Lens-like action of a star by the deviation of light in the gravitational field,” *Science*, vol. 84, no. 2188, pp. 506–507, 1936.

[34] D. Clowe, A. Gonzalez, and M. Markevitch, “Weak-lensing mass reconstruction of the interacting cluster 1e 0657–558: Direct evidence for the existence of dark matter,” *The Astrophysical Journal*, vol. 604, no. 2, p. 596, 2004.

[35] ESA Collaboration, *Planck’s view of the Cosmic Microwave Background*, 2018. [Online]. Available: `https://sci.esa.int/s/wQdrX4A`.

[36] K. Olive et al., “Review of particle physics,” *Chinese physics C*, vol. 38, no. 9, pp. 1–1676, 2014.

[37] G. Bertone, D. Hooper, and J. Silk, “Particle dark matter: Evidence, candidates and constraints,” *Physics reports*, vol. 405, no. 5-6, pp. 279–390, 2005.

[38] G. Lucente, N. Nath, F. Capozzi, M. Giannotti, and A. Mirizzi, “Probing high-energy solar axion flux with a large scintillation neutrino detector,” *Physical Review D*, vol. 106, no. 12, p. 123 007, 2022.

[39] N. Yoshida, A. Sokasian, L. Hernquist, and V. Springel, “Early structure formation and reionization in a warm dark matter cosmology,” *Astrophys. J. Lett.*, vol. 591, pp. L1–L4, 2003. DOI: `10.1086/376963`. arXiv: `astro-ph/0303622`.

[40] S. Chatrchyan et al., “The CMS Experiment at the CERN LHC,” *JINST*, vol. 3, S08004, 2008. DOI: `10.1088/1748-0221/3/08/S08004`.

[41] *ATLAS technical coordination* (Technical design report. ATLAS). Geneva: CERN, 1999. [Online]. Available: `https://cds.cern.ch/record/385482`.

[42] J. Conrad, L. Latronico, F. Longo, and B. Lott, “Fermi Gamma-ray Space Telescope sees first light,” *CERN Cour.*, vol. 48N9, pp. 13–15, 2008.

[43] D. Ferenc et al., “The MAGIC gamma-ray observatory,” *Nuclear Instruments and Methods in Physics Research Section A: Accelerators, Spectrometers, Detectors and Associated Equipment*, vol. 553, no. 1-2, pp. 274–281, 2005.

[44] M. Casolino et al., “Cosmic-ray observations of the heliosphere with the PAMELA experiment,” *Adv. Space Res.*, vol. 37, no. 10, R. Battiston, M. A. Shea, C. Rakowski, and S. Chatterjee, Eds., pp. 1848–1852, 2006. DOI: `10.1016/j.asr.2005.06.035`.

[45] B. Alpat, “Alpha magnetic spectrometer (AMS-02) experiment on the international space station (ISS),” *Nucl. Sci. Tech.*, vol. 14, no. 13, pp. 182–194, 2003. arXiv: `astro-ph/0308487`.

[46] M. Aguilar et al., “Towards Understanding the Origin of Cosmic-Ray Positrons,” *Phys. Rev. Lett.*, vol. 122, no. 4, p. 041 102, 2019. DOI: `10.1103/PhysRevLett.122.041102`.

[47] A. Goldschmidt, “The IceCube detector,” in *27th International Cosmic Ray Conference*, Aug. 2001.

[48] J. Aalbers et al., “DARWIN: towards the ultimate dark matter detector,” *JCAP*, vol. 11, p. 017, 2016. DOI: `10.1088/1475-7516/2016/11/017`. arXiv: `1606.07001 [astro-ph.IM]`.

[49] R. Bernabei et al., “The DAMA project: Achievements, implications and perspectives,” *Progress in Particle and Nuclear Physics*, vol. 114, p. 103 810, 2020.

[50] P. Di Gangi, “The Xenon Road to Direct Detection of Dark Matter at LNGS: The XENON Project,” *Universe*, vol. 7, no. 8, p. 313, 2021.

[51] D. Akerib et al., “Snowmass2021 cosmic frontier dark matter direct detection to the neutrino fog,” *arXiv preprint arXiv:2203.08084*, 2022.

[52] L. Bergström, “Dark matter evidence, particle physics candidates and detection methods,” *Annalen der Physik*, vol. 524, no. 9-10, pp. 479–496, 2012.

[53] E. Aprile et al., “Design and Performance of the XENON10 Dark Matter Experiment,” *Astropart. Phys.*, vol. 34, pp. 679–698, 2011. DOI: `10.1016/j.astropartphys.2011.01.006`. arXiv: `1001.2834 [astro-ph.IM]`.

[54] J. Angle et al., “First Results from the XENON10 Dark Matter Experiment at the Gran Sasso National Laboratory,” *Phys. Rev. Lett.*, vol. 100, p. 021 303, 2008. DOI: `10.1103/PhysRevLett.100.021303`. arXiv: `0706.0039 [astro-ph]`.

[55] E. Aprile et al., “The XENON100 Dark Matter Experiment,” *Astropart. Phys.*, vol. 35, pp. 573–590, 2012. DOI: `10.1016/j.astropartphys.2012.01.003`. arXiv: `1107.2155 [astro-ph.IM]`.

[56] E. Aprile et al., “Dark Matter Results from 225 Live Days of XENON100 Data,” *Phys. Rev. Lett.*, vol. 109, p. 181 301, 2012. DOI: `10.1103/PhysRevLett.109.181301`. arXiv: `1207.5988 [astro-ph.CO]`.

[57] E. Aprile, “The XENON1T Dark Matter Search Experiment,” *Springer Proc. Phys.*, vol. 148, D. Cline, Ed., pp. 93–96, 2013. DOI: `10.1007/978-94-007-7241-0_14`. arXiv: `1206.6288 [astro-ph.IM]`.

[58] E. Aprile et al., “Dark Matter Search Results from a One Ton-Year Exposure of XENON1T,” *Phys. Rev. Lett.*, vol. 121, no. 11, p. 111 302, 2018. DOI: `10.1103/PhysRevLett.121.111302`. arXiv: `1805.12562 [astro-ph.CO]`.

[59] E. Aprile et al., “Constraining the spin-dependent WIMP-nucleon cross sections with XENON1T,” *Phys. Rev. Lett.*, vol. 122, no. 14, p. 141 301, 2019. DOI: `10.1103/PhysRevLett.122.141301`. arXiv: `1902.03234 [astro-ph.CO]`.

[60] E. Aprile et al., “The XENONnT dark matter experiment,” *The European Physical Journal C*, vol. 84, no. 8, p. 784, 2024.

[61] E. Aprile et al., “WIMP Dark Matter Search using a 3.1 tonne × year Exposure of the XENONnT Experiment,” *arXiv preprint arXiv:2502.18005*, 2025.

[62] E. Aprile et al., “Searching for Heavy Dark Matter near the Planck Mass with XENON1T,” *Phys. Rev. Lett.*, vol. 130, no. 26, p. 261 002, 2023. DOI: `10.1103/PhysRevLett.130.261002`. arXiv: `2304.10931 [hep-ex]`.

[63] E. Aprile et al., “Search for Coherent Elastic Scattering of Solar ^{8}B Neutrinos in the XENON1T Dark Matter Experiment,” *Phys. Rev. Lett.*, vol. 126, p. 091 301, 9 2021. DOI: `10.1103/PhysRevLett.126.091301`. [Online]. Available: `https://link.aps.org/doi/10.1103/PhysRevLett.126.091301`.

[64] E. Aprile et al., “First indication of solar B 8 neutrinos via coherent elastic neutrino-nucleus scattering with XENONnT,” *Physical Review Letters*, vol. 133, no. 19, p. 191 002, 2024.

[65] J. Billard et al., “Direct detection of dark matter—APPEC committee report,” *Reports on Progress in Physics*, vol. 85, no. 5, p. 056 201, 2022.

[66] E. Aprile et al., “First Dark Matter Search with Nuclear Recoils from the XENONnT Experiment,” *Phys. Rev. Lett.*, vol. 131, no. 4, p. 041 003, 2023. DOI: `10.1103/PhysRevLett.131.041003`. arXiv: `2303.14729 [hep-ex]`.

[67] E. Aprile et al., “The neutron veto of the XENONnT experiment: Results with demineralized water,” *arXiv preprint arXiv:2412.05264*, 2024.

[68] V. Mazza, “The XENONnT Neutron Veto: Performance in the Gd-doped phase,” Master’s thesis, Università di Bologna, 2024. [Online]. Available: `https://amslaurea.unibo.it/id/eprint/33265/`.

[69] J. Aalbers et al., “The XLZD Design Book: towards the next-generation liquid xenon observatory for dark matter and neutrino physics,” *Eur. Phys. J. C*, vol. 85, no. 10, p. 1192, 2025. DOI: `10.1140/epjc/s10052-025-14810-w`. arXiv: `2410.17137 [hep-ex]`.

[70] X.-J. Xu, Z. Wang, and S. Chen, “Solar neutrino physics,” *Progress in Particle and Nuclear Physics*, vol. 131, p. 104 043, 2023.

[71] R. L. Workman et al., “Review of Particle Physics,” *PTEP*, vol. 2022, p. 083C01, 2022. DOI: `10.1093/ptep/ptac097`.

[72] R. F. Lang, C. McCabe, S. Reichard, M. Selvi, and I. Tamborra, “Supernova neutrino physics with xenon dark matter detectors: A timely perspective,” *Physical Review D*, vol. 94, no. 10, p. 103 009, 2016.

[73] J. Migenda, S. Cartwright, L. Kneale, M. Malek, Y.-J. Schnellbach, and O. Stone, “Sntools: An event generator for supernova burst neutrinos,” *Journal of Open Source Software*, vol. 6, no. 60, p. 2877, 2021.

[74] A. Strumia and F. Vissani, “Precise quasielastic neutrino/nucleon cross-section,” *Phys. Lett. B*, vol. 564, pp. 42–54, 2003. DOI: `10.1016/S0370-2693(03)00616-6`. arXiv: `astro-ph/0302055`.

[75] H. Shi, Z. Huang, J. Zhou, G. Lü, and X. Chen, “A Core-Collapse Supernova Neutrino Parameterization with Enhanced Physical Interpretability,” Nov. 2025. arXiv: `2511.16631 [astro-ph.HE]`.

[76] C. Andreopoulos et al., “The GENIE Neutrino Monte Carlo Generator,” *Nucl. Instrum. Meth. A*, vol. 614, pp. 87–104, 2010. DOI: `10.1016/j.nima.2009.12.009`. arXiv: `0905.2517 [hep-ph]`.

[77] GENIE collaboration, *GENIE cross-sections v3.06.00*, 2025. [Online]. Available: `https://scisoft.fnal.gov/scisoft/packages/genie_xsec/v3_06_00/`.

[78] S. Agostinelli et al., “Geant4—a simulation toolkit,” *Nuclear instruments and methods in physics research section A: Accelerators, Spectrometers, Detectors and Associated Equipment*, vol. 506, no. 3, pp. 250–303, 2003.

[79] A. Mancuso, “The XENONnT neutron veto: design, construction and performance,” Ph.D. dissertation, Università di Bologna, 2024. [Online]. Available: `https://amsdottorato.unibo.it/id/eprint/11437/`.

[80] V. Beligotti, “Study of muon-induced neutrons in XENONnT,” Master’s thesis, Università di Bologna, 2025.

[81] Y. Zhuang, L. E. Strigari, and R. F. Lang, “Time variation of the atmospheric neutrino flux at dark matter detectors,” *Physical Review D*, vol. 105, no. 4, p. 043 001, 2022.

[82] B. Zhou and J. F. Beacom, “First detailed calculation of atmospheric neutrino foregrounds to the diffuse supernova neutrino background in Super-Kamiokande,” *Physical Review D*, vol. 109, no. 10, p. 103 003, 2024.

[83] J. Tena-Vidal et al., “Neutrino-nucleon cross-section model tuning in GENIE v3,” *Phys. Rev. D*, vol. 104, no. 7, p. 072 009, 2021. DOI: `10.1103/PhysRevD.104.072009`. arXiv: `2104.09179 [hep-ph]`.

[84] C. Andreopoulos et al., “The GENIE Neutrino Monte Carlo Generator: Physics and User Manual,” Oct. 2015. arXiv: `1510.05494 [hep-ph]`.

[85] C. H. Llewellyn Smith, “Neutrino Reactions at Accelerator Energies,” *Phys. Rept.*, vol. 3, pp. 261–379, 1972. DOI: `10.1016/0370-1573(72)90010-5`.

[86] J. Nieves, J. E. Amaro, and M. Valverde, “Inclusive quasi-elastic neutrino reactions,” *Phys. Rev. C*, vol. 70, p. 055 503, 2004, [Erratum: Phys.Rev.C 72, 019902 (2005)]. DOI: `10.1103/PhysRevC.70.055503`. arXiv: `nucl-th/0408005`.